Experimental and Numerical Investigation of Therapeutic Ultrasound Angioplasty

Graham P. Gavin (BEng)

PhD **2005**

Experimental and Numerical Investigation of Therapeutic Ultrasound Angioplasty

by

Graham P. Gavin (*BEng*)

Thesis presented to Dublin City University in fulfilment of the requirements for the degree of Doctor of Philosophy

Supervisors: **Dr. Garrett B. McGuinness**
Prof. M.S.J. Hashmi

School of Mechanical and Manufacturing Engineering,
Dublin City University,
Ireland

2005

Declaration

I hereby certify that this material, which I now submit for assessment on the programme of study leading to the award of PhD is entirely my own work and has not been taken from the work of others save and to the extent that such work has been cited and acknowledged within the text of my work.

Signed: 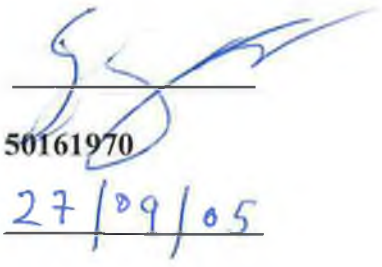

I.D. No: **50161970**

Date: 27/09/05

Abstract

Title: Experimental and Numerical Investigation of Therapeutic Ultrasound Angioplasty

by

Graham P. Gavin (BEng)

Therapeutic ultrasound angioplasty is an emerging minimally invasive cardiovascular surgical procedure that involves the delivery of ultrasonic displacements to the distal-tip of small diameter wire waveguides. The ultrasonic distal-tip displacements affect atherosclerotic plaque and thrombus by direct contact ablation, pressure wave components and cavitation, in addition to an acoustic streaming event around the distal-tip. This study uses experimental and numerical methods to investigate ultrasonic displacements in wire waveguides and the effect the distal-tip displacements have on the surrounding fluid.

An experimental therapeutic ultrasound wire waveguide apparatus is described that delivers displacements to the distal-tip of 1.0 mm and tapered 0.35 mm diameter nickel-titanium (NiTi) waveguides. The operating frequency of the apparatus has been experimentally determined to be 23.5 kHz and for the power settings tested delivers displacements of up to 85 μm peak-to-peak (p-p) to the distal-tip of 1.0 mm diameter waveguides. The apparatus has been shown to directly ablate calcified materials with a stiffer response when compared with atherosclerotic plaques and to generate cavitation and acoustic streaming.

A coupled fluid-structure numerical model of the waveguide and fluid surrounding the distal-tip has been developed that predicts the waveguide displacements and stresses along the entire length of the wire waveguide. The structural results of the model have been validated against experimental measurements of the displacements of the waveguide with the inclusion of a constant damping value of 4.5%. The fluid results of the model predict the pressure amplitudes developed in the surrounding fluid and compare closely with values reported in literature. The model predicts the distal-tip displacements required to cause cavitation, a major disruptive event, and has been compared with experimental observations made with the ultrasonic wire waveguide apparatus.

The waveguide numerical model will prove a valuable design tool in the further development and improvement of this emerging cardiovascular technology.

Table of Contents

Preface:		**Pages I- XIV**
Declaration		I
Abstract		II
Acknowledgements		III
Table of Contents		IV- VI
List of Figures		VII- XII
List of Tables		XIII
Nomenclature		XIV-XV
Publication from this Work		XVI- XVII
Chapter 1:	**Introduction**	**Pages 1- 8**
1.1	Cardiovascular Disease	1
1.2	Minimally Invasive Procedures	3
1.3	Complicated Atherosclerotic Plaques	5
1.4	Therapeutic Ultrasound Angioplasty	6
1.5	Research Objectives and Methodology	7
Chapter 2:	**Literature Survey**	**Pages 9- 40**
2.1	Vascular Disease	9
2.2	Complicated Atherosclerotic Plaques	13
2.2.1	Mechanical Properties of Atherosclerotic Plaques	13
2.2.2	Complications Associated with Present Procedures	15
2.3	Therapeutic Ultrasound Delivered via Wire Waveguide	17
2.3.1	Introduction	17
2.3.2	Ultrasound generation	18
2.3.3	Minimal invasive delivery of ultrasound	19
2.3.4	Mechanical effect of wire waveguide tip displacement	21
2.3.4.1	Direct contact ablation	21
2.3.4.2	Acoustic pressure waves and cavitation	23
2.3.4.3	Acoustic streaming	23
2.3.5	Testing of ultrasound delivered via wire waveguide	24
2.3.5.1	Mechanical performance evaluation	24
2.3.5.2	Clinical evaluation	29
2.4	Theoretical Mechanics Background	32
2.4.1	Steady-state vibration of a uniform rod	32
2.4.2	Acoustic pressure field around and oscillating sphere	34
2.4.3	Cavitation	36
2.4.4	Acoustic streaming	36
2.5	Finite Element Analysis of Ultrasound Transmission in Wire Waveguides	38
2.5.1	Material properties	38

2.5.2 Mesh density 39
2.5.3 Damping 39
2.6 Summary 40

Chapter 3: Design and Development of Ultrasonic Wire Waveguide Apparatus **Pages 41- 72**
3.1 Introduction to Apparatus Design 41
3.2 Ultrasonic Wire Waveguide Apparatus Design and Development 44
3.2.1 Ultrasonic generator and converter 44
3.2.2 Acoustic horn 46
3.2.3 Wire waveguide design 46
3.2.3.1 NiTi wire waveguide 47
Tensile testing of NiTi wire waveguide 49
Material density of NiTi wire waveguide 50
3.2.4 Connection of wire waveguide to acoustic horn 50
3.2.4.1 Evaluation of connection methods 53
Single side set-screw 56
Double side set-screw 60
Axial set-screw 63
3.2.5 Final apparatus design and housing 65
3.3 Summary 72

Chapter 4: Performance Characteristics of the Ultrasonic Wire Waveguide Apparatus **Pages 73- 97**
4.1 Introduction 73
4.2 Direct Peak-to-Peak Displacement Measurement 75
4.2.1 Displacement measurement technique 75
4.2.2 Calibration of objective lens 77
4.3 Wire Waveguide Distal-Tip (p-p) Displacements 80
4.3.1 Effect of input power dial settings 80
4.3.2 Effect of wire waveguide length 84
4.4 Displacement (p-p) Results along Length of Wire Waveguide 90
4.5 Summary 97

Chapter 5: Numerical Model of Wire Waveguide and Fluid Interaction **Pages 98- 156**
5.1 Introduction 98
5.2 Modal Analysis of Wire Waveguide 100
5.2.1 Modal Analysis Method 100
5.2.2 Effects of Mesh Density on Modal Analysis of Wire Waveguide 102
5.2.3 Sensitivity Analysis of Material Properties 102
5.2.4 Results of Modal Analysis 104

5.2.5 Summary of Modal Analysis 106
5.3 Harmonic Response Analysis of Wire Waveguide 111
5.3.1 Harmonic Response Method 111
5.3.2 Distal-tip response of wire waveguides over a range of frequencies 113
5.3.3 Distal-tip response of wire waveguides over a range lengths 113
5.3.4 Displacement response along length of wire waveguides 114
5.3.5 Wire Waveguides with Spherical Distal-tip Geometry 114
5.3.6 Results from harmonic response analysis 114
5.3.7 Summary of Harmonic Analysis of Wire Waveguide 131
5.4 Coupled Fluid-Structure Model of Wire Waveguide 134
5.4.1 Acoustic Fluid-Structure Method 134
5.4.2 Fluid-structure model of spherical distal-tip 137
5.4.3 Fluid-structure model of wire waveguide with no distal-tip 151
5.5 Summary 156

Chapter 6: Experimental Testing of the Ultrasonic Wire Waveguide Apparatus **Pages 157- 179**
6.1 Introduction 157
6.2 Tapered Wire Waveguide 158
6.3 Model Materials 162
6.4 Testing Ultrasonic Wire Waveguide Apparatus on Model Materials 166
6.5 Ultrasonic Wire Waveguide in Fluid 174
6.5.1 Cavitation 174
6.5.2 Acoustic Streaming 176
6.6 Summary 179

Chapter 7: Conclusions and Future Work **Pages 180- 188**
7.1 Conclusions from this work 180
7.2 Summary of Results 182
7.3 Recommended Future Directions 187

List of References **Pages i- xi**

List of Figures

Chapter 1:	**Introduction**	**Pages 1- 8**
Figure 1.1a	Principal causes of death in Ireland for all ages in 2003	2
Figure 1.1b	Principal causes of death in Ireland in 2004 in the 0-64 age category	2
Figure 1.2a	Image of distal end of Medtronic 'Stormer' Balloon Angioplasty catheter	4
Figure 1.2b	Image of distal end of Medtronic 'S660' over-the-wire Stent	4
Chapter 2:	**Literature Survey**	**Pages 9- 40**
Figure 2.1	Systemic Arterial Tree	10
Figure 2.2	Natural history of atherosclerosis	12
Figure 2.3	Uniaxial radial compression data for various types of plaque	14
Figure 2.4a	Generation of ultrasonic displacements	20
Figure 2.4b	Diagram of stepped acoustic horn	20
Figure 2.5	Schematic of ultrasonic wire waveguide in catheter	22
Figure 2.6	General features of acoustic streaming	25
Figure 2.7	Acoustic pressure amplitudes ahead of vibrating wire Waveguide	28
Figure 2.8	Average thrombi dissolution time *in vitro*	30
Figure 2.9	Pressure volume curves after ultrasound energy application	31
Figure 2.10	Diagram of a uniform rod	33
Figure 2.11	Diagram relating to the pressure field developed around an oscillating sphere	35
Figure 2.12	Cavitation threshold intensities for degassed water	37
Chapter 3:	**Design and Development of Ultrasonic Wire Waveguide Apparatus**	**Pages 41- 72**
Figure 3.1	Block diagram of project plan	43
Figure 3.2	Image of Branson ultrasonic generator	45
Figure 3.3	Image of piezoelectric converter	48
Figure 3.4	Image of Acoustic Horn	48
Figure 3.5	Assembled horn and converter	48
Figure 3.6	Stress-strain curve for 0.35 mm NiTi wire	51
Figure 3.7	Cyclic Stress-strain curve for 0.6 mm NiTi wire	52
Figure 3.8	Test-rig for the evaluation of connection methods	54
Figure 3.9	Evaluation of wire waveguide connection methods	55
Figure 3.10	Drawing of single side set screw connection method	57

Figure 3.11	Image of single side set screw connection method	57
Figure 3.12	Data of time-to-failure for single side set-screw connection method	58
Figure 3.13	Image of failed 0.6 mm wire waveguide	59
Figure 3.14	Drawing of double side set screw connection method	61
Figure 3.15	Image of double side set screw connection method	61
Figure 3.16	Data of time-to-failure for double side set-screw connection method	62
Figure 3.17	Drawing of axial crimped set screw connection method	64
Figure 3.18	Image of axial crimped set screw connection method	64
Figure 3.19	Data of time-to-failure for axial crimped set-screw connection method	67
Figure 3.20	Image of failed 0.6 mm axial crimped set-screw connection method	68
Figure 3.21	Image of 0.35 mm diameter wire waveguide with steel sleeve	68
Figure 3.22	Drawing of ultrasonic wire waveguide apparatus	69
Figure 3.23	Image of final ultrasound wire waveguide apparatus	70
Figure 3.24	Data of time-to-failure for axial crimped set-screw connection method in housing	71

Chapter 4:	**Performance Characteristics of the Ultrasonic Wire Waveguide Apparatus**	**Pages 73- 97**
Figure 4.1	Diagram of wire waveguide displacement measurement test-rig	76
Figure 4.2	Schematic of peak-to-peak displacement measurement	76
Figure 4.3	Image of wire waveguide displacement measurement test-rig	78
Figure 4.4	Image of scale bar with superimposed measurements	79
Figure 4.5	Histogram of measurements recorded	79
Figure 4.6	Image of ultrasonic wire waveguide apparatus over microscope lens	81
Figure 4.7	Image of vibrating wire waveguide distal-tip	82
Figure 4.8	Distal-tip displacements (p-p) for a 1.0 mm waveguide	83
Figure 4.9	Distal-tip displacements for multiple wire lengths	85
Figure 4.10	Distal-tip displacements (p-p) for a 1.0 mm waveguide with fitted trend lines	87
Figure 4.11	Distal-tip displacements (p-p) for multiple waveguide lengths and powers with fitted trend lines	89
Figure 4.12	Analytical solution of internal displacements (p-p) in an undamped thin rod of length 288mm	92
Figure 4.13	Image of internal wire waveguide displacement (p-p)	93
Figure 4.14	Experimental results of wire waveguide displacement (p-p) along a wire waveguide of length 288mm	94
Figure 4.15a	Experimental results of wire waveguide displacement	

(p-p) along a wire waveguides of length 273 mm 95
Figure 4.15b Experimental results of wire waveguide displacement (p-p) along a wire waveguides of length 303 mm 96

Chapter 5: Numerical Model of Wire Waveguide and Fluid Interaction **Pages 98- 156**

Figure 5.1 Problem sketch of wire waveguide with fixed-free boundary conditions 101
Figure 5.2a Proximal end of finite element model of 1.0mm diameter wire waveguide with a mesh density of 2 × 606 103
Figure 5.2b Proximal end of finite element model of 1.0mm diameter wire waveguide with a mesh density of 2 × 303 103
Figure 5.3a Mesh density results from modal analysis of 1.0 mm wire waveguide model 107
Figure 5.3b Mesh density results from modal analysis of 0.6 mm wire waveguide model 108
Figure 5.3c Mesh density results from modal analysis of 0.35 mm wire waveguide model 109
Figure 5.4a Effect on the first and fifth resonant frequencies due to variations (± 5%) in Young's modulus 110
Figure 5.4b Effect on the first and fifth resonant frequencies due to variations (± 5%) in density 110
Figure 5.5: Problem sketch for harmonic response analysis of wire waveguide 116
Figure 5.6 Predicted harmonic response of wire waveguide distal-tip peak-to-peak displacements over a frequency range of 0 – 30 kHz 117
Figure 5.7 Predicted harmonic response of wire waveguide distal-tip peak-to-peak displacements over a frequency range of 15 – 30 kHz for input displacement (p-p) of 30 μm, 60 μm and 90 μm 118
Figure 5.8 Predicted harmonic response of wire waveguide distal-tip peak-to-peak displacements over a frequency range of 18 – 28 kHz for an input displacement (p-p) of 30 μm, of length 303 mm and a range of damping values between 1% and 5% 119
Figure 5.9 Predicted harmonic response of wire waveguide distal-tip peak-to-peak displacements over a frequency range of 18 – 28 kHz for an inputted displacement (p-p) of 30 μm, over a range of lengths of 263 mm, 283 mm and 303 mm 120

Figure 5.10 Predicted response of wire waveguide distal-tip peak-to-peak displacements at 23.5 kHz, over a range of lengths from 118 mm – 303 mm, for an inputted displacement (p-p) of

32 μm and a range of damping values of 4%, 4.5% and 5%. 122
Figure 5.11 Comparison of wire waveguide distal-tip peak-to-peak displacements, over a range of lengths from 118 mm – 303 mm, for an inputted displacement (p-p) of 32 μm (power setting = 1.5) and a damping value of 4.5% 123
Figure 5.12 Comparison of wire waveguide distal-tip peak-to-peak displacements, over a range of lengths from 118 mm – 303 mm, for an inputted displacement (p-p) of 46 μm (power setting = 2.25) and a damping value of 4.5% 124
Figure 5.13 Comparison of numerical (no damping) and analytical wire waveguide (l=288 mm) internal displacements and numerically determined internal stress 126
Figure 5.14 Comparison of numerical (damping = 4.5%) and experimental wire waveguide (l=288 mm) internal displacements and numerically determined internal stress 127
Figure 5.15 Comparison of numerical (damping = 4.5%) and experimental wire waveguide (l=303 mm) internal displacements and numerically determined internal stress 128
Figure 5.16 Comparison of numerical (damping = 4.5%) and experimental wire waveguide (l=273 mm) internal displacements and numerically determined internal stress 129
Figure 5.17 Comparison of predicted frequency response of wire waveguide distal-tip peak-to-peak displacements for a 0.35 mm wire waveguide with and without spherical distal ball-tips. 133
Figure 5.18 Schematic of Numerical Fluid-Structure Modelling 136
Figure 5.19 Distal Section of Acoustic Fluid Structure Model of Wire Waveguide with 1.0 mm spherical ball-tip 138
Figure 5.20 Predicted pressure field (real pressure) around distal section of acoustic fluid structure model of wire waveguide with 1.0mm spherical ball-tip. Distal -tip displacement is 64.5μm (p-p) at 23.5 kHz. 139
Figure 5.21 Comparison of predicted frequency response of wire waveguide distal-tip peak-to-peak displacements for a 0.35 mm wire waveguide with a 1.0 mm diameter spherical distal ball-tip and with a surrounding fluid 140
Figure 5.22 Comparison of predicted frequency response of wire waveguide distal-tip peak-to-peak displacements for a 0.35 mm wire waveguide with a 1.5 mm diameter spherical distal ball-tip and with a surrounding fluid 141
Figure 5.23 Comparison of predicted pressure field (nodal results) and analytically determined pressures along axial line '0X' for a wire waveguide with a 1.0 mm spherical ball-tip 143
Figure 5.24 Comparison of predicted pressure field (nodal results) along axial line '0X' for a wire waveguide with a 1.0 mm

and 1.5 mm diameter spherical ball-tip for various distal-tip displacements at 23.5 kHz 144
Figure 5.25 Comparison of predicted pressure field (nodal results) along radial line '0R' for a wire waveguide with a 1.0 mm and 1.5 mm diameter spherical ball-tip for various distal-tip displacements at 23.5 kHz 145
Figure 5.26 Predicted surface pressure field (nodal results) for a wire waveguide with a 1.5 mm spherical ball-tip. Distal -tip displacement is 51 μm (p-p) at 23.5 kHz. 147
Figure 5.27 Predicted pressure (real) field (nodal results) around distal section of acoustic fluid structure model of wire waveguide with 2.46 mm spherical ball-tip and distal -tip displacement (p-p) of 130 μm (p-p) at 22.5 kHz as described by Makin et al [62] 148
Figure 5.28 Comparison of predicted pressure amplitude field (nodal results) and experimental results along axial line ahead of distal-tip for a model based on device described by Makin et al [62] 149
Figure 5.29 Comparison of a) the experimental distribution, as described by Makin et al [62] and b) the predicted pressure field distribution (tip displacement = 6.5μm (p-p)), in the region surrounding (>12mm) from the distal tip 150
Figure 5.30 Distal section of acoustic fluid structure model of wire waveguide with no distal-tip geometry 152
Figure 5.31 Predicted pressures (real) in region surrounding 0.35 mm diameter wire waveguide with no distal-tip geometry (freq. = 23.5 kHz, distal-tip displacement (p-p) = 11 μm) 152
Figure 5.32 Comparison of predicted pressure amplitudes (nodal results) along axial line for a wire waveguide (0.35 mm diameter) with no distal-tip geometry for various distal-tip displacements at 23.5 kHz. 153
Figure 5.33 Predicted pressure field distribution (tip displacement = 80 μm (p-p)) in the region surrounding a 0.35 mm wire waveguide with no distal tip 154
Figure 5.34 Comparison of predicted pressure amplitudes (nodal results) along axial line for a wire waveguide (1.0 mm diameter) with no distal-tip geometry for various distal-tip displacements at 23.5 kHz. 155

Chapter 6: Experimental Testing of the Ultrasonic Wire Waveguide Apparatus **Pages 157- 179**
Figure 6.1 Diagram of 0.35 mm tapered wire waveguide 159

Figure 6.2 Distal-tip displacements (p-p) for a 1.0 mm diameter wire waveguide of length 288 mm for multiple input

	power dial-settings	160
Figure 6.3	Image of stationary and vibrating 0.35 mm tapered wire waveguide distal tip with a calibrated objective lens magnification factor of 8	161
Figure 6.4	Billets of calcium carbonate and calcium hydroxide	164
Figure 6.5	Results of compression tests on billets of calcium carbonate (n=2) and compressed calcium hydroxide (20, 40 and 50kN)	165
Figure 6.6	Compression results from calcium carbonate billets with fitted linear trendlines	165
Figure 6.7	Diagram of direct ablation testing rig	167
Figure 6.8	Adapted static friction tester used in bench testing of ultrasonic wire waveguide apparatus in determining material removal rates for various specimens	168
Figure 6.9	Results of direct ablation on the 20, 40 and 50 kN compressed calcium hydroxide samples for a 0.35 mm tapered wire waveguide and an applied force of 1 Newton	169
Figure 6.10	Results of direct ablation on the calcium carbonate for a 0.35 mm tapered wire waveguide and an applied force of 1 Newton.	169
Figure 6.11	Results of direct ablation on the 20, 40 and 50 kN compressed calcium hydroxide samples for a 0.35 mm tapered wire waveguide and an applied force of 2 Newtons.	170
Figure 6.12	Results of direct ablation on the calcium carbonate for a 0.35mm tapered wire waveguide and an applied force of 2 Newtons.	171
Figure 6.13	Image of calcium carbonate specimen with hole drilled through with 0.35 mm diameter tapered wire waveguide, also shown	172
Figure 6.14	Image of 20 kN calcium hydroxide specimen with hole drilled through with 0.35 mm diameter tapered wire waveguide	172
Figure 6.15	Image of 20 kN calcium hydroxide specimen with hole drilled through with 1.0 mm diameter wire waveguide	173
Figure 6.16	Images of the distal-tip of the 1.0 mm diameter wire waveguide in water at ambient temperature for various input power dial-settings between 1.5 and 6.5	175
Figure 6.17	Images of acoustic streaming around the distal-tip of the 1.0 mm diameter wire waveguide for various input power dial-settings	177

List of Tables

Chapter 2:	**Literature Survey**	**Pages 9- 40**
Table 2.1	Acoustic horn tip powers	26
Table 2.2	Waveguide tip displacements	26
Chapter 3:	**Design and Development of Ultrasonic Wire Waveguide Apparatus**	**Pages 41- 72**
Table 3.1	Ultrasonic wire waveguide apparatus design requirements	42
Chapter 4:	**Performance Characteristics of the Ultrasonic Wire Waveguide Apparatus**	**Pages 73- 97**
Table 4.1	Comparison of experimental and analytical non-resonant lengths	85
Table 4.2	Comparison of linear and exponential fit trend lines	89
Chapter 5:	**Numerical Model of Wire Waveguide and Fluid Interaction**	**Pages 98- 156**
Table 5.1	Comparison of Analytical and Numerical Resonant Frequencies	105

Nomenclature

u	*harmonic displacement amplitude at any point in a uniform rod*
x	*the distance of a point in a uniform from the proximal end*
t	*time*
l	*length of a uniform rod*
b	*input displacement amplitude*
ω	*angular frequency*
c	*longitudinal speed of sound in a medium*
f	*frequency (Hz)*
P	*Pressure Amplitude*
P_r	*Real Pressure*
P_i	*Imaginary Pressure*
ρ	*density*
d	*displacement amplitude*
R	*Radius of sphere*
r	*radial location in a field*
θ	*angular location in a field*
T	*Cavitation Threshold*
E	*Young's Modulus*
A_f	*Austenitic Finish Temperature*
σ	*Standard Deviation*
$[K]$	*stiffness matrix*
$\{\varphi_i\}$	*mode shape vector of mode i*

ω_i *natural frequency of mode i*

[M] *mass matrix*

(r ×y) *mesh density*

$(\ddot{\vec{u}})$ *nodal acceleration vector*

$(\dot{\vec{u}})$ *nodal velocity vector*

$(\vec{u})$ *nodal displacement vector*

$(\vec{F}^{a})$ *applied force vector*

[C] *damping matrix*

(β) *variable matrix multiplier*

ζ *constant damping value*

$(\ddot{\vec{P}})$ *2nd derivative of nodal pressure with respect to time*

$(\vec{P})$ *nodal pressure*

$[R]$ *coupling matrix*

F_c *applied feed force*

F_a *applied weight*

F_r *static friction force*

Note: All displacements used are peak-to-peak displacements unless otherwise stated

Publications from this Thesis

Journal Papers:

Performance Characteristics of a Therapeutic Ultrasound Wire Waveguide. Graham P. Gavin, Garrett B. McGuinness, Finbar Dolan and M.S.J. Hashmi. 2005. *International Journal of Mechanical Sciences. (Submitted)*

Conference Papers:

An Acoustic Fluid-Structure Simulation of a Therapeutic Ultrasound Angioplasty Device. Graham P. Gavin, Garrett B. McGuinness, Finbar Dolan and M.S.J. Hashmi. *II International Conference on Computational Bioengineering, Lisbon, Portugal.* 2005.

Conference Presentations:

Development and Performance Characteristics of an Ultrasound Angioplasty Device. Graham P. Gavin, Garrett B. McGuinness, Finbar Dolan and M.S.J. Hashmi *Proceedings of the 11th Ann. Confer. of the section of Bioengineering of the Royal Academy of Medicine in Ireland.* 2005.

Development of a Numerical Model to Simulate Pressure Distributions in Ultrasound Angioplasty. Graham P. Gavin, Garrett B. McGuinness, Finbar Dolan and M.S.J. Hashmi *Proceedings of the 10th Ann. Confer. of the section of Bioengineering of the Royal Academy of Medicine in Ireland.* 2004.

Conference Posters:

Pressure Distribution around Spherical Distal Ball-tip in Ultrasound Angioplasty. Graham P. Gavin, Garrett B. McGuinness, Finbar Dolan and M.S.J. Hashmi *Conference of European Society of Biomechanics, 's-Hertogenbosch, the Netherlands.* 2004.

Industry Conferences:

Ultrasound Waveguide Device for the Treatment of Atherosclerotic Plaque. Graham P. Gavin, Garrett B. McGuinness, Finbar Dolan and M.S.J. Hashmi. *Medtronic International Science and Technology Annual Conference, Minneapolis, USA.* 2005.

Ultrasound Waveguide Device for the Treatment of Atherosclerotic Plaque. Graham P. Gavin, Garrett B. McGuinness, Finbar Dolan and M.S.J. Hashmi. *Medtronic European Science and Technology Conference, Maastricht.* 2005.

In memory of my father, John, who was laid to rest as the final words fell on these pages. We will miss you always.

Chapter 1

Introduction

1.1 Cardiovascular Disease

The World Health Organisation has studied the global prevalence of cardiovascular diseases (CVD) and estimate that as many as 16.7 million deaths worldwide can be attributed to CVD each year [1]. By 2020, cardiovascular disease will be the leading cause of death in developing countries with worldwide deaths totalling 25 million [1].

Cardiovascular diseases include coronary heart disease (CHD), stroke and other diseases of the circulation and have been shown to be the leading cause of death in the European Union (EU), accounting for nearly half of all deaths (42%), with a total of 1.5 million people dying annually [2].

In an attempt to quantify the economic impact the American Heart Association estimated that the cost of cardiovascular diseases to the American economy, in 2004, was approximately $368.4 billion [3]. This figure includes, among others, hospital and procedural costs, nursing costs and the economic costs due to loss of productivity, as the disease tends to affect individuals in the prime of their earning power and their productivity.

In Ireland, in 2003, 39% of deaths were related to cardiovascular disease, as shown in Figure 1.1a [4]. Coronary heart disease accounted for 20% of all deaths. When age statistics are taken into account, primarily the 0 – 64 years category as shown in Figure 1.1b, in 2004 the death rate from CVD in Ireland was 24% of all deaths and was higher (61.83 per 100,000 population) than the EU average (55.63 per 100,000 population) [4].

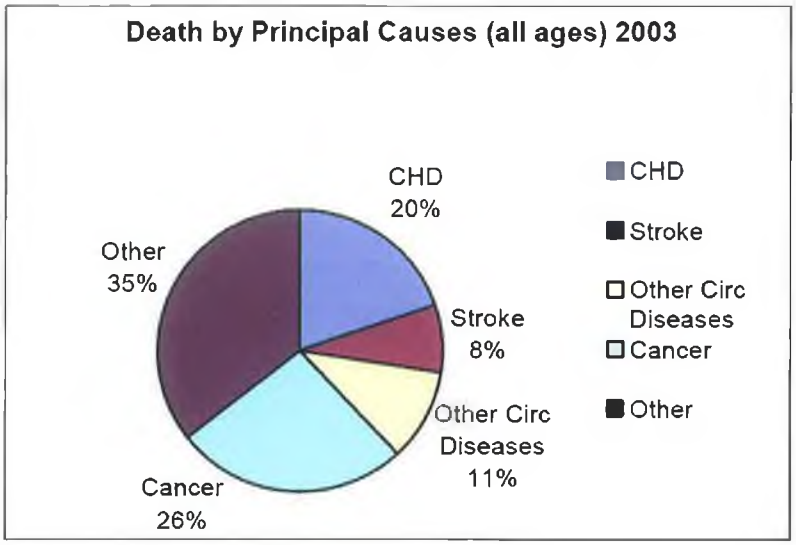

Figure 1.1a: Principal causes of death in Ireland for all ages in 2003, Irish Heart Foundation, Reports and Position Statements [4]

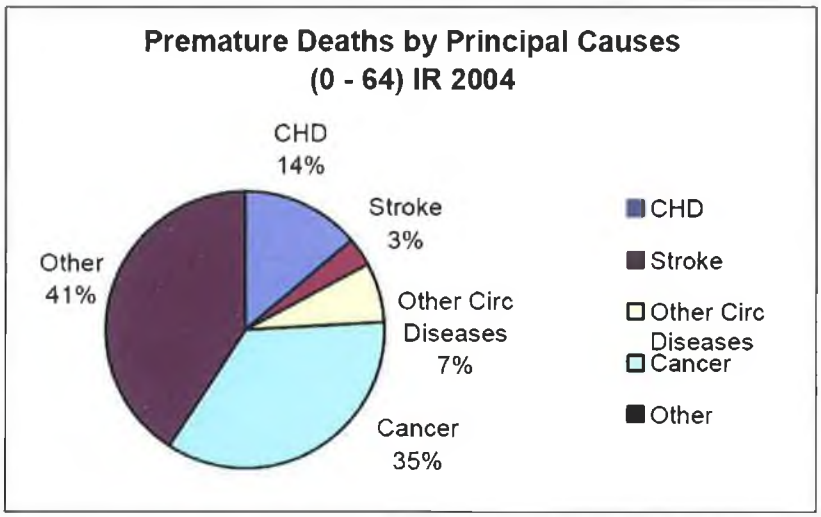

Figure 1.1b: Principal causes of death in Ireland in 2004 in the 0-64 age category, Irish Heart Foundation, Reports and Position Statements [4]

Coronary heart disease is a blockage of the coronary arteries and results in a reduction of blood flow to the heart muscle. These blockages can be the result of a gradual chronic process such as atherosclerosis, an abnormal thickening of the arterial wall resulting in the loss of blood supply downstream, or can occur more rapidly by clotting or by the occurrence of a thromboembolism [5, 6]. Blockages and atherosclerosis can also occur in the peripheral arteries and peripheral thromboembolism is considered the most common cause of sudden arterial occlusion [7].

1.2 Minimally Invasive Procedures

Balloon angioplasty involves the use of a small balloon at the distal end of a catheter, as shown in Figure 1.2a, which enters the narrowed arterial section and expands it by inflating the balloon and forcing both the diseased and healthy section of arterial wall open [8, 9 (cited in 10)]. Once the balloon catheter is removed it is intended that the plaque remains permanently deformed and that blood flow will return to near normal parameters [10, 11]. This is an example of a minimally invasive procedure and is significantly less traumatic for the patient than an arterial by-pass, which involves open surgery.

Since its invention in 1978, balloon angioplasty has become one of the most widely carried out surgical procedures in the United States. In 2001, an estimated 571,000 balloon angioplasty procedures were performed representing an increase of 266% since 1987 [3].

Another common procedure based on balloon dilation is a stent implant; a wire mesh scaffolding that is deployed to the narrowed region over a balloon catheter as shown in Figure 1.2b. When the balloon is deflated and removed the stent implant remains *in situ* to hold the arterial section open [12].

These are mechanical devices that seek to re-open the arterial lumen by loading and permanently deforming the plaque. These procedures suffer from two major complications. Following balloon dilation, which causes stretching of healthy and diseased arterial tissue, remodelling and reformation starts to take place [6, 13].

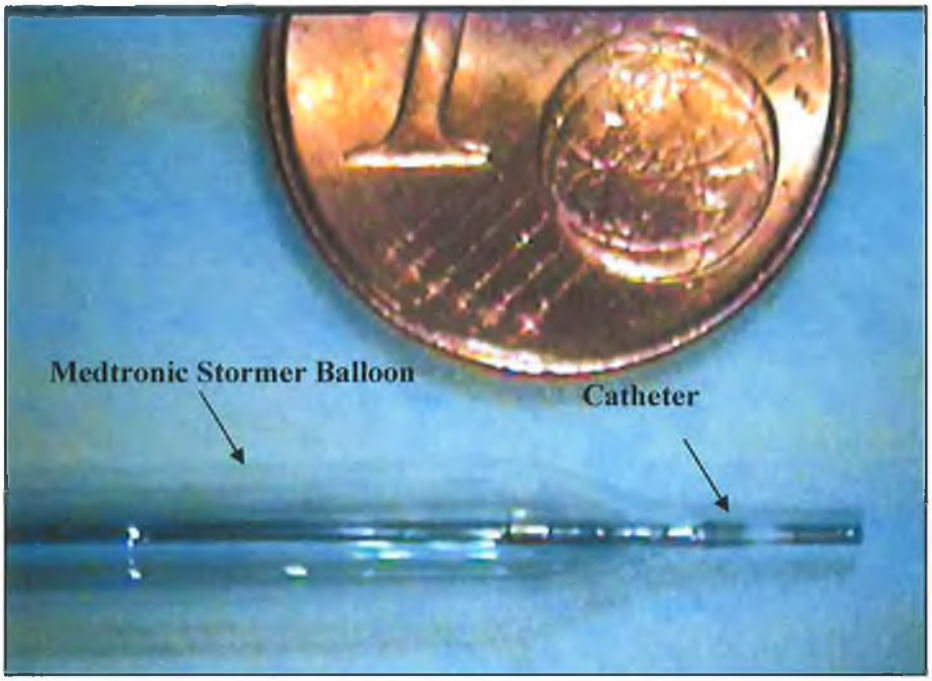

Figure 1.2a: Image of the distal end of a Medtronic 'Stormer©' balloon angioplasty catheter.

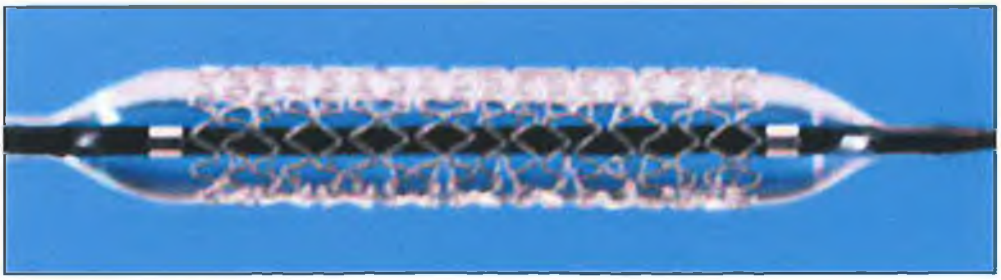

Figure 1.2b: Image of the distal end of a Medtronic "S660©" over-the-wire coronary stent, image courtesy of Medtronic Vascular Ltd ©.

This process is due to a healing response in the region and is known as restenosis. This form of complication is a biological response to intervention and tends to occur in the months following the procedure. According to some investigators restenosis rates for balloon angioplasty procedures alone can be as high as 60% after six months whereas for stented vessels the value is usually between 20-30% for a similar time period [14].

1.3 Complicated Atherosclerotic Plaques

Present angioplasty procedures require that the lesion must be capable of being crossed by a guidewire; a thin wire that acts as a guide-rail for the balloon catheter. If the vessel is nearly or totally occluded, the surgeon cannot gain access to the site with the guidewire resulting in a severe reduction to interventional success [15, 16].

In addition to the complications gaining access to totally occluded arteries the mechanical properties of the diseased tissues are extremely diverse. Work has been carried out to assess the various mechanical properties of lesions and all report a wide variation in mechanical properties with plaque varying from a soft distensible material to a rigid calcified plaque [17, 18].

These calcified plaques tend to be able to resist the mechanical loads from the balloon dilation procedures and higher pressures have to be utilised in order to fracture this rigid material. These complications tend to severely reduce the success rates when treating calcified lesions with standard methods [19].

Topoleski and Salunke showed that calcified plaques show distinct rigid mechanical behaviour from other plaque types and therefore may require specific procedures, devices or protocols to improve success rates and long-term results [20].

Another disadvantage associated with many minimally invasive cardiovascular dilation procedures, including balloon angioplasty and stent implantation, is their inability to cause selective injury to the atherosclerotic plaque

[21]. In the re-opening of an occluded artery or in the removal of plaque material, dilation procedures induce injury on adjacent healthy arterial sections.

It is therefore considered desirable to develop a device or procedure that could mechanically target calcified or totally occluded lesions and selectively damage, ablate or otherwise disrupt this rigid plaque material. Any device that can induce damage to this rigid material may also act as pre-treatment so diseased arteries may be more effectively treated by conventional balloon angioplasty or stent implantation.

1.4 Therapeutic Ultrasound Angioplasty

Ultrasound in medicine is widely used in medical imaging or diagnostic procedures that utilise the differential mechanical properties of biological tissue to build up an echo pattern and subsequently an image of internal tissue layout. This is a low power ultrasound application and generally takes place at high frequencies in the Megahertz range [22].

The use of high-power low-frequency ultrasound external to the body has been used for aortic valve de-calcification and, also, focused ultrasound in lithotripsy for the disintegration of kidney and gallstones [23]. These extracorporeal devices are based on the fact that ultrasound at the correct frequency and amplitude can disrupt inelastic rigid tissue while distensible healthy elastic tissue in the locality will remain largely unaffected.

It was therefore hypothesised that this form of ultrasonic energy in cardiovascular surgery may have the potential to fracture or ablate calcified or fibrous tissue while the more distensible healthy arterial tissue remains unaffected [24 (cited in 23), 25, 26].

Initial work reported in the literature shows that this form of ultrasonic energy delivered via small diameter wire waveguides can disrupt thrombus and atherosclerotic plaque, *in vitro* and *in vivo*, and that rigid calcified plaques are more susceptible to the ultrasonic energy [7, 21, 27, 28].

There appears to be a great deal of commercial interest in this emerging minimally invasive technology. This thesis represents the first stage of an investigation into the engineering science principles of therapeutic ultrasound angioplasty and was performed in collaboration with Medtronic Vascular Ltd. (Galway, Ireland).

In early 2005, Flowcardia™ Inc., (Sunnyvale, California, USA), received approval to market their ultrasonic waveguide Crosser© System in the European Union for the treatment of chronic total occlusions, following failure to cross by conventional guidewire techniques [29]. Clinical trials are currently underway (2005) and application for final approval to the Food and Drug Administration (FDA) is expected in the United States market later this year (2005) [29, 30].

Most work to date in this novel use of therapeutic ultrasound in the treatment of cardiovascular disease has concentrated on the end clinical benefits of the method while little work appears in the literature in the understanding of how this form of ultrasonic energy is delivered down small diameter wire waveguides to the lesion location.

In addition, much work is needed to fully understand what effects the vibrating distal-tip of the waveguide has on surrounding fluid and plaque material. This may be best approached by using bench-top, experimental studies and numerical methods to simulate wire waveguide, distal-tip and surrounding fluid behaviour. To date no numerical model of this nature appears in the literature.

Still, the initial clinical results reported appear promising and, with recent market approvals, therapeutic ultrasound angioplasty is likely to have a future role in the targeting of complicated lesions including chronic total occlusions and calcified and fibrous plaques.

1.5 Research Objectives and Methodology

The objectives of this work are to develop an experimental therapeutic ultrasound apparatus and a numerical coupled fluid-structure model of the

therapeutic ultrasonic displacements delivered via small diameter wire waveguides and the affects these displacements have on the surrounding fluid.

A literature review of the use of this form of therapeutic ultrasound in the treatment of cardiovascular diseases is presented identifying powers and frequencies of operation as well as other published information such as the effect of ultrasound delivery on surrounding tissue and fluid.

This thesis will describe the design and the development of a therapeutic ultrasound wire waveguide apparatus that is then used in further investigative studies. An experimental investigation of the performance characteristics of this experimental ultrasound waveguide apparatus is performed using an optical microscope.

A computational model which simulates the fluid-structure interaction between the wire waveguide and surrounding fluid will be developed and validated against the experimental results reported in this thesis and in the literature.

Finally, the wire waveguide apparatus will be bench tested on some model materials similar to or more resistant than calcified plaque to further understand and identify mechanisms of ablation and disruption.

Chapter 2

Literature Survey

2.1 Vascular Disease

Arterial function can be broken down into two main categories. The primary function is to act as a conduit to deliver blood in an efficient manner from the heart to the various tissues and organs of the body. This requires a complex vascular tree throughout the body delivering oxygenated blood to the various extremities and returning it to the heart as shown in Figure 2.1 [31].

Not only is the supply of blood crucial but also the manner in which it is supplied. Arteries seek to act as cushions to actively control the fluid flow properties of the blood delivered, such as pressure and velocity. The intermittent contraction of the heart results in a pulsating flow that is subsequently altered to regular flow through the organs and tissues by arterial cushioning function [5].

Within an artery, the healthy vessel wall can be generally divided into three distinct layers: the intima, the media and the adventitia. Each of these layers in turn is made up of one or more of the arrangement of components which constitute the vessel wall: the endothelial lining, collagen fibres, elastin fibres, smooth muscle cells and ground substances [33]. Atherosclerosis is the underlying condition that is responsible for most cardiovascular disease and tends to occur in the large and medium-sized arteries including the coronary, iliac and femoral arteries [6, 31].

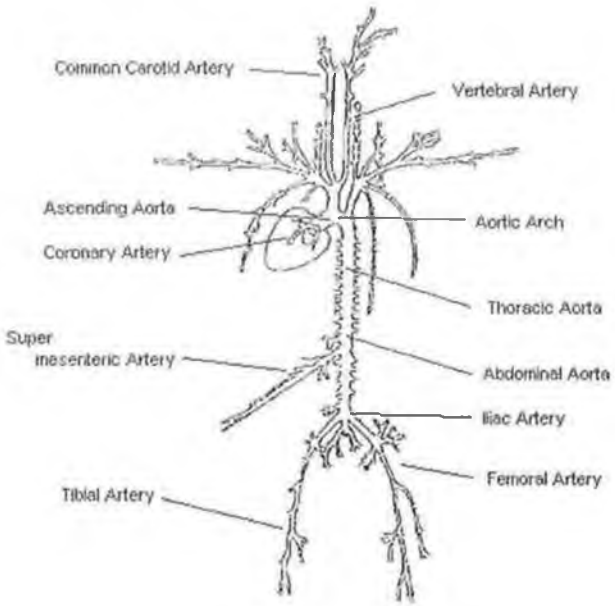

Figure 2.1: Systemic Arterial Tree based on diagram in Mechanical Properties of Arterial Wall, Hayashi [31] (used with the kind permission of the author, originally modified from McDonald [32])

Atherosclerosis is a thickening of the arterial medial layer which affects the artery by altering conduit function and reducing blood flow downstream. There are numerous theories describing the origin and progression of the disease that are beyond the scope of this work but all agree it is a time-dependent process with varying stages of severity [34, 35, 36 (cited in 6)] and this appears to be backed up by extensive autopsy studies [37]. The progression of atherosclerosis can be broadly classified into three stages; the fatty streak, the fibroatheromatous plaque and the complicated lesion [6, 38].

Initially, a fatty streak formed by lipid deposits appears on the intimal surface of arteries but does not always progress into a fibroatheromatous plaque [6, 38]. The fibroatheromatous plaque consists of a necrotic plaque core that is surrounded on one side by the underlying arterial wall and bounded on the other by a plaque cap as shown in Figure 2.2 [6].

The fibroatheromatous plaque is a clearly raised lesion and has a plaque core that consists of a mix of collagen fibres, soft lipid and calcified materials and is often known as a fibrous core [38]. The lesions tend to progress further and are often associated with events such as the plaque core rupturing that can lead to haemorrhaging or clotting resulting in further loss or complete loss of lumen diameter as shown in Figure 2.2 [6].

Of particular interest to this work are complicated calcified plaques that have a plaque core and cap that are primarily composed of calcified minerals and tough collagen fibres [6]. These are known as advanced lesions partly due to the time they take to develop as they tend to occur near the end of the lesion progression. They are closely associated with chronic total occlusions and the success rate with standard procedures involving the mechanical loading of the lesion tend to be lower as the rigidity and stiffness of the calcified material and tough collagen fibres can resist these applied loads [19].

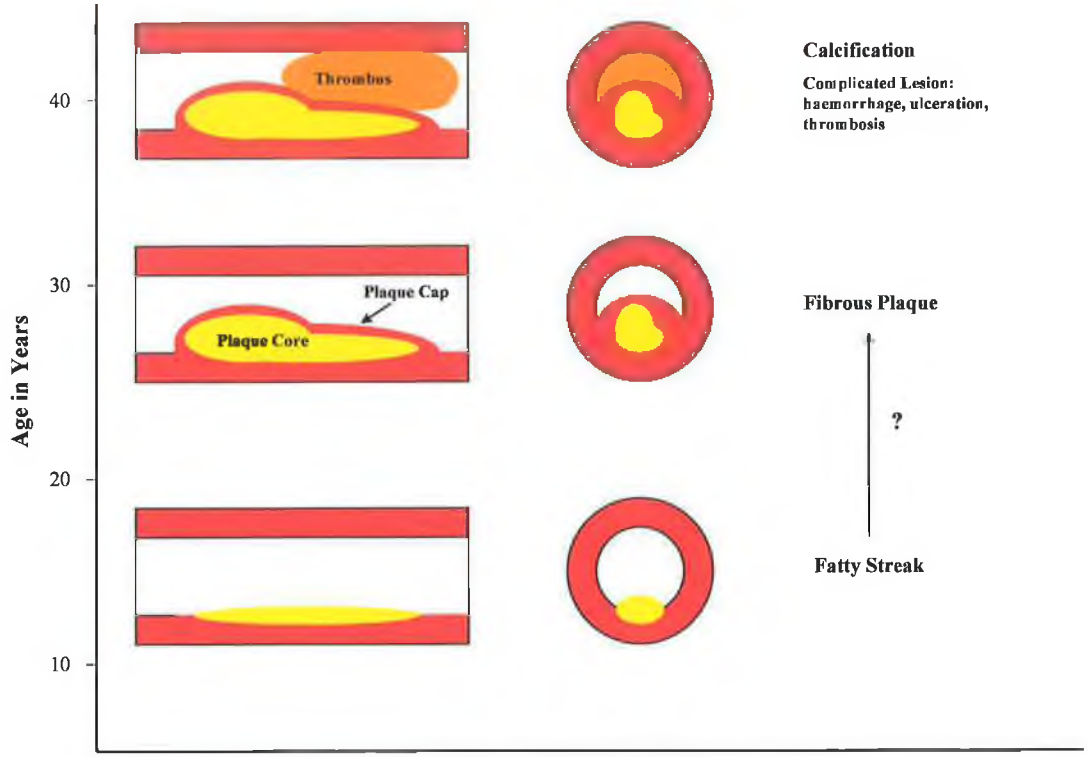

Figure 2.2: Natural history of atherosclerosis, adapted from Topoleski and Salunke [6] (originally modified from Cotran [39])

2.2 Complicated Atherosclerotic Plaques

Knowledge of the mechanical and physical properties of various plaques and the healthy arterial wall is of great benefit when developing methods and devices to treat specific lesion types and also in the sourcing of model materials to bench test devices on, prior to clinical trials. The material properties are largely responsible for problems associated with present interventional procedures. These are biological materials, however, and exhibit complex properties under deformation.

2.2.1 Mechanical Properties of Atherosclerotic Plaques

Specific mechanical properties vary from person to person. Healthy arterial tissue generally exhibits a non-linear elastic response to loading and this appears to be due to the variation in elastin and collagen fibres that are embedded in the arterial wall [40, 41, 42].

The majority of mechanical testing reported in the literature appears to be focused on tensile and compression testing of the various constituents of the arterial wall and of fibroatheromatous plaque. Tests have been conducted on plaque caps, plaque cores and individual layers of the arterial wall such as the media.

Topoleski and Salunke [6, 20] investigated the mechanical behaviour of various plaque types as well as underlying arterial tissue. Segments of human aortoiliac artery were excised during autopsy and atherosclerotic lesions (plaque cap and core) removed and cut to 5 mm × 5 mm sections. A pathologist classified each specimen as calcified (hard), fibrous (medium) or atheromatous core (soft).

The samples were subjected to a uniaxial radial compression tests and the averaged results are shown in Figure 2.3. The authors concluded that the plaque response was indeed non-linear and that all the plaques fell into three distinct mechanical behaviour patterns. The wide variation in the properties of the plaque types can be clearly seen with the hard calcified and fibrous plaques (containing some calcium) showing distinct behaviour with a considerably stiffer response than both the medium and soft plaques and the healthy arterial tissue under compression.

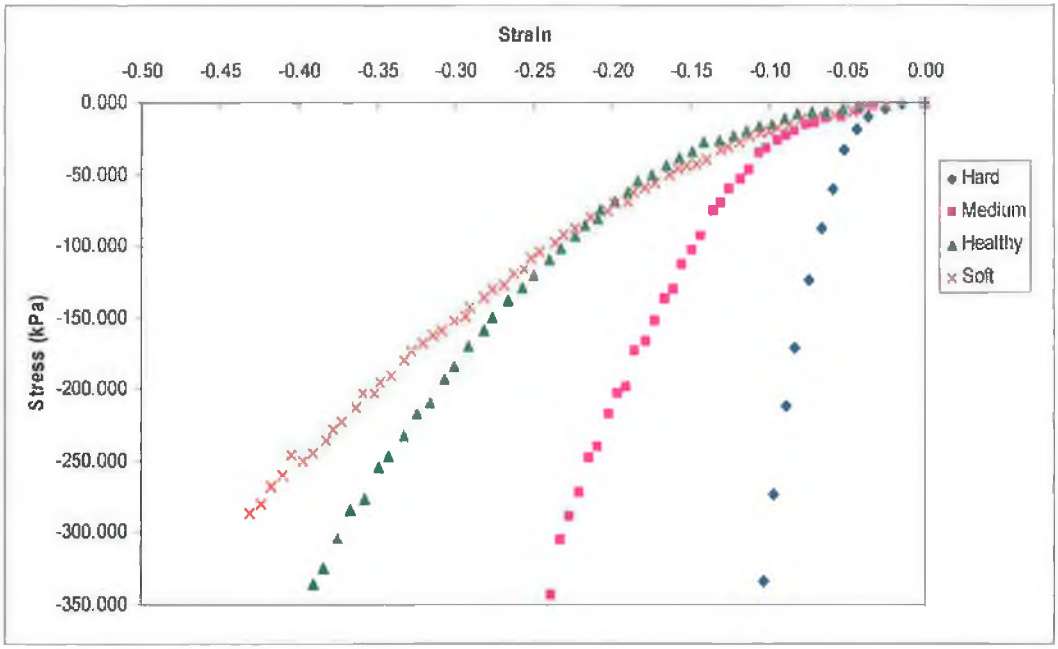

Figure 2.3: Uniaxial radial compression data for various types of plaques. Adapted from Topoleski and Salunke [6] using digitising extraction software (xyextract ©)

Tensile testing of various human atherosclerotic tissues was performed by Loree *et al* [17] with a total of 26 intimal plaques being tested. Specimens were excised in the circumferential direction and classified histologically as cellular (12 samples), hypocellular [t] (9 samples) or calcified (5 samples).

The tensile test results showed great variation within each plaque classification. Plaques classified as hypocellular and calcified were considerably stiffer than cellular plaques. The authors noted that, for a given stress value, the cellular plaque strain was approximately 2-3 times greater than the equivalent value for calcified plaque and hypo-cellular plaque which showed similar tensile properties.

The authors believed that this was primarily due to the fact that in the tensile mode the presence of collagen fibres dominated the tensile circumferential properties and that the other constituents of the plaque such as calcification played a less important role. They stated that in numerous interventional procedures like balloon angioplasty the primary mechanism present was radial compression of the plaque and perhaps the calcification had a greater effect.

This appears to be strongly supported by the experimental work from Topoleski and Salunke [6, 20] and other authors who investigated the properties of lesions [43, 44, 45, 46]. The results of these authors suggest that calcified and fibrous plaques show a similar stiffer response than non-fibrous soft lesions.

In the compressive mode however, the rigidity of the calcifications seem to play a major role as suggested by Loree *et al* [17] and are considerably more rigid than both the fibrous and non-fibrous lesion types.

2.2.2 Complications Associated with Present Procedures

The ability of the guidewire to cross the lesion is the main determinant of interventional success in 80% of cases [15]. If this cannot be achieved dilation devices, such as balloon angioplasty and stents, cannot gain access to the lesion site and reopen the blockage.

t: hypocellular: containing less than the normal number of cells

Chronic total occlusions caused by advanced plaques, haemorrhaging and thrombosis can all result in these total blockages of the arterial lumen and therefore the prevention of standard interventional procedures.

The presence of calcification can occur in both the plaque cap and plaque core and results in the overall rigidity of the lesion increasing. Calcifications require that higher balloon pressure have to be used during dilation procedures and Siegel *et al* concluded that there is a link between high balloon inflation pressures and deep vessel injury and acute procedural complications, known as barotraumas, all resulting in greater localised damage and higher restenosis rates [47].

While plaques can develop around the entire lumen structure resulting in a concentric lesion, progression is often eccentric [11, 48, 49 (cited in 6)]. Calcified eccentric lesions pose further complications as during dilation procedures the rigid calcified side of the artery remains non-dilated while the healthy and often thinner side of the arterial wall over dilates resulting in eccentric lesions yielding sub-optimal results [11].

The inability of standard dilation procedures to specifically target diseased tissue is a major drawback and may be one of the further causes of restenosis. These complications seriously affect procedural success rates and many authors have suggested that these lesions may require specific protocols to improve success [20, 47].

Any such method would ideally be capable of navigating the vascular structure by minimally invasive means and disrupt total blockages, due to plaque or thrombus, and also be able to target calcified material while healthy arterial tissue in the vicinity remained largely unaffected.

Therapeutic ultrasound transmitted via wire waveguides appears to have the potential to disrupt these types of lesions by minimally invasive means.

2.3 Therapeutic Ultrasound Delivered via Wire Waveguide

Therapeutic ultrasound is the use of high-amplitude low-frequency ultrasound [23]. The mechanical effect this form of ultrasound has on biological tissues was first noted by Conte and de Lorenzi (cited in Atar *et al* [50]) and its effectiveness is based on the fact that at the right combination of frequency and amplitude inelastic rigid tissue is vigorously disrupted while elastic tissue can absorb the energy [51, 52].

It was therefore conceived that this form of energy may be useful in the treatment of cardiovascular disease and could potentially have advantages over standard dilation procedures in the targeting of specific lesions, especially complicated rigid calcified and fibrous plaques [23].

2.3.1 Introduction

Development and testing of experimental devices began as early as the 1970s but were extremely limited for practical use. Sobbe *et al* [24 (cited in 23)] showed that ultrasound delivered through a large diameter wire probe resulted in a longitudinally vibrating distal-tip that had the effect of disrupting blood clots in animals.

During the mid-1980s particular design issues were addressed by two groups, headed by Siegel and by Rosenschein with the goal of making an actual working prototype for initial clinical testing and potentially for use in trials. No specific design issues appear in the literature and the majority of work focuses on the end clinical results. Some general information is reported and is included in this review [21, 25, 26].

Both teams based their design efforts on the system developed by Sobbe *et al* delivering the ultrasonic waves to the lesion via a wire waveguide. This sets up longitudinal stress waves and a longitudinal peak-to-peak displacement at the distal-tip of the wire waveguide with the potential to disrupt both lesions and clots.

2.3.2 Ultrasound Generation

In order to displace the distal-tip a wire at the frequencies and high amplitude displacements required to cause disruption to lesions a source capable of delivering these ultrasonic displacements was required. Both Siegel *et al* [25] and Rosenschein *et al* [21 and 26] describe the use of a piezoelectric transducer as a source for the ultrasound.

The piezoelectric effect is a property of certain classes of crystalline materials including natural crystals of Quartz, Rochelle Salt and Tourmaline plus manufactured ceramics such as Barium Titanate and Lead Zirconate Titanates (PZT). When a mechanical pressure is applied to these materials a voltage is produced proportional to the pressure applied. Conversely, when a voltage is applied the structure changes shape; acting as an electromechanical transducer. These shape changes are usually very small, in the order of a few microns, and the voltage amplitudes required to produce them are large, around a 1000 volts [53].

Dynamic voltages can also be applied which result in a dynamic displacement or shape change in the material. In this arrangement the material behaves very much like a mechanical system with resonant frequency characteristics. The transducer's output will be at a maximum at the first resonant frequency, a characteristic of the material and geometric configuration [53]. Using a stack arrangement as shown in Figure 2.4a mechanical displacements of 0 –5 μm peak-to-peak at frequencies less than 100 kHz can be achieved. An ultrasonic generator provides the electrical source to drive the transducer at the resonant frequency of the piezoelectric stack.

These types of transducer are used mostly for sonochemistry applications where agitation of chemical and biological samples is required. The frequencies and amplitudes discussed are chosen for their ability to cause cavitation, a desirable effect in processing chemical solutions [54].

It is largely due to this reason and availability that transducers used for generating the ultrasound in intravascular therapeutic ultrasound have been adapted from sonochemistry applications [25].

For sonochemistry and the generation of cavitation, the displacements (at the frequencies used) from the converter (transducer) are still too small for sample processing. An acoustic horn or waveguide is usually attached to the transducer to amplify the displacements [54].

Acoustic horns are solid metal rods that are designed to couple to the front-end mass of the converter. They achieve an increase in output displacement by two means. Firstly, their geometry is such that the input wave is compressed through a progressively smaller cross-sectional area as it travels the length of the rod resulting in a larger displacement at the output. This can be clearly seen in both linear and exponentially tapered horns [54].

Secondly, horns can be manufactured to resonate at the frequency of the ultrasonic converter. Stepped horns, as shown in Figure 2.4b, appear most useful for adaptation to the natural frequency of the driving transducer [55]. In most practical applications a combination of both stepped and tapered sections are used in horn design. Horns are manufactured from materials that have high dynamic fatigue strength and low acoustic loss, such as titanium alloys [54]. With a horn attached to the converter output displacements greater than 150μm peak-to-peak can be achieved and at frequencies less than 100 kHz.

Acoustic horns, being of solid metal configuration, lack the flexibility necessary to navigate the tortuous vascular geometry. In order to deliver these ultrasonic peak-to-peak displacements over sufficient lengths and with the flexibility necessary in minimally invasive vascular surgery the idea of using wire waveguides was developed [24 (cited in 23), 25, 26].

2.3.3 Minimal Invasive Delivery of Ultrasound

Most of the initial work in the area was based on finding methods to deliver this form of ultrasound over waveguide lengths ($\approx$ 1600 mm) and small diameters ($<$ 0.35 mm) capable of being used in surgical applications. While little detailed description of the exact design and construction methods is given, some general conclusions were drawn from early design and testing.

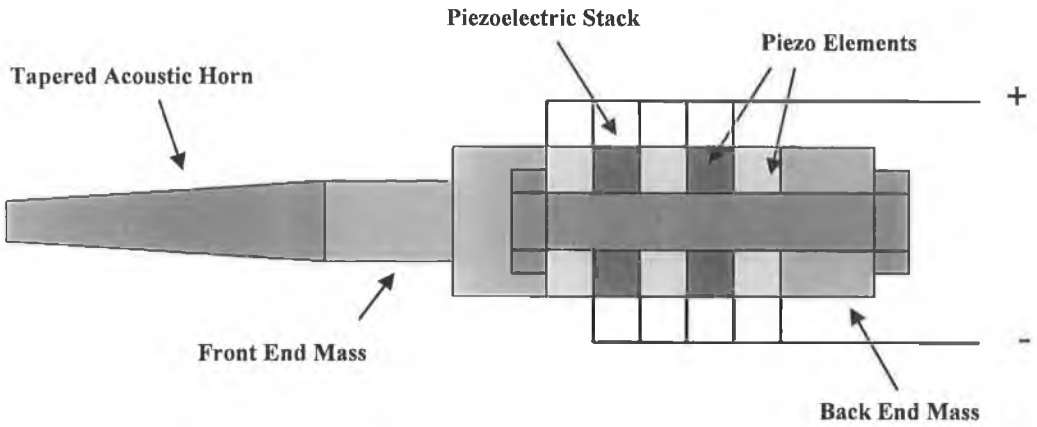

Figure 2.4a: Generation of mechanical ultrasonic displacements: converter and acoustic horn

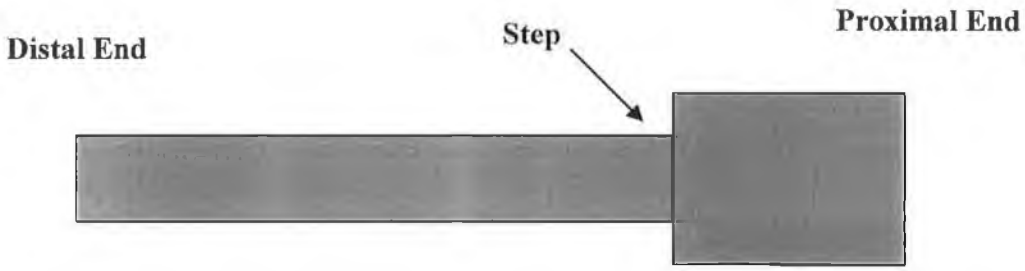

Figure 2.4b: Diagram of a stepped acoustic horn

Rosenschein *et al* [21] described the use of a solid flexible aluminium transmission wire mechanically coupled to the acoustic horn. Details surrounding the coupling method were not included. Fischell *et al* describe the use of a solid 1.5F (≈ 0.5 mm diameter) titanium wire waveguide [56]. This system also appears to have been used by Ariani *et al* [7] and Demer *et al* [51].

These authors work, in general, detail the use of solid wires manufactured from aluminium, titanium or alloys of both to form the transmission member or wire waveguide to transmit the ultrasound from the acoustic horn to the lesion location. This ultrasonic transmission results in longitudinal displacements at the distal tip of the wire waveguide.

In addition both teams located a ball-tip or enlargement at the distal end of the wire. This increases the surface area in contact with the lesion and the surrounding fluid. Demer *et al* [51] describes the use of a 2.0 mm diameter ball-tip and Siegel *et al* [47] a 1.7 mm diameter ball-tip in conjunction with the wire waveguide.

2.3.4 Mechanical Effects of Wire Waveguide Tip Displacement

Atar *et al* [50] suggested that the ultrasonic longitudinal vibration of the wire waveguide distal-tip results in four major potentially disruptive events; direct contact ablation, pressure wave components, cavitation and acoustic micro-streaming and all these appear to be related to the distal-tip displacement amplitude, frequency and geometry [57, 58, 59, 60]. A diagram of the distal section of the wire waveguide and location of disruption mechanisms is shown in Figure 2.5

2.3.4.1 Direct Contact Ablation

The oscillating distal-tip of the wire waveguide acts as an ultrasonic reciprocating micro-drill. Research in ultrasonic micromachining has shown that it is associated with low material removal rates by microchipping, and is ideal for ablating brittle ceramic materials [61].

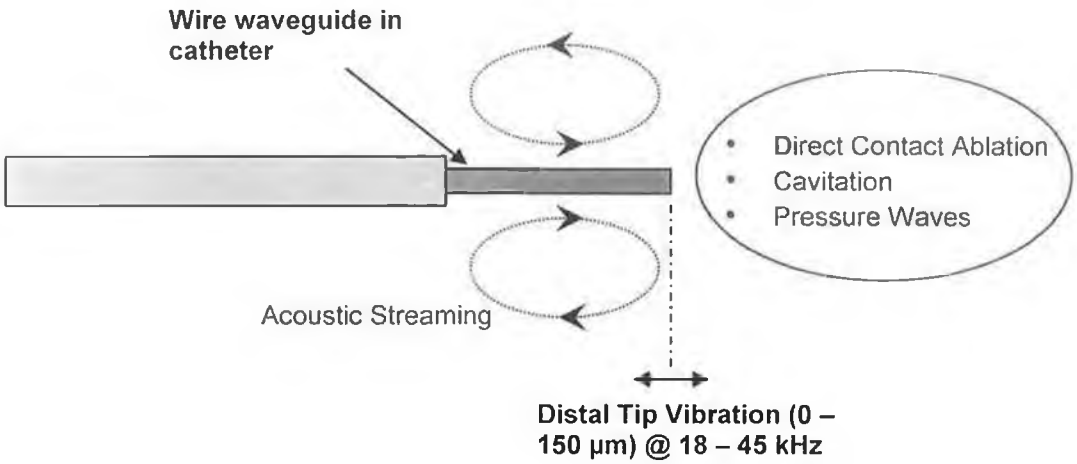

Figure 2.5: Schematic of ultrasonic wire waveguide in catheter and the regions surrounding the longitudinal vibrating distal-tip where disruptive mechanisms can occur.

Direct contact between the oscillating tip and the plaque in the arterial lumen results in the fragmentation and ablation of the plaque into microscopic particles and is considered to be one of the major effects of ultrasound angioplasty [52].

Also, it appears that due to the varying material properties of the plaques this form of fragmentation technique ablates less distensible rigid calcified and fibrous plaques faster than flexible material such as the healthy arterial wall tissue [26].

2.3.4.2 Acoustic Pressure Waves and Cavitation

As a result of the direct contact between the oscillating distal-tip and surrounding fluid an oscillating acoustic pressure field, superimposed on the ambient pressure, is established around the distal-tip [58, 62]. Of particular interest is the fact that if the pressure amplitude is sufficiently high cavitation may occur.

Cavitation occurs when on the negative side of a pressure cycle, such as when the wire waveguide tip is retracting, with sufficient amplitude and frequency, suspended gas bubbles in the fluid, in channels within the tissue or trapped at solid interfaces expand and collapse with the generation of shock waves. Burdic [57] has suggested a simplified relationship between pressure and cavitation threshold, discussed in section 2.4.3. Cavitation is a potentially significant erosion event undesirable in most acoustic applications but necessary in cavitation cleaning baths and sonochemistry [57, 58, 63].

Yock and Fitzgerald [23] concluded that cavitation is a major contributing factor in the disruption of plaque and thrombus and that ultrasound ablation of lesions was only present above the cavitation threshold and that the rate of disintegration correlates with the amount of power delivered above this threshold.

2.3.4.3 Acoustic Streaming

Two general forms of fluid motion are set up around an oscillating sphere in a fluid. The first can be considered as the oscillatory fluid motion very close to the

wall of the tip and, secondly, a unidirectional fluid motion in an external acoustic streaming layer as shown in Figure 2.6 [58, 59].

It is the combined presence of direct contact, acoustic pressure waves, cavitation and acoustic streaming that led investigators to believe that ultrasound delivered via a wire waveguide could disrupt arterial lesions and some analytical theory further describing these disruptive mechanisms is discussed later.

2.3.5 Testing of Ultrasound Delivered via Wire Waveguide

The testing reported in the literature in the use of therapeutic ultrasound delivered via wire waveguides can be broadly categorised into; (i) mechanical testing and performance characteristics and (ii) clinical end results and effects. While both are of interest to this work the mechanical characteristics are focused upon and clinical effects referred to as appropriate.

2.3.5.1 Mechanical Performance Evaluation

Ariani *et al* [7] describe the use of a 20 kHz converter delivering pulsed energy (50% duty cycle) to a 0.76 mm titanium wire waveguide with a 2.0 mm ball-tip and a length of 89 cm. Using this system they describe measuring the wire waveguide peak-to-peak (p-p) distal-tip displacements by means of an optical microscope.

For various acoustic horn distal-tip power inputs between 8 – 25 Watts the wire waveguide distal-tip displacements were measured and displacements between 63.5 μm and 111 μm were documented. Table 2.1 shows the measured wire waveguide distal-tip displacements for the range of powers tested.

This method of optically determining tip displacements is similar to a technique in acoustic horn technology described by Perkins [54]. Many authors describe the output from the waveguide to the surrounding environment in terms of this crucial distal-tip displacement [21, 51]. Table 2.2 shows the documented distal-tip displacements achieved by various investigators.

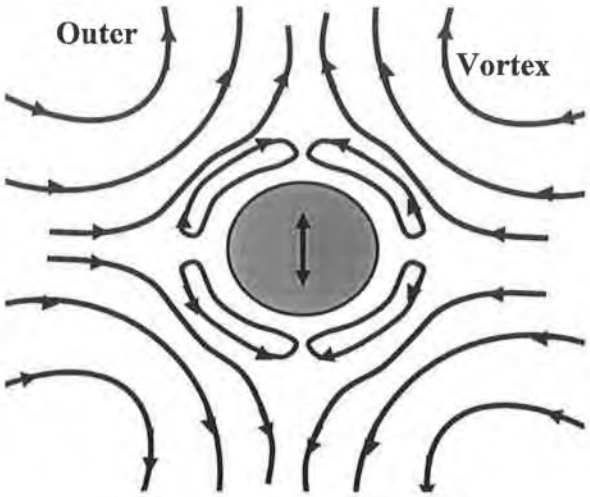

Figure 2.6: General features of acoustic microstreaming near a small vibrating sphere. Adapted from Nyborg [58]

Table 2.1: Acoustic horn tip power versus wire waveguide distal-tip displacement at 20 kHz from Ariani *et al* [7]

Acoustic Horn Tip Power (Watts)	8	11	15	18	23	25
Waveguide Tip Displace. p-p (μm)	63.5	76	83	89	102	111

Table 2.2: Waveguide Tip Displacements from the literature

Author	**Frequency of Operation (kHz)**	**Distal Peak-to-peak Displacement (μm)**	**Wire Data**
Rosenschein et al [21]	*20*	*150 ± 25*	*Aluminium Alloy Wire* *1.6mm* *No Ball Tip*
Ariani et al [7]	*20*	*63.5 - 111*	*Titanium Wire* *.72mm* *2mm Ball-Tip*
Demer et al [51]	*20*	*50 ± 25*	*Titanium Wire* *.5mm* *2mm Ball-Tip*
Makin et al[62]	*22.5*	*200/ 130*	*Titanium Wire* *1.98/2.46 mm Ball-Tip*

Experimental work reported by Makin and Everbach [62] shows the acoustic pressure field developed in the region surrounding the distal-tip of a vibrating wire-waveguide. The device operated at 22.5 kHz and delivered wire waveguide distal-tip displacements of 200 μm or 130 μm to two wire waveguide options. The first waveguide was 445 mm in length with a 1.98 mm diameter ball-tip and the second wire was of 660 mm length with a 2.46 mm diameter tip.

Figure 2.7 shows the pressure amplitude in the axial range ahead of the 2.46 mm diameter tipped wire waveguide with a peak-to-peak displacement of 130 μm. The results show decreasing pressure amplitudes with increasing distance in the range of 12- 250 mm. Measurements could not be made in the region close to the wire waveguide tip but it was inferred by the authors that these would be of the order of a few hundred kilopascals and were therefore sufficient to cause the cavitation that was observed.

Rosenschein *et al* [21] determined that, for the device described, cavitation was observed to occur only above the threshold value of 8 Watts at the distal-tip of the acoustic horn and that above this threshold a conically shaped cavitation field was observed. This information regarding power output is only applicable to this device but demonstrates that below a certain wire waveguide distal-tip displacement the acoustic pressures developed are insufficient to cause cavitation.

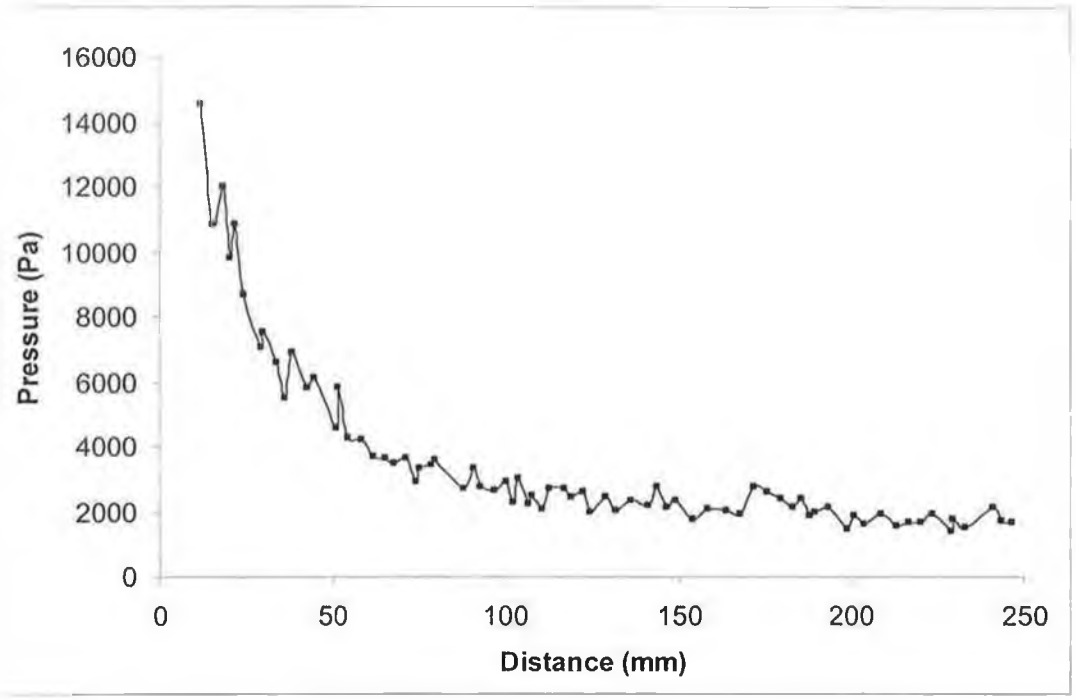

Figure 2.7: Acoustic pressure amplitudes in a range axially ahead of the vibrating wire waveguide with ball-shaped distal-tip. Data digitised from Makin and Everbach [62] (using xyextract© digitising software).

2.3.5.2 Clinical Evaluation

Ariani *et al* used an ultrasound waveguide to disrupt human thrombus *in vitro* and *in vivo* [7]. While no exact mode of disruption is determined their results show an inverse relationship between acoustic horn distal-tip power and time to dissolve the clots; higher powers dissolved the clots in a shorter time period. Figure 2.8 shows this relationship and this can be related back to Table 2.1 for corresponding wire waveguide distal-tip displacements. Other authors have published similar results in the treatment of thrombus both *in vivo* and *in vitro* [21, 64].

In addition to this experimental work conducted on thrombus other authors have tested the effect of the ultrasound delivery on atherosclerotic lesions. Siegel *et al* [52] experimentally tested a 19.5 kHz system on 50 lesions of which 34% were calcified. The results showed that ultrasound delivered via a wire waveguide could recanalise the arteries affected by the lesions and that the calcified arteries treated with therapeutic ultrasound could subsequently be dilated at lower pressures than before suggesting an overall increase in the distensibility of the lesion.

This effect is further supported by work conducted by Demer *et al* [51] when the distensibility of calcified lesions was shown to increase following ultrasound delivery. This was assessed by pressure-volume inflation curves from a standard dilation catheter as shown in Figure 2.9. Following the administration of ultrasound the inflation curve shifted to the right indicating increased distensibility and allowed standard balloon dilation at lower pressures.

This increase in distensibility is thought to be further increased during intervention and immediately afterwards by a phenomenon called vasodilation; the relaxation of the fibres in arteries in the vicinity of low frequency ultrasound [56]. This is thought to be a biological response and beyond the scope of this work but its effects are worth noting.

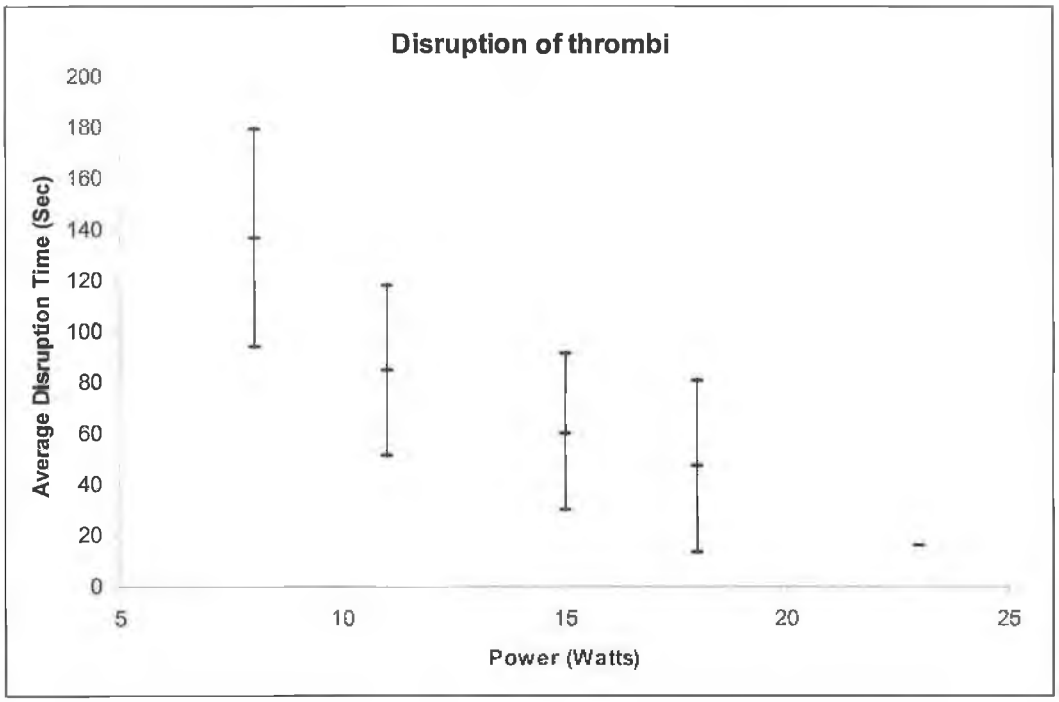

Figure 2.8: Average thrombi (n= 50) dissolution time *in vitro* for various acoustic horn distal-tip powers. Data digitised from Ariani *et al* [7] (using xyextract© digitising software

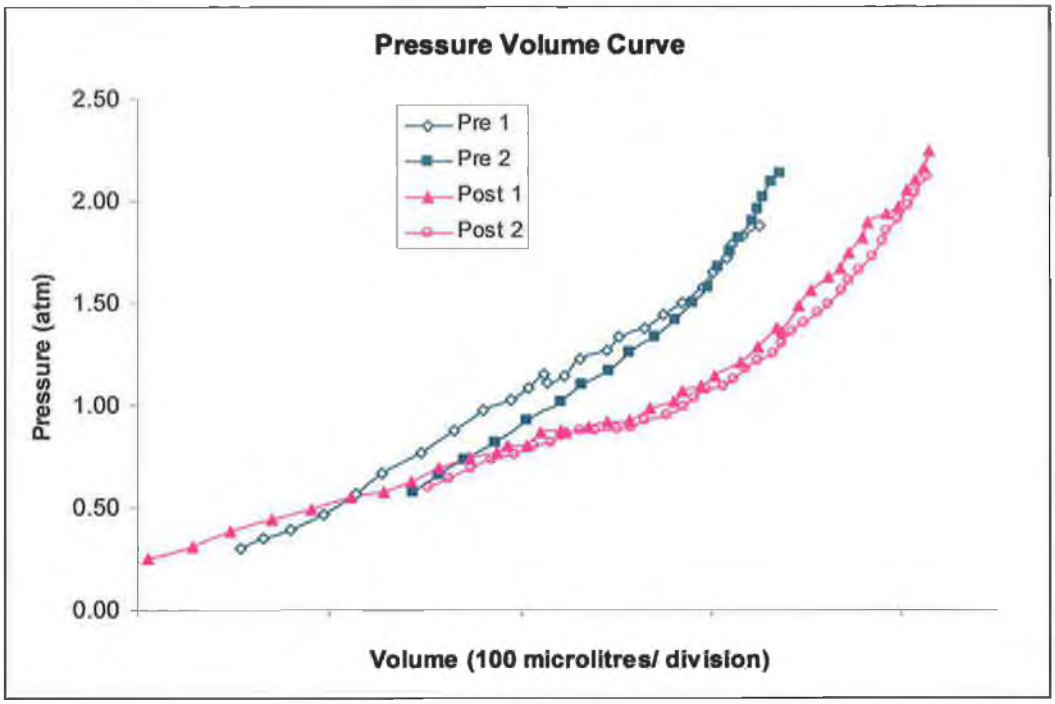

Figure 2.9: Example of pressure-volume curves obtained pre (left curves) and post (right curves) ultrasound energy application. The rightward shift indicates increased distensibility. Data digitised from Demer *et al* [51] (using xyextract© digitising software).

2.4 Theoretical Mechanics Background

The following review focuses on the response of a uniform rod (waveguide) to a harmonic input displacement and also how an oscillating sphere (distal ball-tip) affects the pressure field in the surrounding fluid.

2.4.1 Steady-state vibration of a uniform rod

The steady-state analytical solution of motion for an undamped longitudinally vibrating rod, as shown in Figure 2.10, subjected to a sinusoidal input vibration motion of $u(t) = b \sin(\omega(t))$ is shown in Equation 2.1 [65]. This is similar to the condition set up in ultrasound transmitted via a wire waveguide where the distal-tip of the acoustic horn applies a sinusoidal input of particular amplitude and frequency to the proximal end of the wire waveguide.

$$u(x,t) = b(\cos\frac{\omega x}{c} + \tan\frac{\omega l}{c}\sin\frac{\omega x}{c})\sin\omega t \qquad (2.1)$$

The steady-state amplitude of vibration at any point ($0 \leq x \leq l$) can be determined although this is an undamped solution and therefore limited. The solution can also be used in the determination of resonant response.

The solution for the resonant response from Equation 2.1 is shown in Equation 2.2 where f_n are the resonant frequencies of vibration for a thin rod of length l and where the speed of sound (longitudinal) in the rod material is c.

$$f_n = \frac{nc}{4l} \qquad n = 1, 3, 5... \qquad (2.2)$$

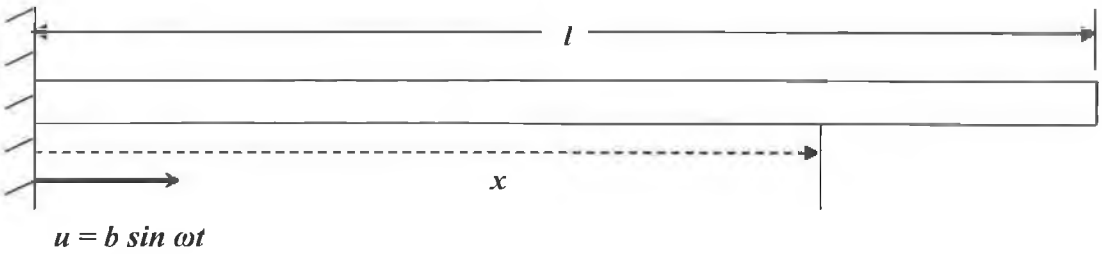

Figure 2.10: Diagram of a uniform rod, of length l, with an input displacement motion of $u = b \sin \omega t$. Adapted from Steidel [63]

Similarly, for a constant frequency Equation 2.3 gives us the lengths where resonance occurs (n = 1, 3, 5, 7...) and the lengths where non-resonance occurs (n = 0, 2, 4, 6, 8...). This is more important to the ultrasound wire waveguide as the displacement input from the distal-tip of the acoustic horn is at a constant prescribed frequency determined the ultrasonic generator.

$$l_n = \frac{nc}{4f} \tag{2.3}$$

2.4.2 Acoustic Pressure Field around an Oscillating Sphere

The literature describes ultrasound transmission resulting in vibration of the distal-tip of the wire waveguide and that the presence of a spherical or near spherical ball-tip enhanced transmission to the fluid [62]. An analytical solution exists for the pressure field developed in the fluid near to an oscillating sphere proposed by Morse [60] as shown in Equation 2.4 and Figure 2.11.

In this solution the maximum pressure at any point, P_{max}, developed in the field surrounding an oscillating sphere can be determined.

$$P_{\max} = 2\pi^2 \rho R f^2 d_0 \times \frac{R^2 |\cos\theta|}{r^2} \tag{2.4}$$

where f is the frequency of oscillation, d_0 is the displacement amplitude of oscillation and ρ is the fluid density. This solution shows that pressure amplitudes are at a maximum on the surface of the sphere and axially ahead of it.

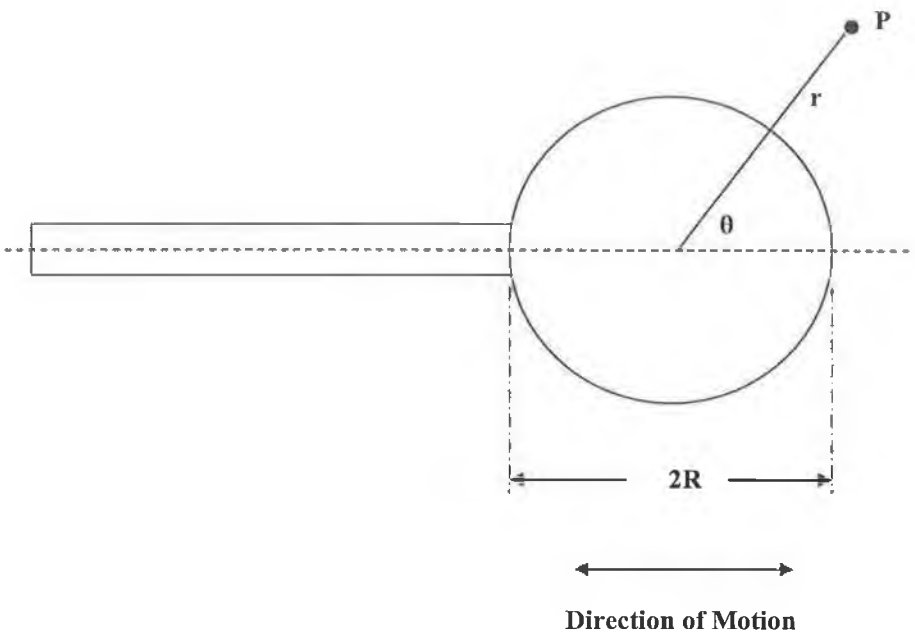

Figure 2.11: Diagram relating to the pressure field developed around an oscillating sphere. Adapted from Nyborg [58]

2.4.3 Cavitation

From the pressure amplitude field it is possible to infer when and where cavitation is likely to occur. While the occurrence of cavitation is dependent on numerous factors such as the temperature and the amount of dissolved gas in the fluid, Burdic [57] suggests a simplified cavitation threshold intensity, as shown in Equation 2.5.

$$T = \frac{P_{\max}^2}{2\rho c} \tag{2.5}$$

According to Perkins [54] this threshold intensity for degassed water at room temperature is approximately between 2 and 3 Watts/cm^2 in the frequency range of 20 – 30 kHz as shown in Figure 2.12.

It is worth noting here, that the acoustic intensity required to cause cavitation increases dramatically above a frequency of 100 kHz, as shown in Figure 2.12 and is one of the main reasons why sonochemistry and therapeutic ultrasound is performed at the low-frequency ultrasound bands of between 20 and 45 kHz.

2.4.4 Acoustic Streaming

Analytical solutions related to acoustic streaming phenomena that occur around a vibrating sphere are available in the literature [58, 59]. These primarily refer to the boundary layer thickness between the inner oscillatory motion and the outer acoustic streaming layer, as shown in Figure 2.6 and will not be discussed here in any great detail.

There is also, however, a solution for the velocity field of the outer streaming layer given by Lee and Wang [59] and this outer streaming layer can be observed experimentally [58].

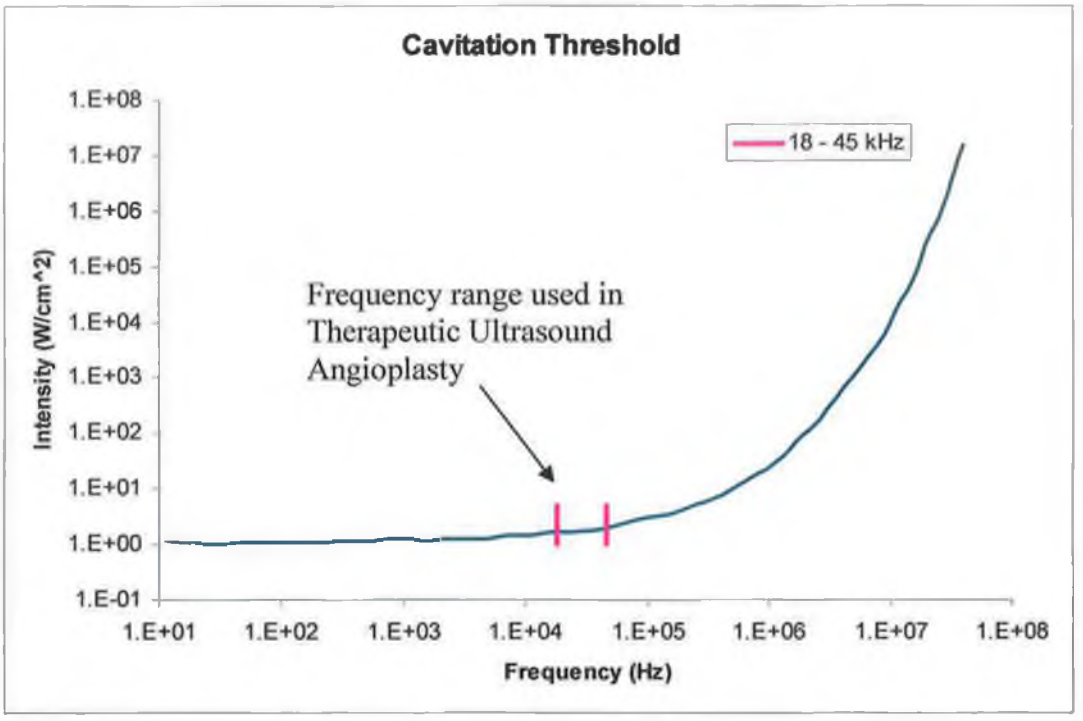

Figure 2.12: Cavitation threshold intensity for degassed water at room temperature. Adapted from Perkins [54] (using xyextract© digitising software).

2.5 Finite Element Analysis of Ultrasound Transmission in Wire Waveguides

While the theoretical analysis discussed provides valuable insight to the mechanics of ultrasound transmission via wire waveguide and through surrounding fluids, they are of limited use in analysing complex geometries and conditions.

The use of the finite element method may be of benefit in assessing effects such as the inclusion of specific distal-tip geometries on the waveguide, material damping in the waveguide and ultimately the modelling of various distal-tip shapes and their effects on the surrounding acoustic pressure field developed, with consequences for the ablation mechanisms

Further, the method may be applied to the coupling of the waveguide and surrounding fluid and modelling the acoustic fluid-structure behaviour of the system. No previous modelling of therapeutic ultrasound in small diameter wire waveguides or the coupling with a distal-tip fluid appears in the literature. This technique, however, has been used in the modelling of ultrasonic acoustic horns [66].

2.5.1 Material Properties

The relevant material properties required for the harmonic response modelling of a structure are the Young's Modulus (E) and the material density (ρ) in the calculation of mass [66, 67]. This follows the requirements of the analytical solution, as combined, these properties are used in the determination of the longitudinal speed of sound (c) in the material as shown in Equation 2.6.

$$c = \sqrt{\frac{E}{\rho}} \tag{2.6}$$

In acoustic fluid analysis the fluid properties required are the fluid density and the speed of sound in the fluid medium [68].

2.5.2 Mesh Density

Mesh density appears to be critical in the design of structures subjected to high frequency vibration due to the fact that as the resonant frequencies increase the wavelength decreases. Mesh density must be sufficiently high so that the structure has the degree of freedom to characterise the wavelengths of modes in the frequency range modelled.

Cunningham showed that, for an acoustic stub horn, insufficient mesh density results in the values for the resonant frequencies being predicted too high due to the structure being too stiff, poor mode shapes and incorrect stress determination [66].

2.5.3 Damping

The inclusion of a damping parameter is crucial in the modelling of structural harmonic response [66 and 67]. Johnson and Pal [69] describe the use of a simple constant damping value as being sufficient in acoustic horn modelling. This damping value can be determined by matching model response to experimentally determined data. This point will be developed further during the discussion of the development of the numerical model.

2.6 Summary

Calcified and totally occluded arteries pose significant complications during standard balloon angioplasty interventions and stent implantations. The use of therapeutic ultrasound transmitted via wire waveguides has been shown in initial clinical testing to be capable of disrupting thrombus, calcified and fibrous plaque without significant damage to healthy arterial tissue.

Potential end clinical benefits in the use of therapeutic ultrasound delivered via small diameter wire waveguides includes increasing distensibility of calcified plaques with the potential of reducing barotraumas and restenosis rates. This technology has also the potential in crossing chronic total occlusions, therefore allowing for standard balloon angioplasty and stent implantation to be used.

Little detailed analysis is provided on the design aspects of these devices or how ultrasonic displacements are delivered to the distal-tip of these small diameter wire waveguides at the frequencies and amplitudes required and the disruption mechanisms these cause. With the launch of products to the U.S. and European markets potentially imminent, sophisticated models for the design and optimisation of these devices are urgently required.

This challenge demands a combination of experimental investigation and computational modelling. A validated finite element model of the mechanical behaviour of a small diameter wire waveguide and it's interaction with surrounding fluids is necessary. Any such model would prove highly beneficial in determining the crucial wire waveguide distal-tip displacements and should be capable of predicting when the highly disruptive cavitation events occur. To date, no such model appears in the literature.

Bench testing of the ultrasonic wire waveguide technology on model materials is also necessary to help further understand the damage mechanisms involved with this technology.

Chapter 3

Design and Development of Ultrasonic Wire Waveguide Apparatus

3.1 Introduction to Apparatus Design

In order to conduct an experimental investigation of ultrasound wave transmission in a wire waveguide an apparatus capable of delivering ultrasonic displacements to the distal-tip of small diameter wire waveguides is required. Since ultrasonic wire waveguide medical devices are not yet commercially available, an apparatus was designed and developed as part of this project.

The objective was to produce a system with adjustable input power setting that delivers a range of displacements to the distal-tip of a wire waveguide, and which allows investigation of several different wire configurations. The apparatus is to consist of an ultrasonic generator, piezoelectric converter, acoustic horn and small diameter wire waveguides, with specific design requirements as shown in Table 3.1.

The ultrasonic wire waveguide apparatus will be used in further experimental testing and in the validation of numerical models, developed later in the thesis, that predict wire waveguide and the behaviour of fluid surrounding the distal-tip. The overall project plan is shown in Figure 3.1.

Table 3.1: Ultrasonic wire waveguide apparatus design requirements

Performance Characteristic	**Specification**	**Justification**
Frequency of Operation	20-30 kHz	Typical values used in clinical applications in the literature [7, 21, 51]
Wire waveguide diameter	0.35mm -1.0mm	Access to peripheral and coronary arteries, similar to standard guidewire dimensions and those reported in the literature [51]
Wire waveguide distal-tip displacement	Up to 100μm peak-to-peak	Typical values used in clinical applications in the literature [7, 21, 51]
Wire waveguide length	Up to 500mm	Allow for the testing of a range of lengths

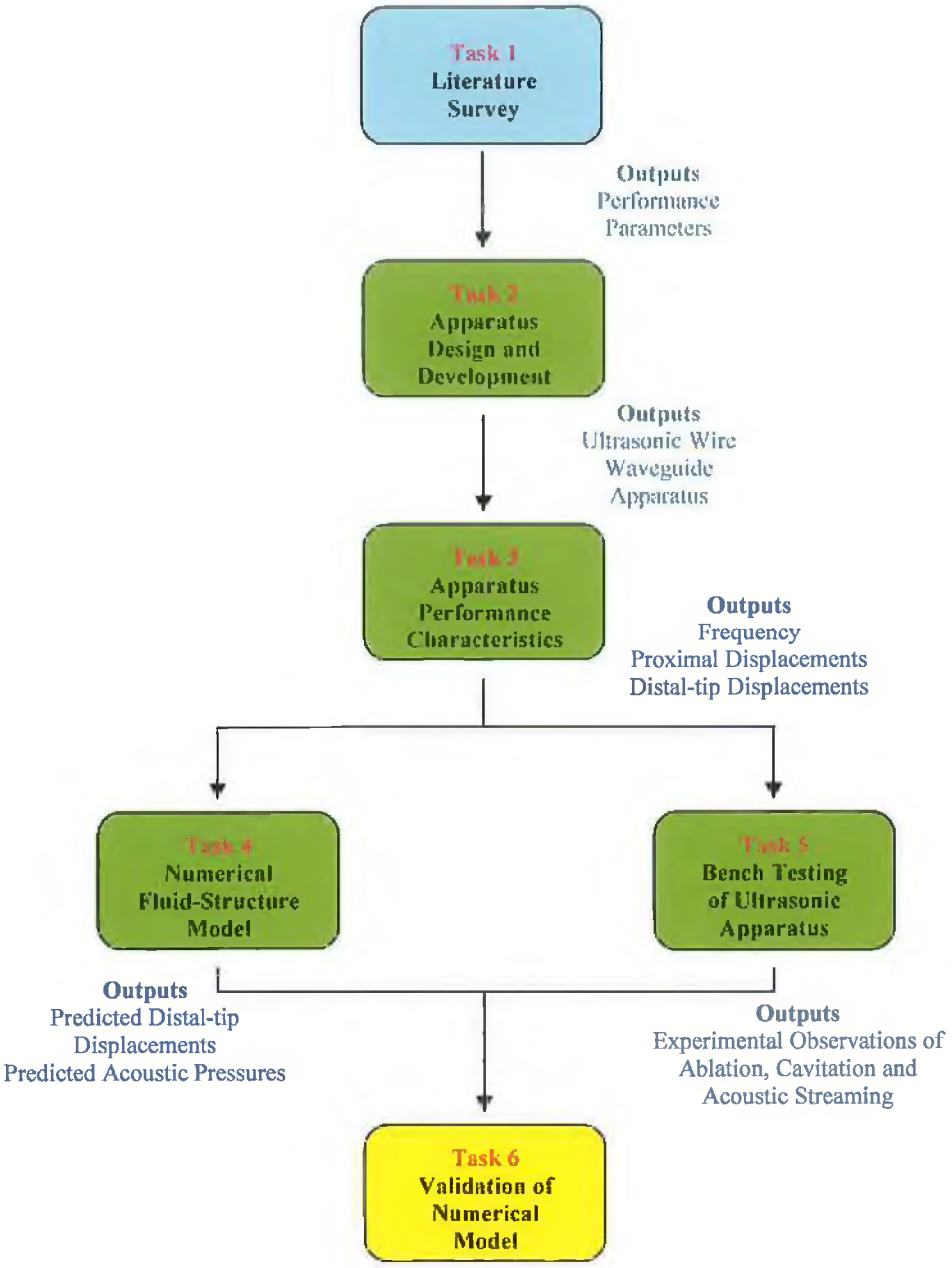

Figure 3.1: Block diagram of project plan

3.2 Ultrasonic Wire Waveguide Apparatus Design and Development

The ultrasonic generator and converter used in the development of the ultrasonic wire waveguide apparatus was a Sonifier 150D™ sourced from Branson Ultrasonics™ (41 Eagle Road, Danbury, CT, USA). This is a generator and converter package that is normally used in sonochemistry applications and features a wide range of acoustic horn tooling options.

3.2.1 Ultrasonic generator and converter

The system consists of an ultrasound generator that provides a sinusoidal voltage output (950 $Vrms_{max}$) at 22.5 kHz ± 6% [70]. The generator uses this flexibility in its output frequency to sweep and find the resonant frequency of the converter and horn combined for a wide band of loading conditions and is shown in Figure 3.2. This is an auto-tuning function and appears in many sonochemistry applications. This is due to the fact that during operation, heating and other phenomena can alter the resonant frequency of the system.

A system with this ability to sweep and find the natural frequency of the converter and horn is most beneficial for this work as minor alterations and attachments to the acoustic horn will not adversely affect ultrasonic transmission characteristics.

In addition, there are various input power dial settings that allow power delivered and therefore the displacement at the distal-tip of the acoustic horn to be controlled. Power can be activated via an on/ off switch on the generator or can be activated remotely via a switch on the body of the converter.

The generator also monitors root-mean-squared (rms) power delivered to the tip of the acoustic horn and displays this back to the user via a digital LCD display although these are often rudimentary power readings and for the consistent and accurate readings required in this work direct measurements of displacements will be made [54].

Figure 3.2: Image of Branson Ultrasonic Generator

The converter is a piezoelectric transducer (lead zirconate titanate) with an internal stack structure that is also designed to resonate at approximately 22.5 kHz and has a front-end mass that can accommodate a range of acoustic horns as shown in Figure 3.3 [70]. This allows us to specify an acoustic horn that has an amplification factor suitable to generate the longitudinal acoustic horn distal-tip peak-to-peak displacements within the range specified. This horn output will form the input displacement to the wire waveguide.

3.2.2 Acoustic Horn

In the selection of the acoustic horn the main factor of consideration was the output displacement amplitudes over the output power range when attached to the chosen ultrasonic converter. The majority of ultrasonic converter manufacturers provide acoustic horns specifically designed for their converters.

Of the acoustic horns available a titanium alloy horn (Branson™ Microtip 5 mm series) was most suited. This is an acoustic horn with a step and linear tapers and was chosen as it has a specified maximum output peak-to-peak of approximately 100μm at the resonant frequency of 22.5 kHz when connected to the piezoelectric converter [71] as shown in Figure 3.4.

Due to the internal displacements, stresses and heat developed, the acoustic horn can only be operated in a liquid environment which both cools and loads the distal-tip and cannot be operated in an unloaded condition such as in air [70]. The assembled acoustic horn and converter are shown in Figure 3.5.

3.2.3 Wire Waveguide Design

The wire waveguides used in the development of the apparatus are made from a Nickel-Titanium (NiTi) alloy obtained from Fort Wayne Metals© (9609 Indianapolis Road, Fort Wayne, IN 46809) and are used in guidewire technology due to their superelastic behaviour which allows greater flexibility for vascular access. Some authors have also shown that these wires, in their austenitic phase, also exhibit low damping similar to other metals and good sound transmission while

in their martensitic phase they have high damping properties [72, 73]. The material also shows an excellent biocompatible response.

3.2.3.1 NiTi Wire Waveguide

The particular nitinol alloy consists of 56%Wt nickel, some trace elements and the balance consisting of titanium (≈ 43%Wt). With this chemical composition the austenitic finish temperature (Af) for an ingot of the material is -10^0 Celsius [74].

However, following cold drawing and annealing, the austenitic finish temperature of wires is increased to approximately 16.5^0 Celsius, and it will therefore exhibit superelasticity and good transmission of sound above this value [74]. This grade of NiTi is commonly used in biomedical engineering for guidewire technology as it is in its austenitic phase at both room temperature and body temperature and can be tested at ambient or body temperature conditions.

Three wire diameters of 1.0 mm, 0.6 mm and 0.35 mm were sourced and used as waveguides. These were chosen as it was felt that the 1.0 mm diameter waveguide may be of benefit during testing while the 0.6 mm and 0.35 mm diameters would have flexibility closer to that required during surgical applications.

Mechanical testing was performed on the wires to establish material properties such as Young's modulus and material density and also to ensure that the wires were in their austenitic phase at room temperature; a requirement for low damping and good ultrasound transmission.

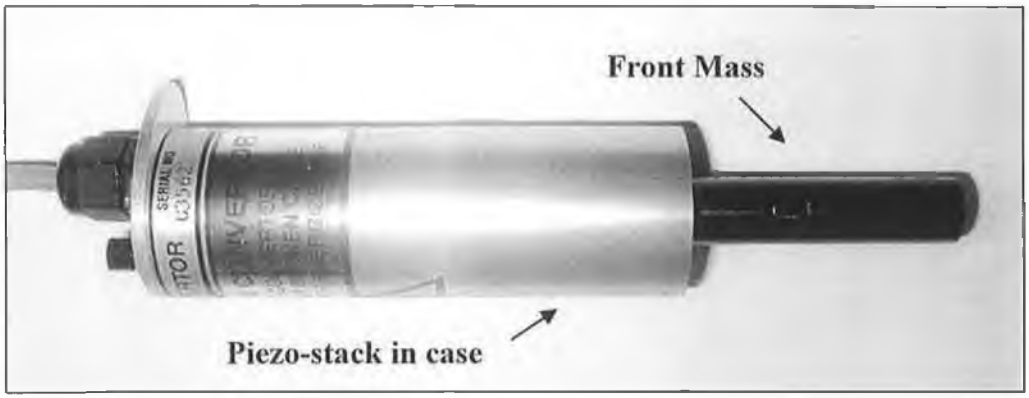

Figure 3.3: Image of Piezoelectric Ultrasonic Converter

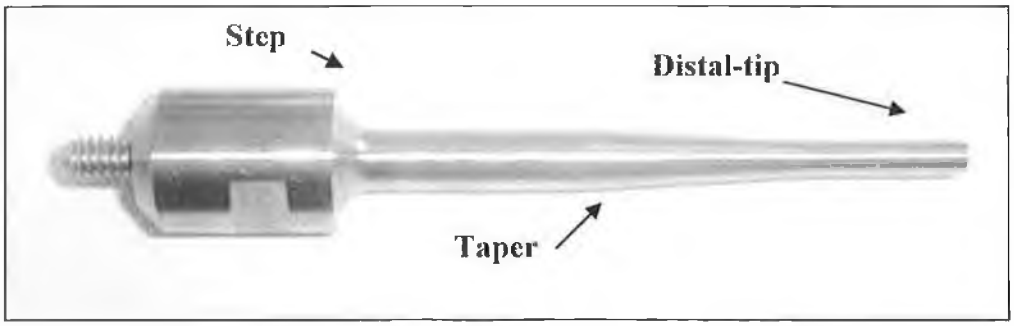

Figure 3.4: Image of Acoustic Horn

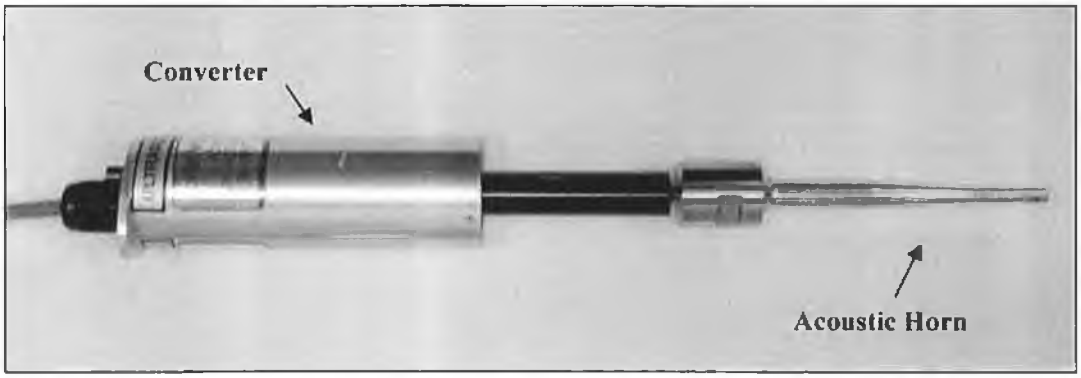

Figure 3.5: Assembled Acoustic Horn and Converter

Tensile testing of NiTi wire waveguide

Samples of the 0.35 mm and 0.6 mm diameter wire were subjected to tensile testing to failure. This testing was conducted with three goals in mind; 1) the determination of a Young's Modulus for the particular nitinol grade (useful in numerical simulation), 2) establishing the ultimate tensile strength and 3) ensuring the wire is in its austenitic phase at room temperature.

Wires were tested on a Hounsfield© H20K-W tensile testing machine at a crosshead speed of 2 mm/min and tests were conducted at room temperature (20^0 Celsius). Initially a 0.35 mm diameter wire was tested to failure to establish the presence of a stress loading plateau and the strain limits where the material begins to undergo a phase transformation from austenitic to a martensitic phase. This stress strain curve behaviour is a property of shape memory alloys in their austenitic phase and is best described in the results obtained in Figure 3.6 and is comparable with results reported in the literature [72, 73, 75].

Based on other work reported in the literature [73] the first linear stress-strain curve (highlighted in red) can be assumed to be the response of the material in its austenitic phase to loading and a Young's modulus of $\approx$ 75 GPa for small strains (less than 0.8 %) can be calculated. Above this value the material undergoes a phase transformation from its austenitic to martensitic phase along the stress-loading plateau of 600 MPa (highlighted in blue).

As strain is increased along this plateau the material moves to complete martensitic phase that finally ends at a strain of 6 %. Once the transformation in phase is complete the wire waveguide behaviour returns to a linear stress-strain response with a martensitic Young's modulus of $\approx$ 30 GPa (highlighted in green).

The complete stress-strain response for a 0.6 mm diameter wire for multiple load cycles is shown in Figure 3.7. In this test the wire was loaded into its martensitic phase (strain = 8.5 %) and unloaded to an unstressed condition. Two load cycles were completed with the third and final cycle loading the wire to failure. These results show that the wire can undergo large strains up to 1.0 % while remaining in its elastic range although there is some permanent set strain of approximately 0.16 %. It is this elastic response over large strains that allow the

wire to exhibit superelastic properties ideal for access through the vascular structure.

The results of the tensile testing of the wires provide much useful information. Providing strains are small (< 0.8 %) the wire will remain in its austenitic phase, exhibit low damping and good sound transmission, and have a Young's modulus of approximately 75 GPa. Over-straining of the wire in bending or through ultrasound transmission would result in the wire transforming to its martensitic phase with the resulting high damping properties and poor sound transmission. The overall results show that the wire has an ultimate tensile strength of 1400 MPa.

Material density of NiTi waveguide

Another important material property that is required in both the analytical and numerical modelling of the waveguide is the density of the Nickel-Titanium. Density measurements were performed with a LabQuip© Sartorius Density Measurement Kit. The density of the material was found to be 6448 kg/m^3.

This value for material density, the Young's modulus in the austenitic phase and the strain at which phase transformation begins all compare closely with the supplier's data sheet for Nitinol [75].

3.2.4 Connection of wire waveguide to acoustic horn

The connection of the wire waveguide to the acoustic horn is critical as a rigid connection is required to ensure the proximal end of the wire waveguide moves with the distal end of the acoustic horn. This guarantees that controllable ultrasonic displacements are input into the wire waveguide.

As the acoustic horn is designed to operate at resonance of approximately 22.5 kHz any connection method must not adversely alter this resonant frequency of operation. Given the ability of the generator to automatically tune to ± 6% of the resonant frequency some alteration is acceptable and inevitable to achieve good connection.

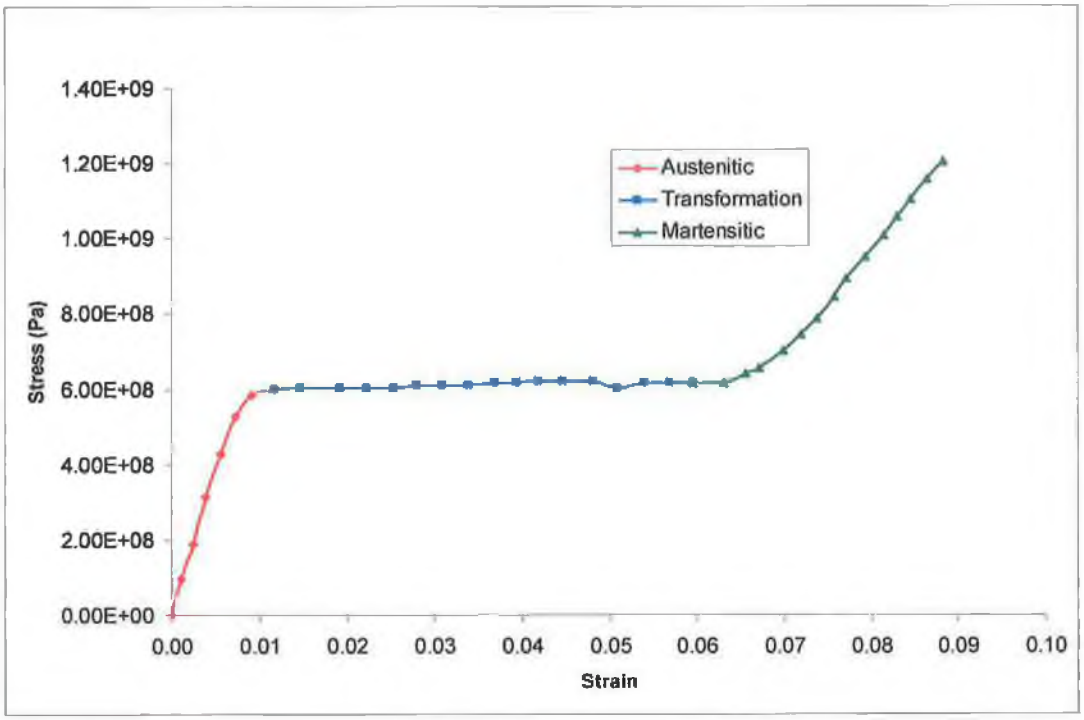

Figure 3.6: Stress strain curve for 0.35mm diameter NiTi wire showing both austenitic and martensitic properties

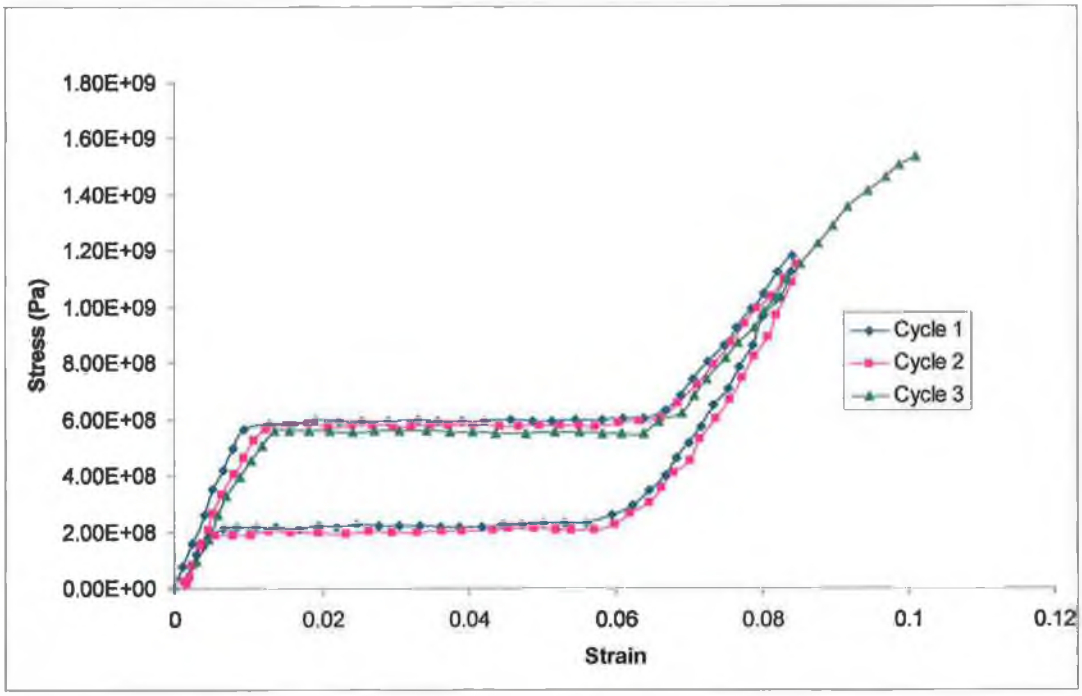

Figure 3.7: Cyclic stress-strain curve for 0.6mm diameter NiTi wire showing superelastic response over large strains

This requires that the alterations due to the connection method add negligible mass when compared with the overall mass of the acoustic horn. It must also be of negligible size in order not to affect the resonant length of the horn and the connection method must not impart large stresses that may affect the operational resonant frequency.

3.2.4.1 Evaluation of wire waveguide connection method

A number of connection methods were evaluated by attaching the three waveguides of diameter 1.0 mm, 0.6 mm and 0.35 mm to the distal end of the acoustic horn and characterising performance based on time to failure, location of failure and a qualitative assessment of overall observed acoustic transmission, based on the fact that poor transmission results in notable power fluctuations at the generator and is accompanied by a change in sound [70].

Figure 3.8 shows the experimental rig used to evaluate the various connection methods. This rig allowed the acoustic horn, a small length of waveguide and a connection configuration to be submerged into a beaker of water. This allowed the converter to be powered while the acoustic horn remained partially submerged in the water for cooling and loading.

Initially, the acoustic horn was powered in the water with no wire or connector to establish baseline horn performance. For a generator input power dial setting of 1.5, fluid disturbances were observed in the water directly ahead of the distal-tip. The noise generated was consistent and power reading remained constant throughout the 30 second test.

The testing of various wire waveguide connection methods consisted of running the horn and connected waveguide at a generator input power dial setting of 1.5 until the connection failed. Time to failure was measured and acoustic transmission was determined by examining fluid disturbance in the regions highlighted in red, as shown in Figure 3.9, ahead of the acoustic horn distal-tip and the distal-tip of the wire waveguide. In addition, the location of failure was recorded.

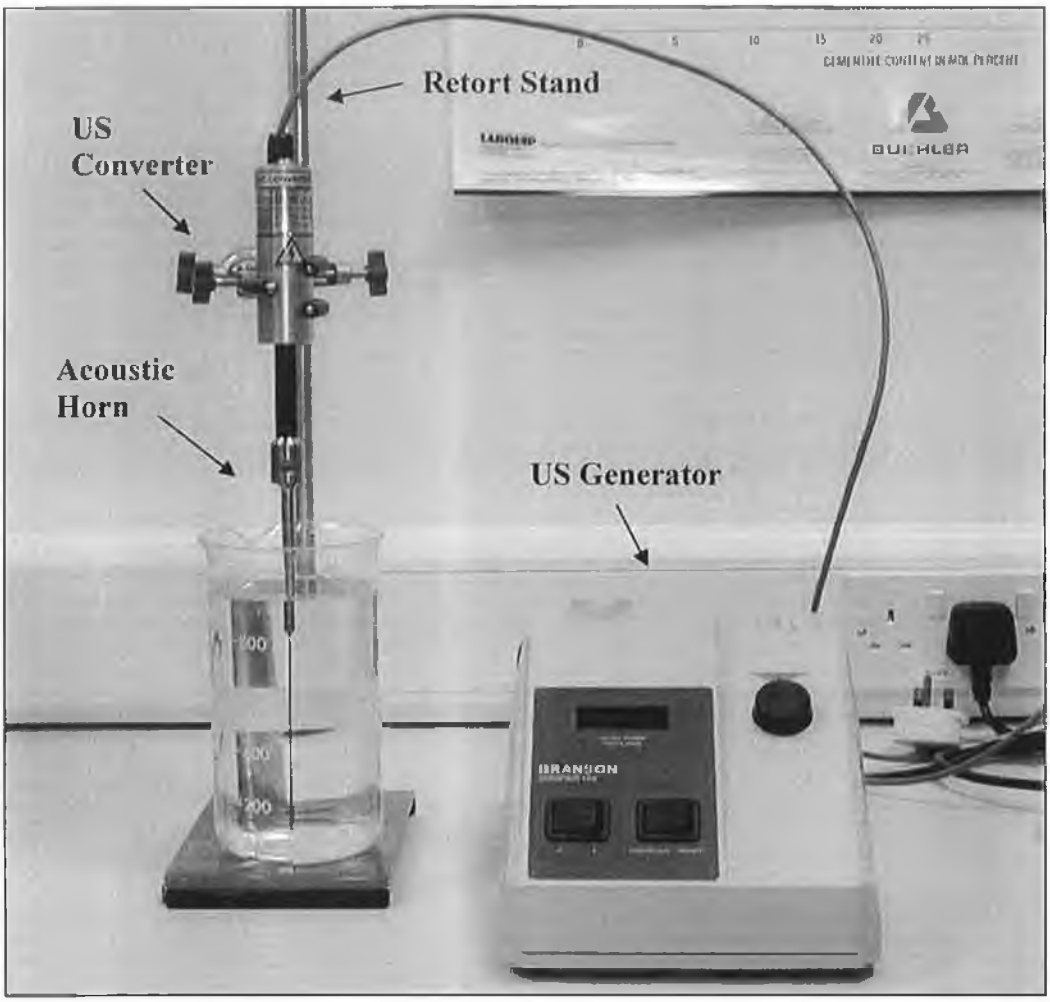

Figure 3.8: Test –rig for the evaluation of wire waveguide connection methods.

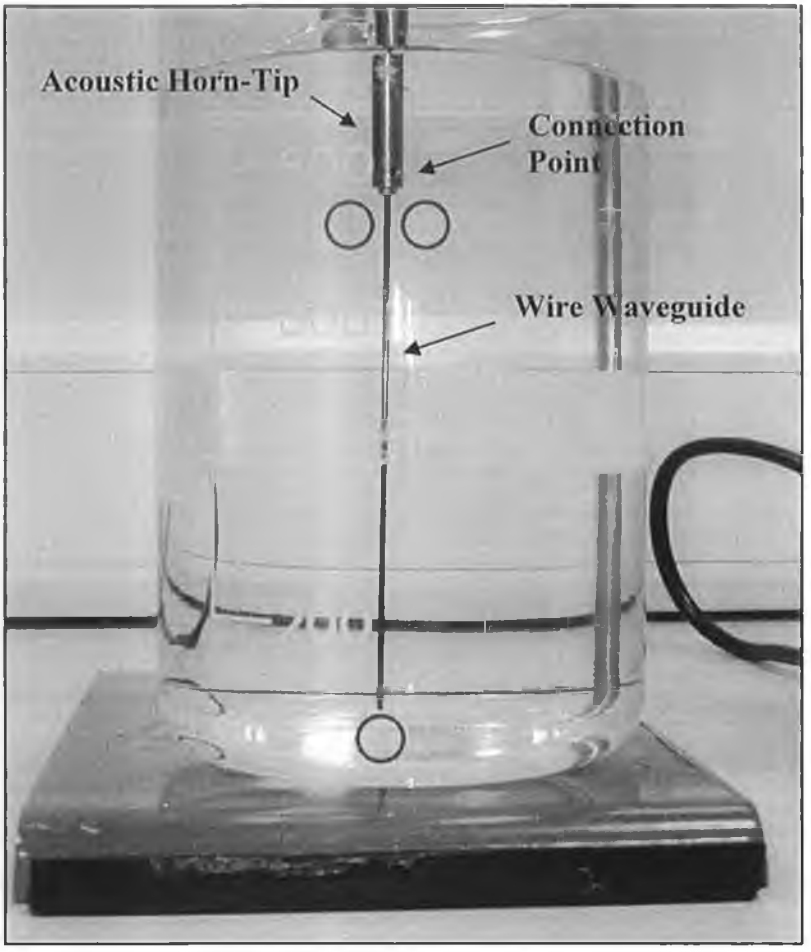

Figure 3.9: Evaluation of wire waveguide connection methods. Acoustic horn and waveguide; shown submerged in beaker of water at room temperature. Red circles mark areas of fluid disturbance.

Single side set-screw

The first connection method was established by drilling a 2 mm diameter hole into the radiating face of the acoustic horn to a depth of 10 mm. The waveguide was inserted into this hole and held in place by a M2 side set-screw as shown in Figure 3.10 and Figure 3.11.

This method of connection resulted in the wire waveguide being held firmly in place between the side set-screw and pit-hole as shown. This resulted in the wire exiting the face of the horn at an angle as shown in Figure 3.11. The single set-screw connection method was tested for all three wire waveguide diameters in the test rig.

From initial testing it was observed that certain lengths (35 mm - 45 mm) of wire waveguide within the beaker resulted in poor ultrasound transmission while other lengths (60 mm - 80 mm) transmitted well. Also, the side set-screw was vibrating out of the side-hole and losing grip of the wire. Based on these initial findings all wires tested for all connection methods were approximately 70 mm in length and where side set-screws were used they were fastened in place with the addition of a retaining compound (Loctite™ Retaining Compound '601') to prevent loosening due to vibration.

The time-to-failure results from testing the side set-screw connection method are shown in Figure 3.12 for all three wire waveguide diameters (each group: n=5). In addition to these results the following observations were made.

Wires sustained crimping damage when being fixed into the horn by the side set-screw as shown in Figure 3.13 and following application of ultrasound all wires failed (n=15) at this connection point where the side set-screw crimped the wire waveguide. From samples recovered failure was shown to occur at the screw edge closest to the tip of the horn and can be seen in Figure 3.13.

The 1.0 mm diameter waveguides lasted longest but overall transmission was poor (based on observation as mentioned), as was the case with the 0.6 mm diameter wires. The 0.35 mm diameter failed in the shortest time but transmission was good.

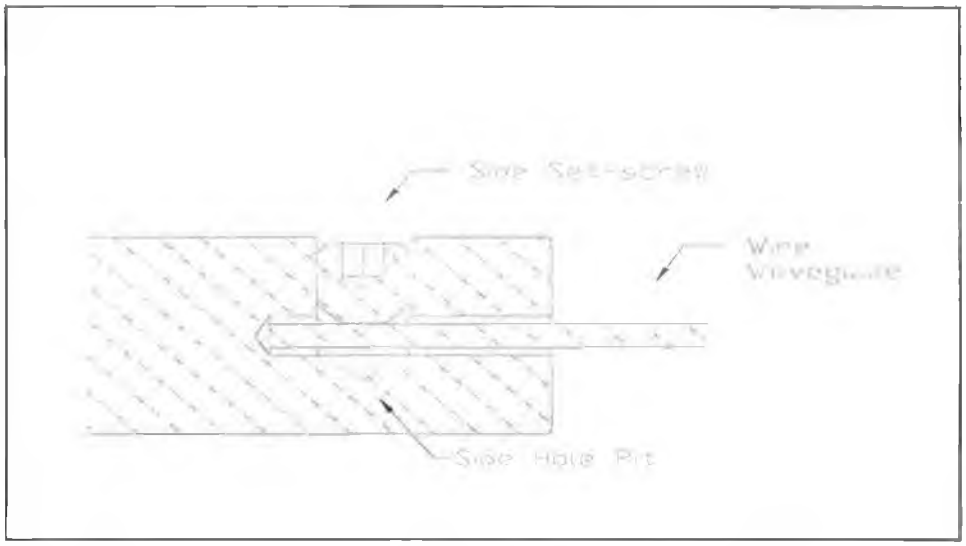

Figure 3.10: Drawing of single side set-screw connection method

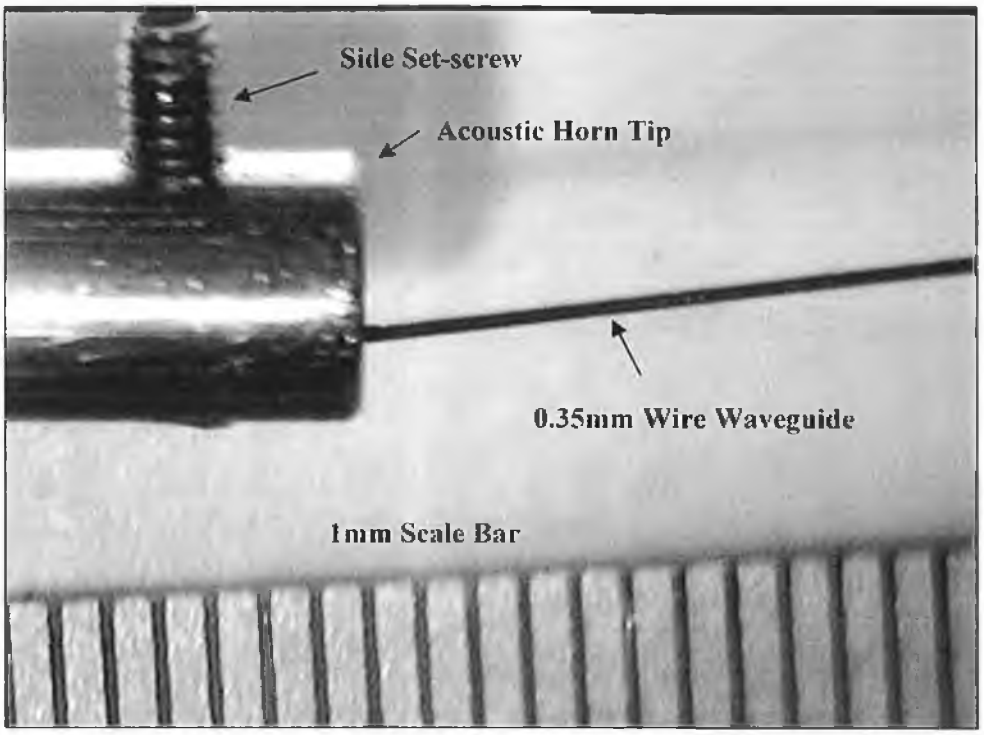

Figure 3.11: Image of single side set-screw connection method

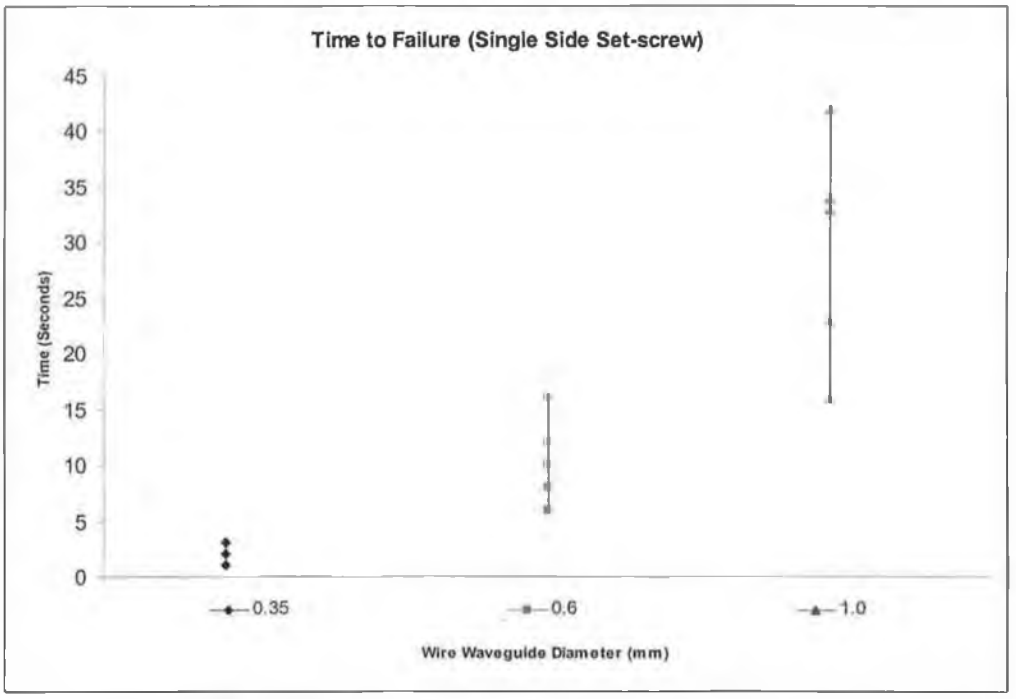

Figure 3.12: Data of time to failure for all three diameter wire waveguides for single side set-screw connection method

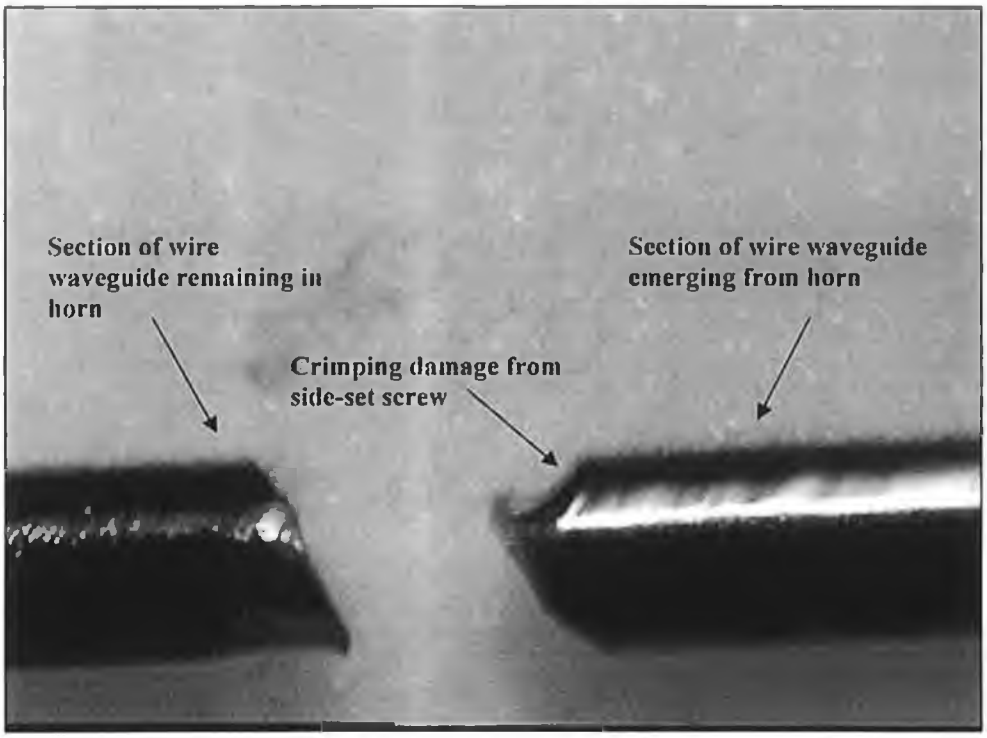

Figure 3.13: Image of failed 0.6mm wire waveguide following application of ultrasound.

Due to the single side set-screw connection method the wire exited the distal-tip of the horn at an angle and a transverse wire motion was observed with the 0.35 mm wire and to a lesser extent the 0.6 mm diameter waveguide. The time-to-failure results were highly variable and this may be due to variations in initial crimping forces.

Based on this evidence it was hypothesised that failure was primarily due to damage sustained to the waveguide during fixing into the horn. When ultrasound was applied, this point became a stress concentrator and subsequently all failures occurred at this location.

The transverse motion of the wire may have further fatigued the wire waveguide at this location. One of the reasons the larger diameter wires lasted longer may be due to the fact that less crimp damage was sustained as a percentage of cross-sectional area during fixing to the horn and also the greater bending stiffness reduced transverse motion. The use of a second side set-screw was considered as a potential solution to both these problems.

Double side set-screw

In order to address the issue of the wire exiting at an angle and the resulting transverse motion a second side set-screw was used to hold the wire waveguide in place as shown in Figures 3.14 and 3.15. It was also envisaged that this method would hold the wire over a longer length with less localised crimp damage.

The time-to-failure results from the tests conducted on the three wire waveguide diameters (each group: n=5) are shown in Figure 3.16 and the following observations were made

All wires waveguides failed (n=15) at the point where the two side set-screws gripped the wire. Failure was consistent with the type of failure observed in the single side set-screw method. Transverse motion was observed once again with the 0.35mm wire waveguide.

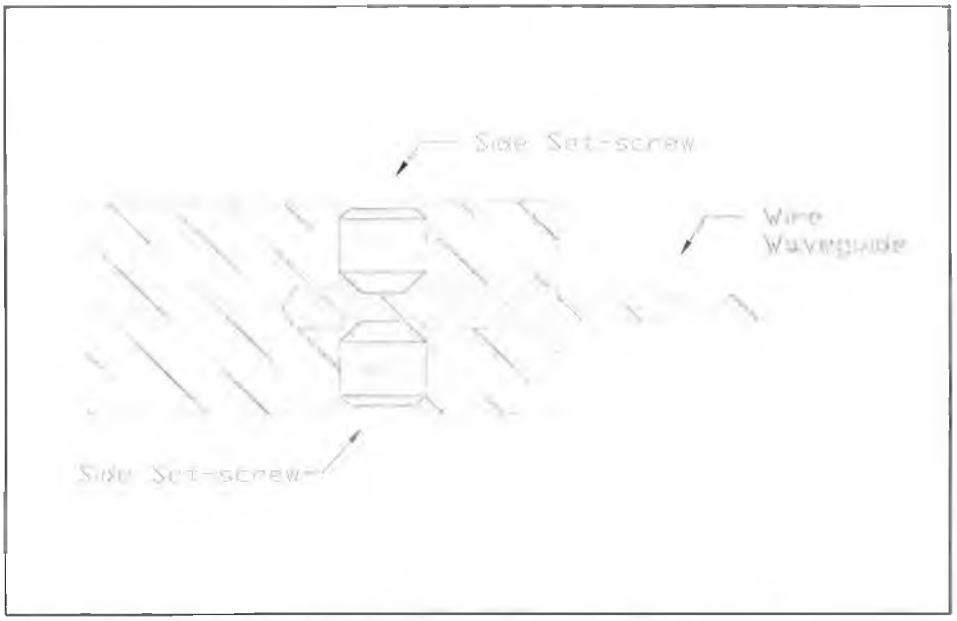

Figure 3.14: Drawing of double side set-screw connection method

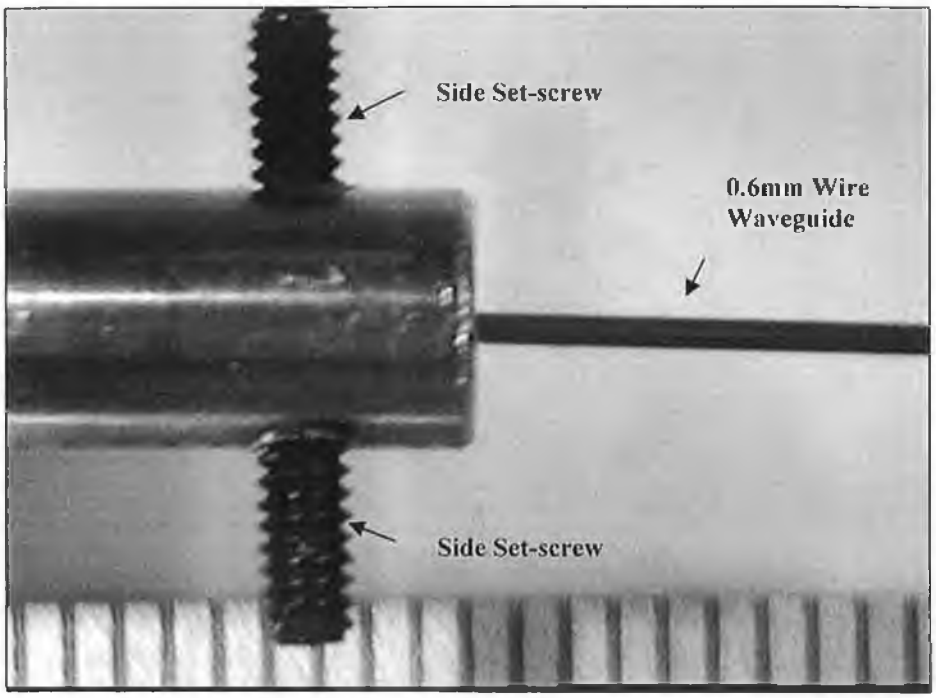

Figure 3.15: Image of double side set-screw connection method

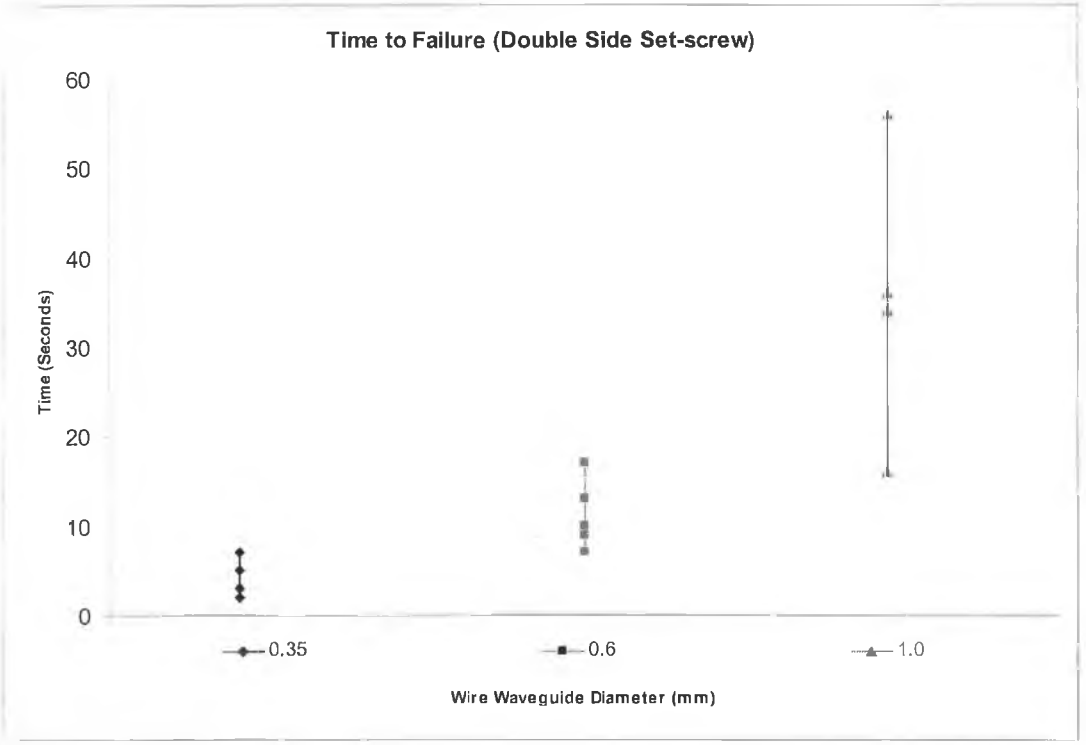

Figure 3.16: Data of time to failure for all three diameter wire waveguides for double side set-screw connection method

The 0.35 mm diameter waveguides showed good transmission to the fluid while little fluid disturbance and power fluctuations were observed with the 0.6 mm and 1.0 mm waveguides. Overall time to failure was increased slightly but results were once again highly variable.

Axial set-screw

The results of time to failure for the single and double side-set-screw connection methods showed that all wires failed in less than 60 seconds. This time would be insufficient to perform tests on the wires such as optical displacement analysis or bench testing on model materials, and is not a basis for an operational device.

The idea to use a screw coupled directly into the radiating face of the horn was based on the method by which the horn itself is attached to the front mass of the converter. The wire waveguide was first crimped into an axial hole in a stainless steel M3 set screw and then screwed into the radiation face of the horn as shown in Figures 3.17 and 3.18.

The time-to-failure results from the tests conducted on the three wire waveguide diameters (each group: n=5) are shown in Figure 3.19 and the following observations were made

All wire waveguides showed excellent transmission of ultrasonic energy based on steady power-reading and fluid disturbance in the regions ahead of the horn and waveguide tip. All failures (n=14), with the exception of one, occurred at the point where the wire waveguide exited the axial crimp screw as shown in Figure 3.20. The other wire (n=1) failed 3 mm from the connection point.

Overall times to failure improved dramatically as shown in Figure 3.18 with the 1.0mm diameter wire waveguide (n=3) lasting 300 seconds before the test was terminated. Time to failure for the 0.35 mm and 0.6 mm diameter wire waveguides were still less than 60 seconds

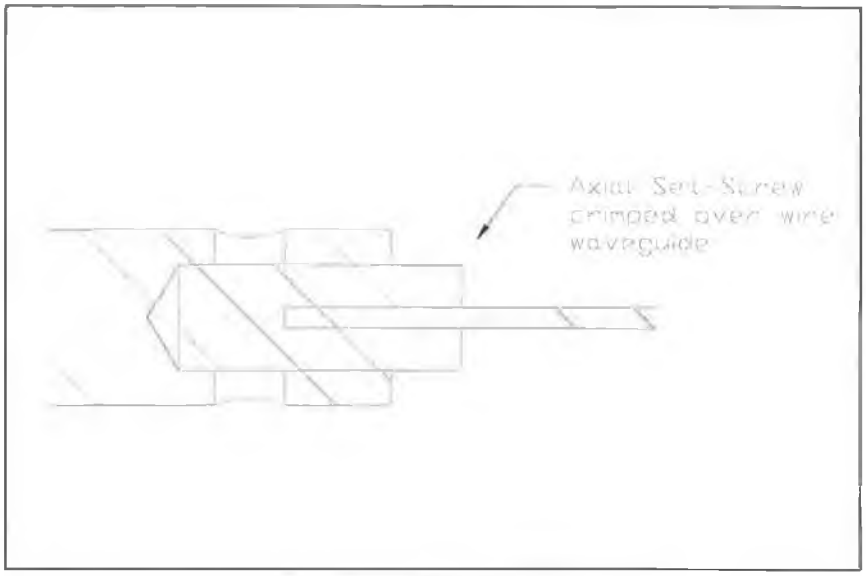

Figure 3.17: Drawing of axial crimped set-screw connection method

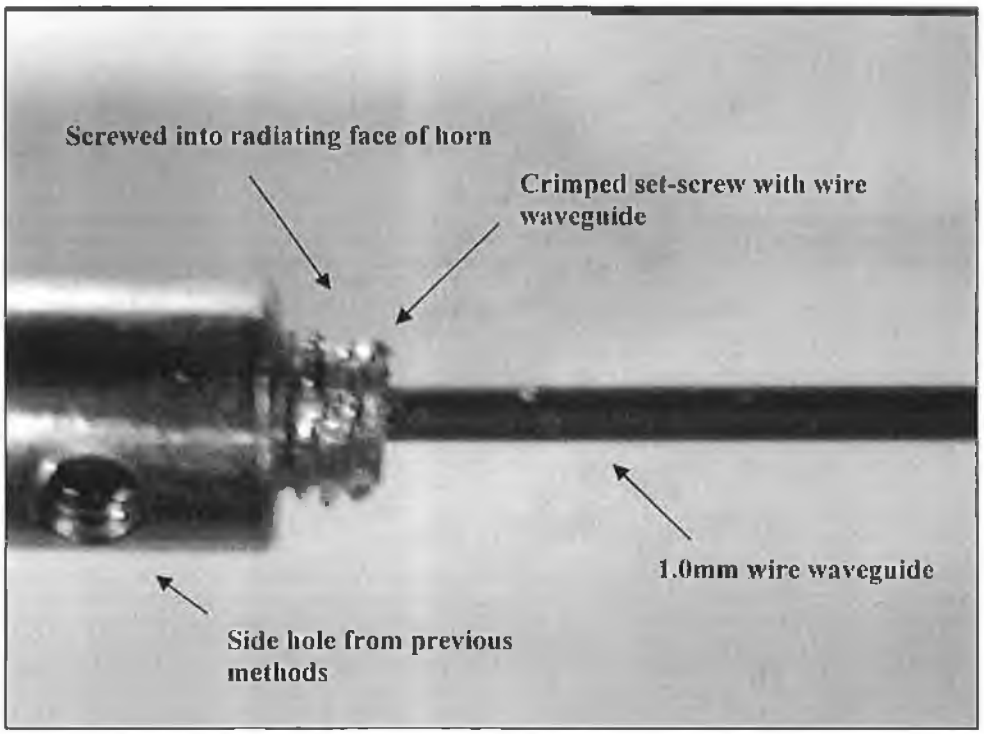

Figure 3.18: Image of axial crimped set-screw connection method

It appears that the bending stiffness of the 1.0 mm diameter wire waveguide near the connection point and the fact that crimping damage from the screw was minimal allowed the wire to transmit ultrasound for longer periods of time. To improve time to failure for the 0.35 mm diameter wire waveguide a stainless steel 0.6 mm outer diameter sleeve was incorporated over the wire at the connection point with the axial crimp screw as shown in Figure 3.21.

The sleeve and wire were bonded together with a retaining compound (Loctite© Retaining Compound '601'). Overall time to failure was examined both with and without the housing, as shown in Figure 3.24, and results improved with this connection method. Further, no transverse motion near the connection point was observed.

3.2.5 Final apparatus design and housing

Based on the experimental testing of the horn and connection methods the main functions of the housing was to encase the apparatus in a lightweight unit that protects the user from contact with the converter and acoustic horn and provide an inner casing for the cooling of the acoustic horn and connection method similar to the test-rig. Any design would allow the wire waveguide to emerge from the housing in a catheter and assist in minimising unwanted transverse vibrations in the emerging waveguide.

Figure 3.22 shows a detailed drawing of the final apparatus design. The design consists of inner casing or cooling jacket that allows a fluid reservoir to be maintained around the distal-tip of the acoustic horn where the wire waveguide is connected. This is similar to conditions on the test-rig.

A female connector is located at the distal section of the inner cooling jacket where the wire waveguide emerged. This connector prevents transverse motion of the waveguide near the connection point and can accommodate a medical grade catheter that contains the emerging waveguide.

An outer casing is used to contain the acoustic horn and cooling jacket and is connected to the converter's body by means of aluminium support. Figure 3.23

shows an image of the overall completed apparatus both in its exploded and assembled views.

Following final design and assembly of the apparatus the three wire waveguide diameters were tested in the apparatus using the axial crimp screw connection method. Transmission performance was based on the same criteria established on the test rig and all tests were terminated after 300 seconds.

Figure 3.24 shows the results for all three wire waveguide diameters including the connection method of the 0.35 mm wire waveguide with a sleeve as discussed.

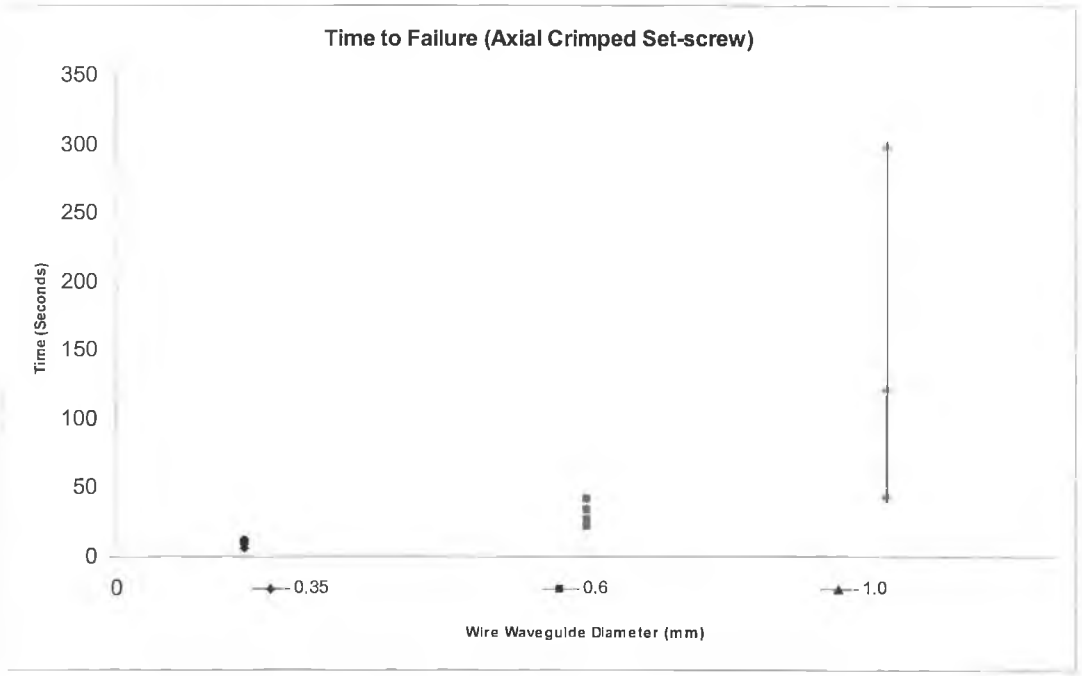

Figure 3.19: Data of time to failure for all three diameter wire waveguides for axial crimped set-screw connection method

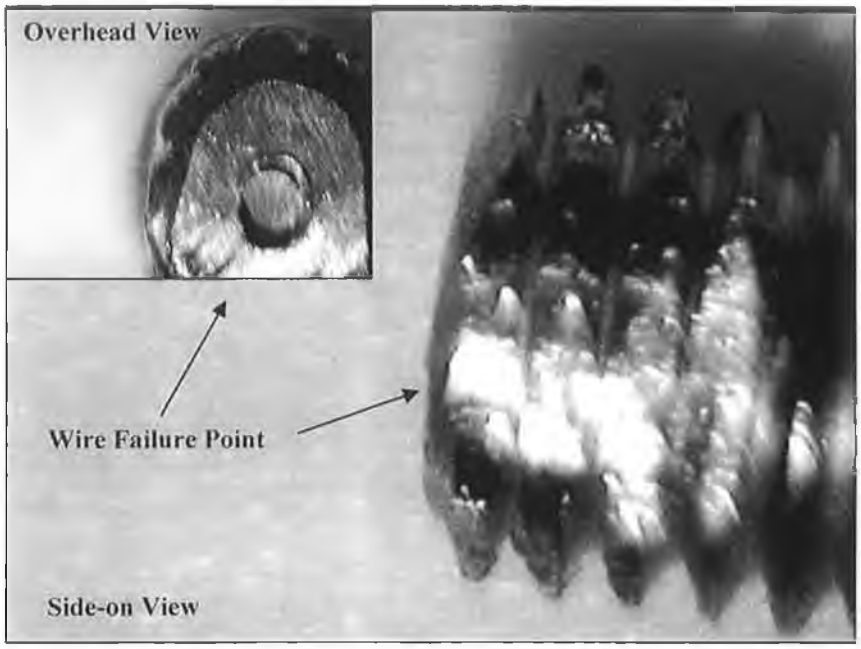

Figure 3.20: Image of failed 0.6mm axial crimped set-screw connection method

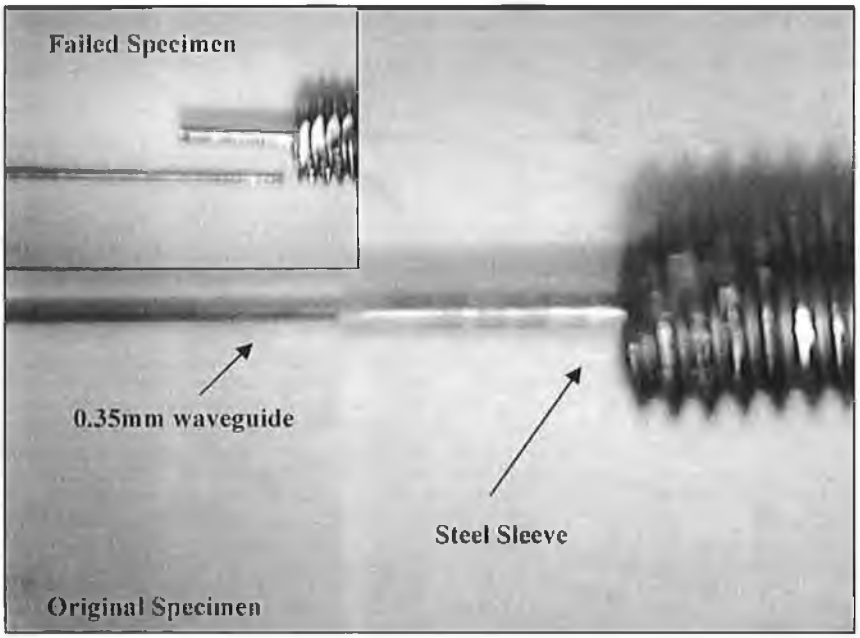

Figure 3.21: Image of 0.35mm diameter wire with axial crimped set-screw and sleeve connection method. Also shown (inset) is the failed wire.

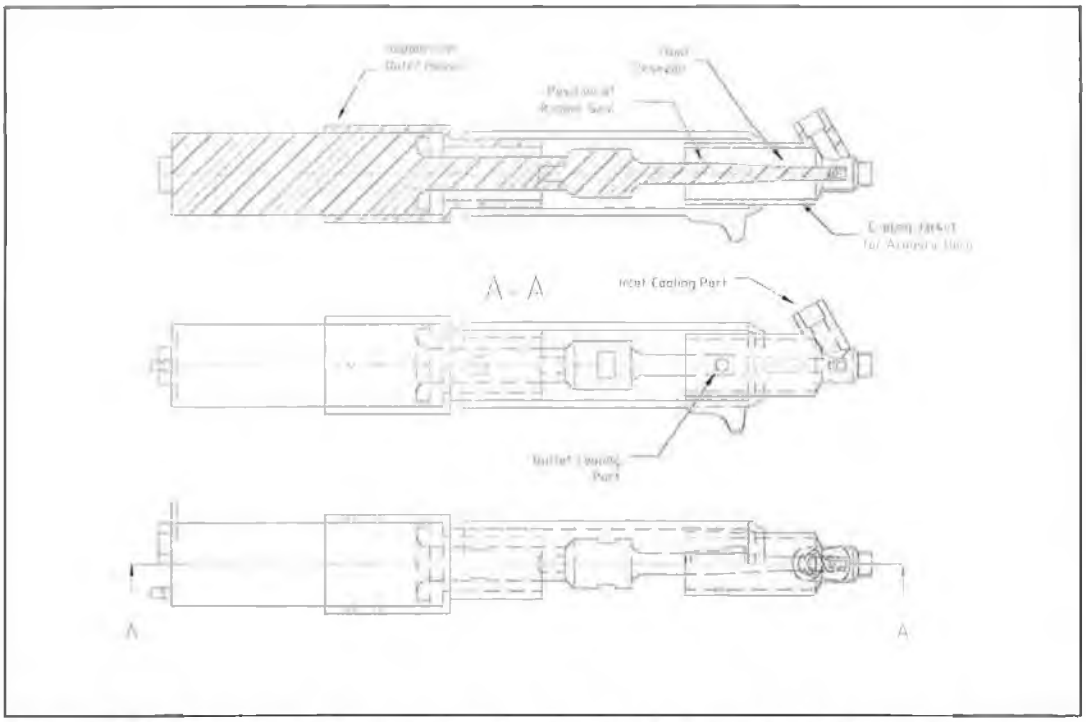

Figure 3.22: Drawing of ultrasonic wire waveguide apparatus in housing

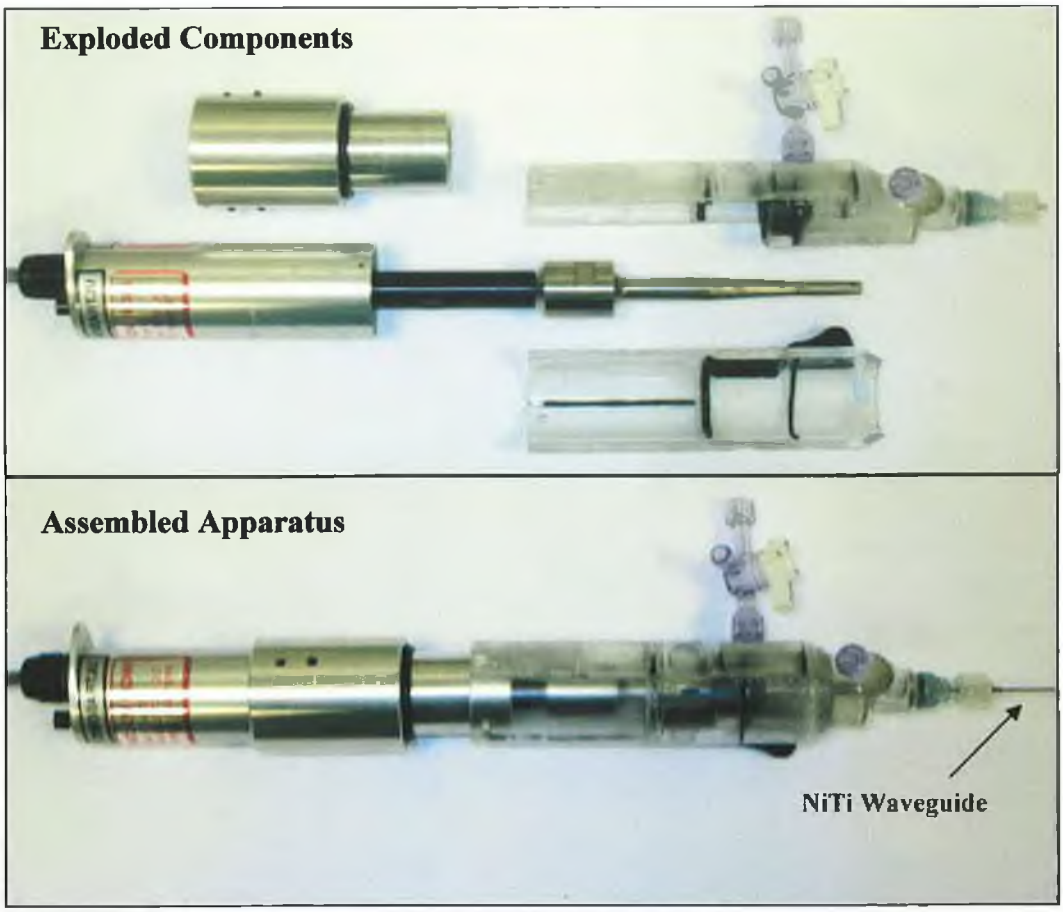

Figure 3.23: Image of final ultrasonic wire waveguide apparatus in its housing with catheter emerging.

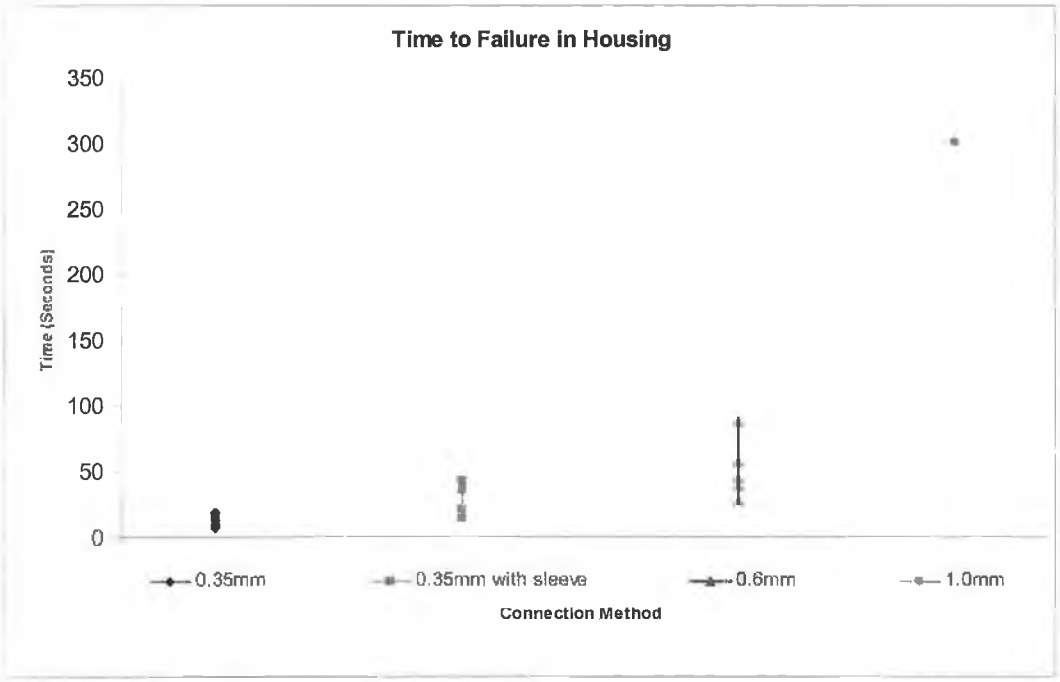

Figure 3.24: Data of time to failure for all three diameter wire waveguides for axial crimped set-screw connection method in apparatus housing

3.3 Summary

An experimental apparatus capable of delivering ultrasonic vibration to the distal tip of small diameter NiTi wire waveguides has been developed. The connection of the wire waveguide and the acoustic horn proved extremely difficult due to the excessive number of wire failures.

The apparatus configuration using an axial crimp screw connection in conjunction with a 1.0 mm diameter waveguide can transmit this ultrasonic energy to the distal-tip for a time exceeding 300 seconds and appears suitable for further performance evaluation testing.

The reliability of the performance with the 1.0mm diameter waveguide may be due to the increased bending stiffness the wire provides near the connection. This reduces unwanted transverse vibration. Also the axial crimp screw connection method grips the wire relatively uniformly with less crimp damage.

With the 0.6 mm and 0.35 mm diameter waveguides, time to failure was less than 90 seconds and while the 0.35 mm diameter wire waveguide may have suitable dimensions for vascular access, testing these waveguides may prove difficult due to excessive failures.

A tapered wire waveguide, discussed in more detail in Chapter 6, may address this issue as it would have sufficient bending stiffness and cross sectional area at the connection point and could taper to diameters more suited to cardiovascular surgery.

Experimental testing to establish performance characteristics and numerical modelling is required, however, to determine displacement amplitudes, frequency of operation and stresses in the wire waveguide due to this form of energy. This will be further discussed in Chapters 4 and 5.

Chapter 4

Performance Characteristics of the Ultrasonic Wire Waveguide Apparatus

4.1. Introduction

The goal of the experimental performance testing programme is to determine the important operating parameters of the ultrasound wire waveguide apparatus such as the displacements applied to the proximal end of the waveguide by the acoustic horn, the frequency of operation and the wire waveguide distal-tip displacements . This will be achieved by direct measurement, using an optical microscope, of the peak-to-peak displacements, both, at the distal-tip of the wire waveguide and over the length of the waveguide for the ultrasonic wire waveguide apparatus described in Chapter 3.

These optical measurements will allow us to examine the distal-tip displacements for a range of generator input power dial-settings, and also how these displacements are affected by varying the length of the wire waveguide. These measurements, both at the distal-tip and along the waveguide length, will also allow the input displacements for various input power dial-settings to be estimated.

Indirectly, these peak-to-peak displacement measurements and the wire length associated with resonance and non-resonance can be used in conjunction with analytical methods to estimate the frequency of operation of the ultrasonic wire waveguide apparatus.

Parameters such as the applied displacements to the proximal end of the wire waveguide and the frequency of operation will form the input conditions to any numerical model used to predict waveguide behaviour. Distal-tip displacements

can be used to validate the numerical model and also in estimating the damping characteristics of the waveguide.

4.2. Direct peak-to-peak displacement measurement

The wire waveguide performance characteristics were determined by the optical measurement technique. This involves direct measurement of the peak-to-peak displacements at any location along the length of the waveguide by means of an optical microscope, digital camera and PC with image analysis as shown schematically in Figure 4.1.

4.2.1. Displacement measurement technique

Using this optical technique the distal-tip peak-to-peak displacement is measured by focusing the optical microscope on the distal tip of the wire waveguide in its non-energised or stationary position. Once ultrasonic energy is applied to the waveguide the rapidly vibrating distal-tip streaks an image on the camera and can be captured. The length of the streak can be measured manually using calibrated measurement software showing the extent of its displacement, the peak-to-peak displacement as shown in Figure 4.2.

When determining the peak-to-peak displacement of any location along the length of the waveguide, an initial mark is identified and its length measured in the stationary condition. This mark can be a small metallic fleck on the wire, an imperfection or blemish on the wire surface. Once again when ultrasound is passed into the waveguide this mark produces a streaked image whose length can be measured as shown in Figure 4.2. The total peak-to-peak displacement is given by:

$$Total\ Displacemen\ = Streak\ Length - Initial\ Length$$

The system used in the measurement of the wire waveguide displacements is shown in Figure 4.3. It consists of an optical microscope (SPS laboratories), a digital colour camera (Vantage 'VGC400') and a PC with image analysis software (Image Analysis System, Buehler) and with multiple objective lenses with up to 80 times magnification.

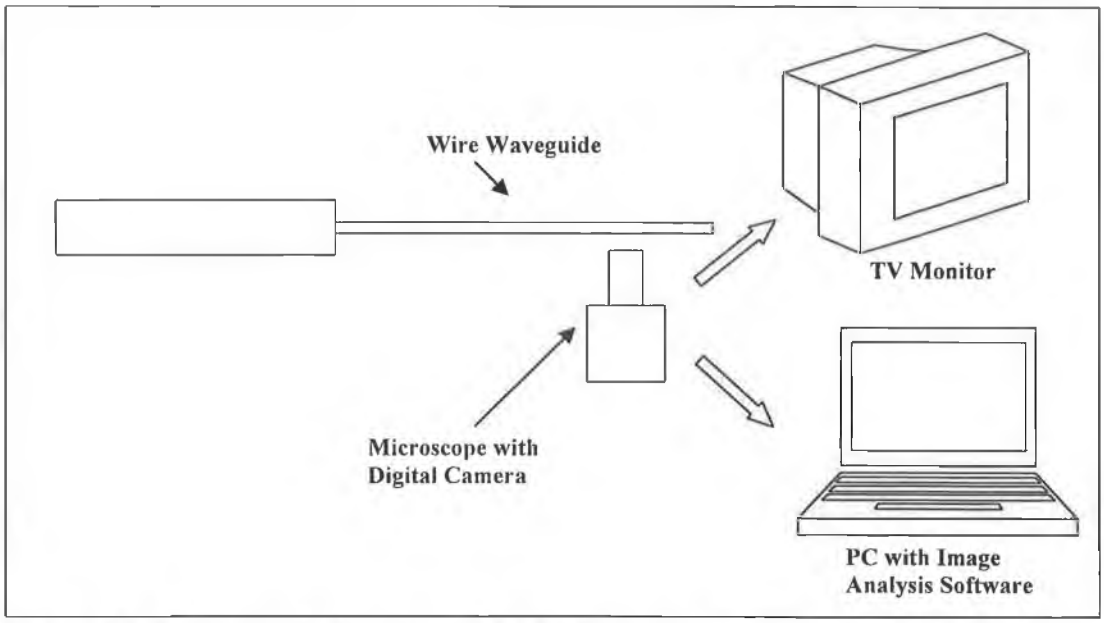

Figure 4.1: Diagram of wire waveguide displacement measurement test rig with optical microscope, camera and PC with image analysis software

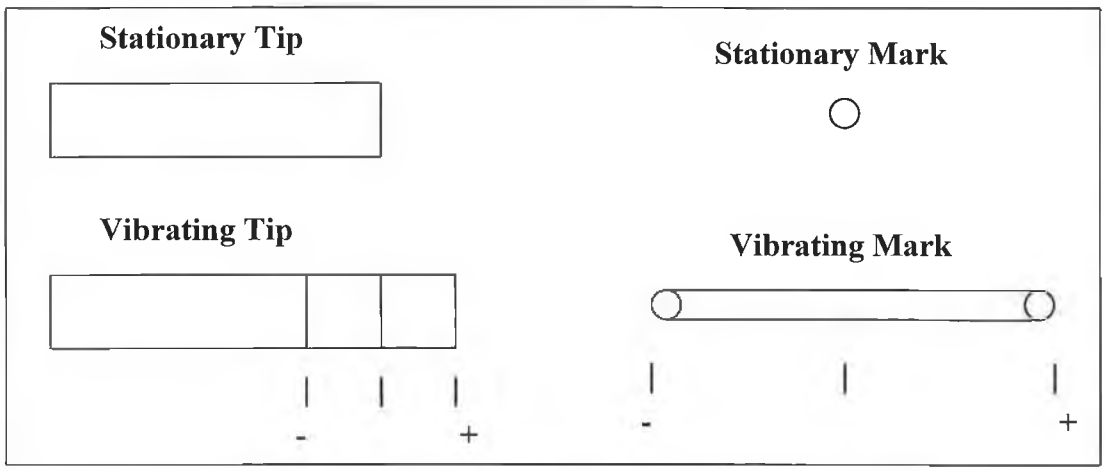

Figure 4.2: Schematic of peak-to-peak displacement measurement by optical means.

While this system has multiple objective lenses with varying magnification factors, the software has to be calibrated for the lenses used, so a picking distance on the image in the software corresponds to the actual distance viewed.

4.2.2. Calibration of Objective Lenses

Calibration was performed using a scale bar (Klarmann Rulings Inc© 'Stage Micrometer') with measurements in micrometers defined. With the objective lens in the microscope, the software is set in calibration mode with an image of the scale bar displayed on the PC. Two points of known distance on the scale bar are selected and the distance entered into the software. This distance is now defined. For improved accuracy, the distance between the two points chosen is kept as large as possible to minimise the effect of operator error. Figure 4.4 shows the image of the scale bar with an objective lens magnification factor of 40.

Because the peak-to-peak displacement measurements were made manually by the user, the accuracy and repeatability of these measurements were determined by assessing the variability in multiple displacement selections. With the scale bar in place and using an objective lens magnification factor of 40, three displacements of 20, 60 and 100 μm were subjected to 25 measurements each.

Figure 4.5 shows a histogram of the range of values obtained for the 20μm scale measurement. These results show that the mean of values chosen for the 20μm measurement was 19.98μm while the standard deviation (σ) was 0.18μm. Similarly, the mean results for the 60μm was 59.82 (σ: 0.23μm) and 100μm was 99.84μm (σ: 0.22μm). Even if the largest spread of data (σ: 0.23μm) for the 60μm measurement is considered 99.7% of measurements (3σ) were within ± 0.69μm.

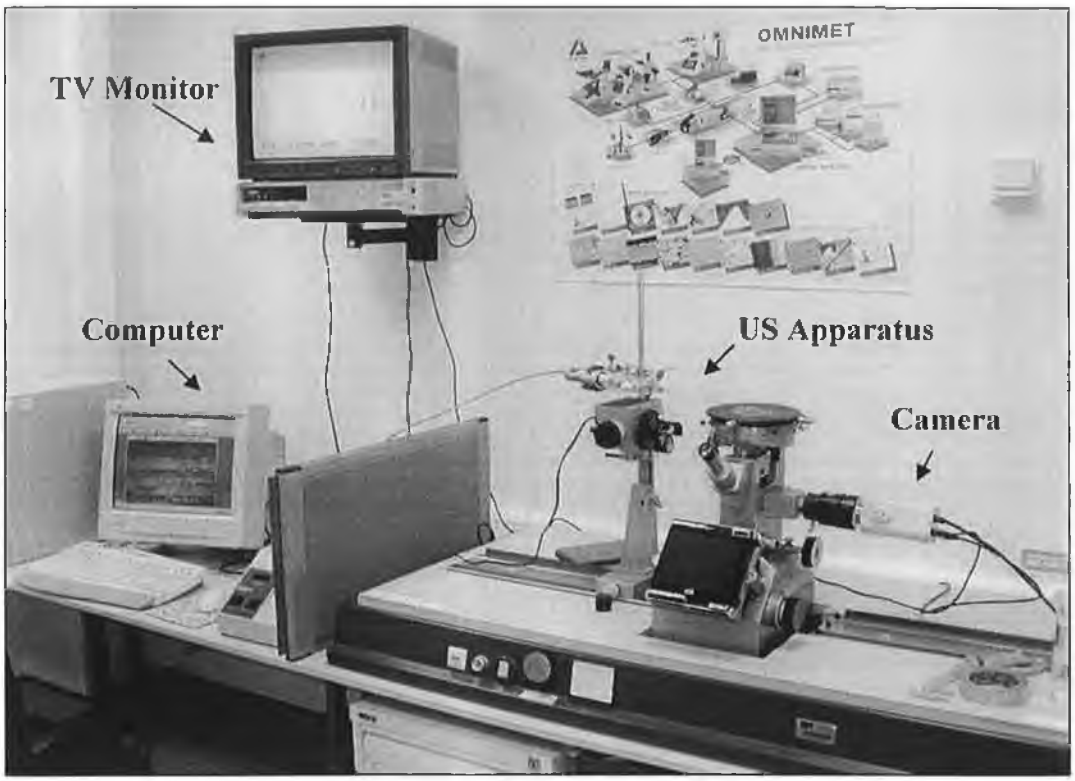

Figure 4.3: Image of wire waveguide displacement measurement system with optical microscope, camera and PC with image analysis software.

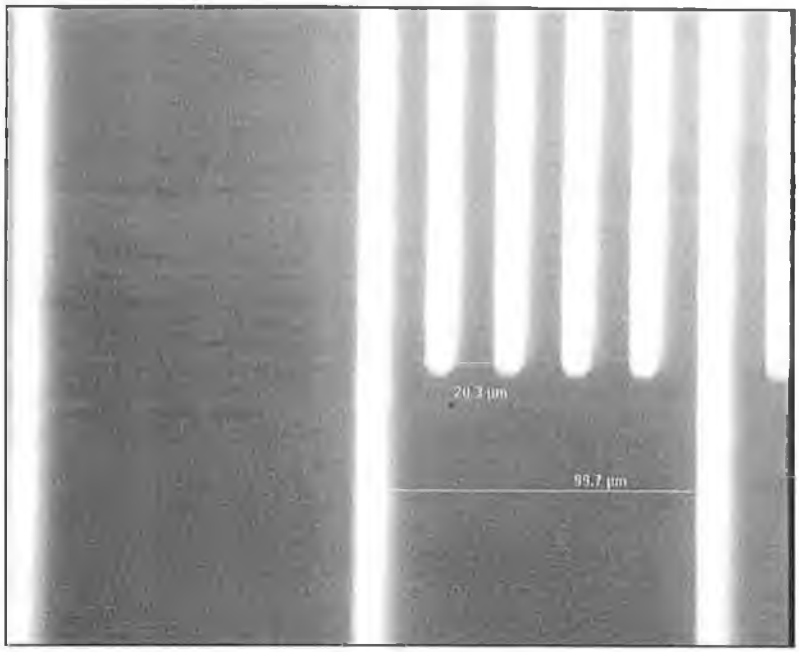

Figure 4.4: Image of scale bar with superimposed displacement measurement for 20 and 100 micrometer divisions.

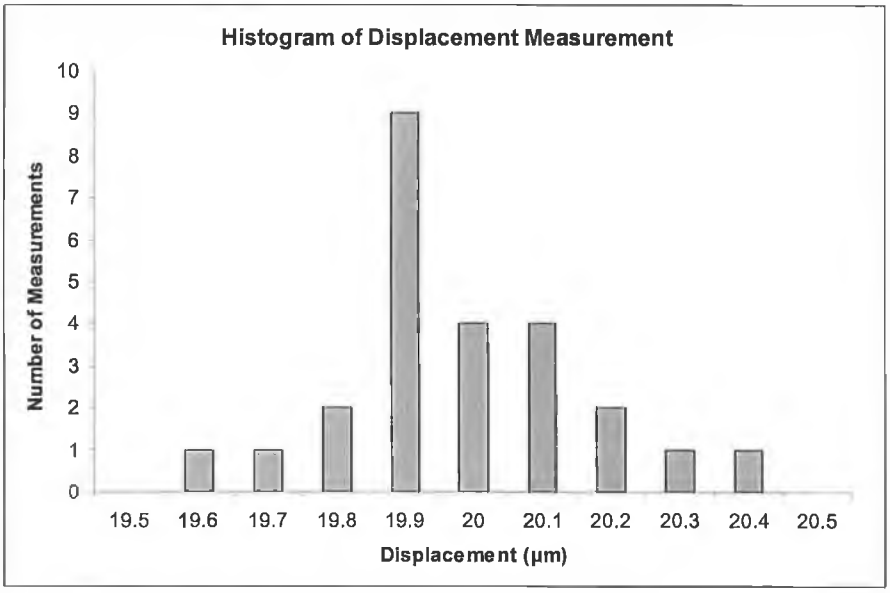

Figure 4.5: Histogram of the spread of measurements recorded for 20µm displacement on scale bar (mean: 19.98µm, σ: 0.18µm).

4.3. Wire Waveguide Distal-Tip Peak-to-Peak Displacements

Using an objective lens magnification factor of 40, the wire waveguide apparatus was orientated and held to allow the wire waveguide distal-tip to be positioned over the microscope lens as shown in Figure 4.6.

The wire waveguide was ensheathed in a catheter in order to minimise transverse vibrations and ensure that the waveguide was parallel with the lens. Figure 4.7 shows an image of the longitudinally vibrating distal-tip of a 1.0 mm diameter wire waveguide and the superimposed displacement measurement from the image analysis software.

Following this procedure the distal-tip displacements for the 1.0 mm diameter wire waveguide were measured for various input power dial settings. This 1.0mm diameter wire waveguide was chosen to allow multiple measurements to be made for each waveguide. The 0.6 mm and 0.35 mm diameter waveguides failed in too short a time period, as shown in Figure 3.24, to allow for multiple tests to be conducted on the same wire.

4.3.1. Effect of input power dial settings

The wire waveguide distal tip results for multiple lengths of 1.0 mm diameter wire waveguide and different input power dial settings are shown in Figure 4.8. These results show that increasing the power delivered from the generator to the converter and acoustic horn increases the wire waveguide distal-tip displacements for any given length. Some lengths resulted in poor or no transmission to the distal tip.

Of particular interest is that at a length of 258mm the distal-tip displacement is greatly increased and at an input power dial-setting level of 2.5 the distal-tip displacement at this length of the wire waveguide was 85μm peak-to-peak. This result seems to indicate that resonance of the waveguide is occurring at certain lengths, as expected.

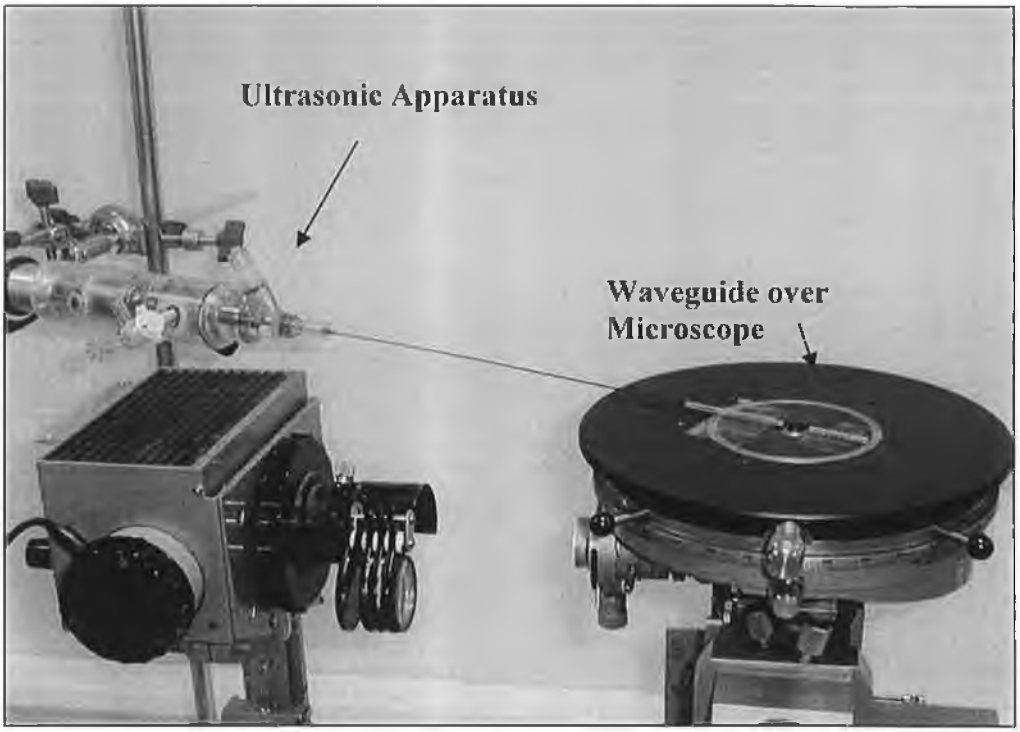

Figure 4.6: Image of ultrasonic wire waveguide apparatus over microscope lens

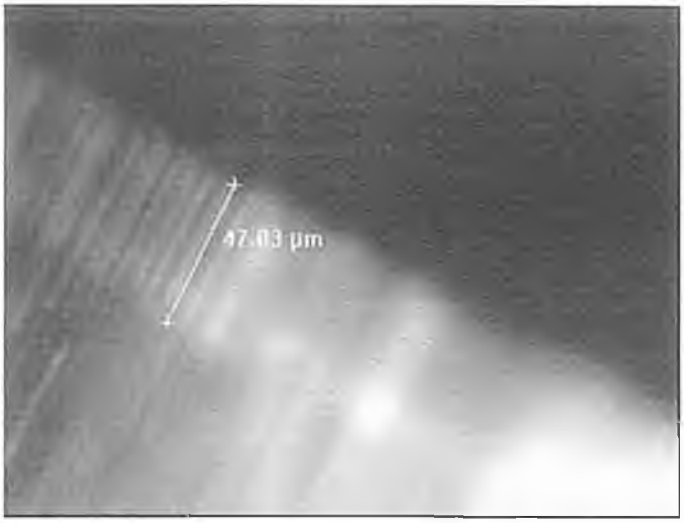

Figure 4.7: Image of vibrating wire waveguide distal-tip obtained by the optical microscope and image analysis software.

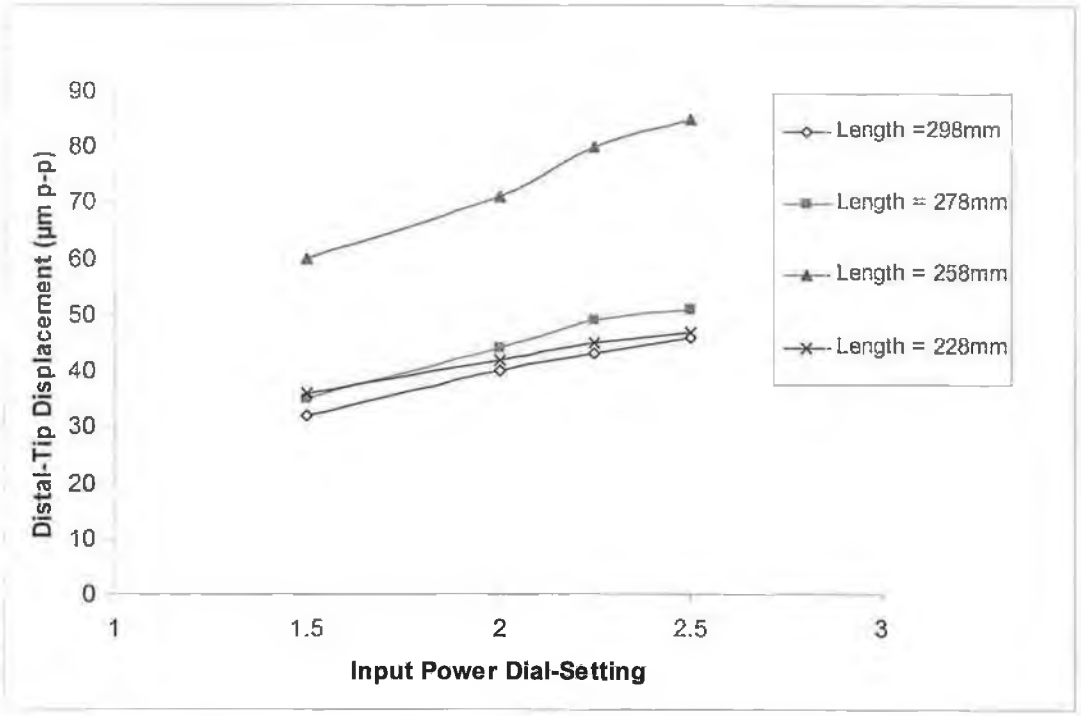

Figure 4.8: Distal-tip displacements for a 1.0mm diameter wire waveguide for generator input power dial settings of 1.5, 2, 2.25 and 2.5

4.3.2. Effects of Wire Waveguide Length

In order to further explore the effect of waveguide lengths, distal–tip displacements for multiple wire waveguide lengths between 118 mm and 303 mm at intervals of 5 mm were tested for a 1.0 mm diameter wire waveguide. The results from this series of experiments for an input power dial-setting of 1.5 are shown in Figure 4.9.

The results show that resonance and non resonance occurs at certain lengths of wire waveguide. The output displacement value near a non-resonant length of 283 mm was 34 μm while at a length of 263 mm the wire waveguide distal-tip displacement is 52 μm for the same input power dial-setting.

As the wire waveguide lengths approached those where resonance occurred (258 mm and 188 mm) the performance of the device started to decline with irregular displacement readings and eventually no distal-tip displacement. Excellent transmission performance was observed at non-resonant lengths (288 mm and 218 mm).

The experimental wire waveguide distal-tip displacement results in Figure 4.9 can be used to determine the frequency at which the waveguide is operating. Both the lengths at which non-resonance occurs and the material properties of the waveguide are known and can be compared with the analytical solution for the non-resonant lengths of a rod to determine frequency of operation.

Using the solution for the non-resonant lengths (l), given in Equation 4.1 the analytically determined lengths compare favourably with the experimental results for an input frequency of 23.5 kHz as shown in Table 4.1:

$$f = \frac{nc}{4l_n} \qquad n = 0, 2, 4, 6... \qquad (4.1)$$

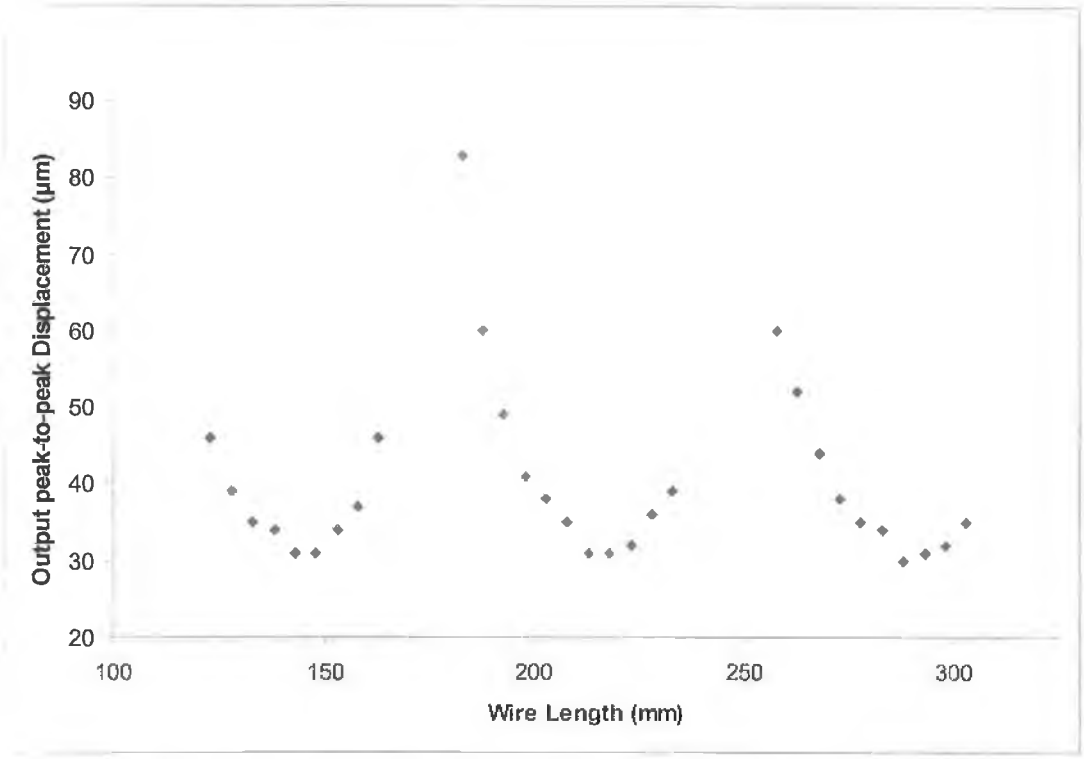

Figure 4.9: Wire waveguide distal-tip displacements for multiple wire waveguide lengths from 118-303 mm for input power dial-setting of 1.5.

Table 4.1: Comparison of experimental and analytical lengths for non-resonance for an input frequency of 23.5 kHz.

n	Analytical Lengths (mm)	Experimental Lengths (mm)	Percentage Error (%)
0	0	-	-
2	72.4	-	-
4	144.8	146	.8
6	217.2	218	0.36
8	289.6	288	0.55

These results are based on the assumption that changing the length of waveguide in the range tested did not cause a significant change in the frequency of operation of the apparatus. This is supported by the relative uniform spacing of the non-resonant lengths of 72 mm and 70 mm. This operational frequency of 23.5 kHz will be used in the numerical modelling of the waveguide.

Having established confidence in the frequency of operation of the ultrasound wire waveguide apparatus it was crucial to determine what the input displacement to the wire waveguide was for each input power dial setting.

In order to determine a reasonable estimate for the input displacement the acoustic horn applies to the proximal end of the wire waveguide for a particular input power dial setting the values of wire waveguide distal-tip displacement at non-resonance were observed.

The solution of the steady state vibration of an undamped rod given in Equation 2.1 shows that at non-resonance the output distal amplitude is equal to the input amplitude. In reality, damping affects the non resonant displacements with a decline in amplitude for increased resonant length number. Using the non-resonant peak-to-peak wire waveguide distal displacements it is possible to extrapolate the input displacement by observing this trend.

Figure 4.10 shows the wire waveguide results with the peak-to-peak distal-tip displacements and a fitted linear trend line through the non-resonant values. Both a linear trend line and an exponential trend line were fitted to the non-resonant data points and were extrapolated back to a zero waveguide length. The results show that for an input power setting of 1.5 the input displacement to the proximal end ($x=0$) of the waveguide is approximately 32μm peak-to-peak. A negligible variation between where the exponential and linear trend lines intercepted the y-axis was determined and the results are shown in Table 4.2.

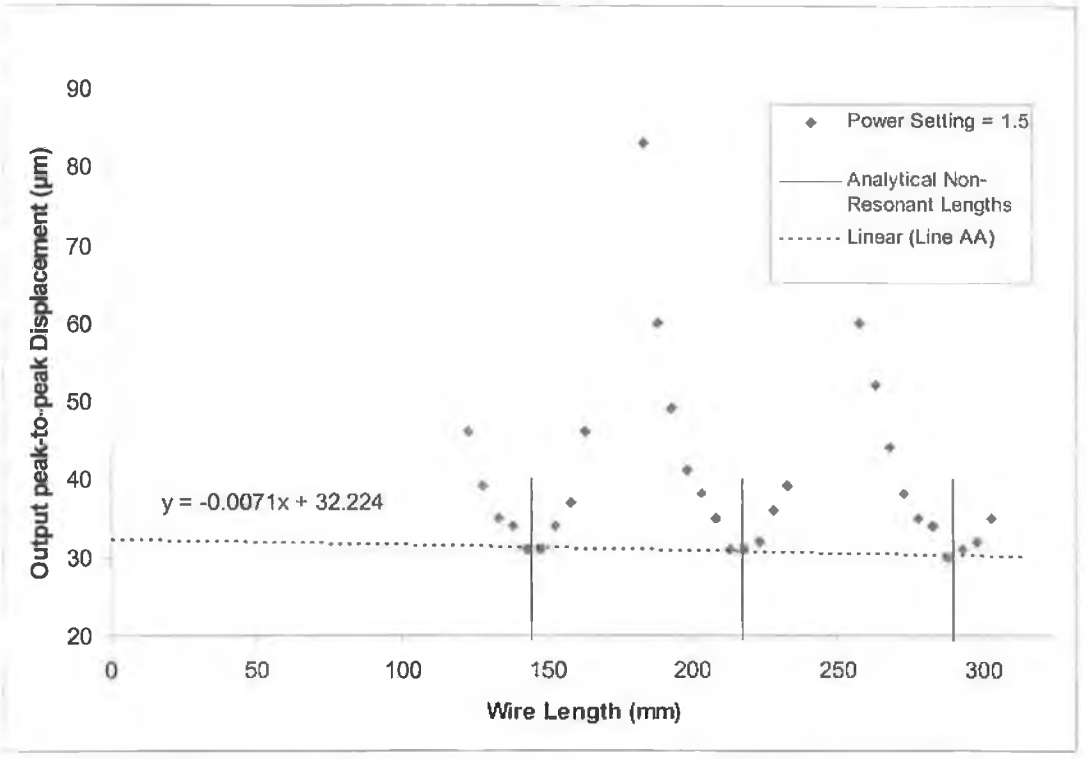

Figure 4.10: Wire waveguide distal-tip displacements for multiple wire waveguide lengths from 118-303mm with extrapolated input displacement trend line and analytical determined lengths.

This technique is only an approximation of the input displacements and is highly sensitive to changes in any of the three non-resonant data points. More non-resonant data would ideally be required or measurement of input displacement at the proximal end of the waveguide. However, this is not possible as once again observations cannot be obtained in this region. These extrapolated input displacements will be further examined when they are used in the numerical model of the waveguide.

This procedure of determining the achievable wire waveguide distal-tip displacements was continued for three other input power settings of 2, 2.25 and 2.5 for a 1.0 mm diameter wire waveguide and the results are shown in Figure 4.11. Both linear and exponential trend lines were fitted to this data also, to determine an estimate of input displacements as shown in Table 4.2.

The results for the four input power settings of 1.5, 2, 2.25 and 2.5 show the overall achievable wire waveguide distal-tip peak-to-peak displacements for a 1.0 mm diameter waveguide. Measurements at resonance could not be made as the apparatus failed to transmit ultrasonic distal-tip displacements at these lengths.

Input proximal displacements for each of the power settings of 2, 2.25 and 2.5 have been estimated to be approximately 41μm, 44.5μm and 46μm, respectively, and will be further examined in the development of a numerical model of the waveguide.

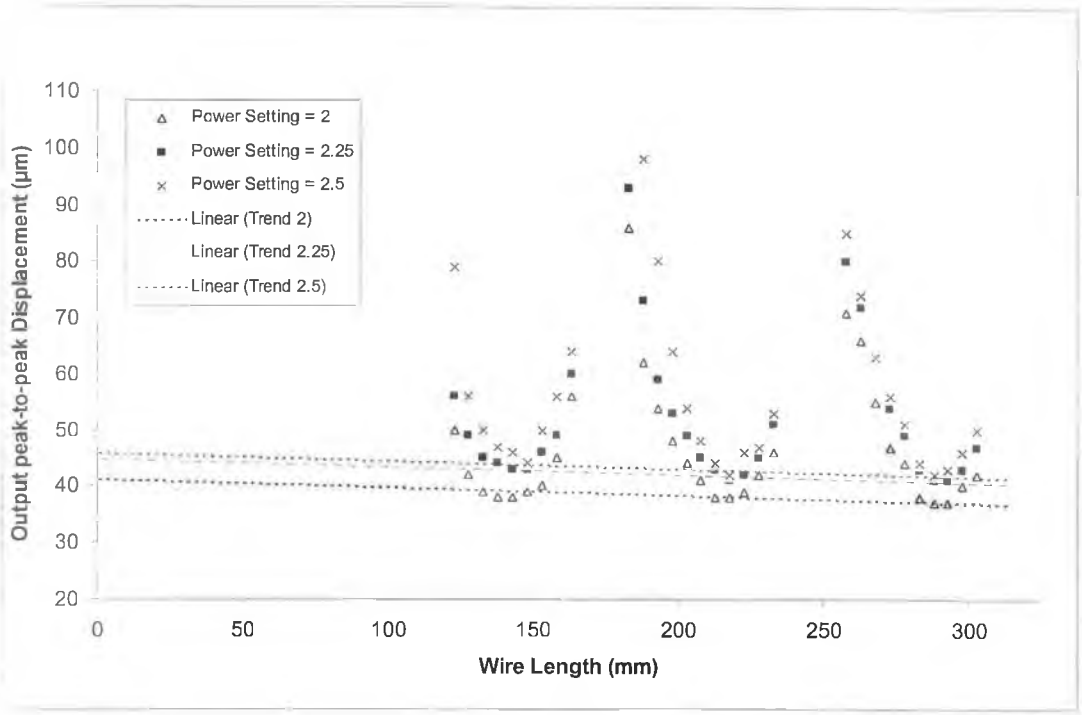

Figure 4.11: Wire waveguide distal-tip displacements for multiple wire waveguide lengths from 118-303mm and input power dial-settings with extrapolated input displacement trend line and analytical determined lengths.

Table 4.2: Comparison of linear and exponential fit trend lines in determining input displacement to wire waveguide

Power Setting	Linear Fit y-Intercept	R-Squared of Linear Fit	Exponential Fit y-Intercept	R-Squared of Exponential Fit
1.5	32.224	0.75	32.269	0.75
2	41.114	1	41.237	0.99
2.25	44.781	0.75	44.863	0.75
2.5	45.781	0.75	45.861	0.75

4.4. Displacement results along length of wire waveguide

Using the solution for the steady-state vibration of an undamped rod given in Equation 4.2 the relative analytical displacement amplitudes at any point in the waveguide (x) between the input at the proximal end ($x = 0$) and the output at the distal end ($x = l$) can be determined for the undamped situation.

$$u(x,t) = b(\cos\frac{\omega x}{c} + \tan\frac{\omega l}{c}\sin\frac{\omega x}{c})\sin\omega t \qquad (4.2)$$

This analytical result could be expected to most clearly match the experimental displacements for a waveguide near a non-resonant length of 288 mm, for example, where the effects of damping are at a minimum. For an input frequency of 23.5 kHz and input peak-to-peak displacement of 32 μm to the proximal end the analytical internal wave structure is shown in Figure 4.12.

The analytical solution results for a 288 mm wire waveguide show a standing wave structure with a series of displacement nodes at lengths of 33, 106, 178 and 251mm and displacement anti-nodes at lengths of 70, 143, 215 and 288 mm. For the non-resonant lengths of waveguide we see that the output displacement equals that of the input and both are on displacement anti-nodes.

Experimental internal displacement measurements were made for three wire waveguide lengths of 288 mm, 303 mm, and 273 mm representing a non-resonant length and lengths either side close to resonance. An example of the type of image obtained for an internal measurement is shown in Figure 4.13. All internal displacement measurements were made for an input power dial setting of 1.5 corresponding to 32 μm input displacement to the proximal end of the waveguide.

The results for the 288 mm wire waveguide are shown in Fig 4.14 and indicate a standing wave structure similar to that determined from the analytical solution. The experimental results, however, show that near displacement node locations as predicted by the analytical solution, the displacement values were non-

zero and increased in magnitude at nodal locations nearer the proximal end of the waveguide.

These results indicate that there is a standing wave with a series of displacement maxima (288, 213 and 148 mm) and minima (253 mm and 178 mm). This is further shown in the internal displacements measurements along with both a 273 mm and a 303 mm length wire waveguide as shown in Figure 4.15.

Due to the fact that the wire waveguide lengths of 273mm and 303 mm are displaced from the non-resonant length of 288 mm and therefore closer to resonant lengths the overall peak-to-peak displacements measured were larger in value.

Of particular interest is that, due to the standing wave structure developed and frequency of operation, at the distal section of the wire waveguides exists a displacement minimum that increases to a displacement maximum over the last 35 mm of the waveguide. The abrasive and frictional effects of the motion of the outer surface of the wire may allow for the wire waveguide to be used in direct side ablation as opposed to direct axial ablation.

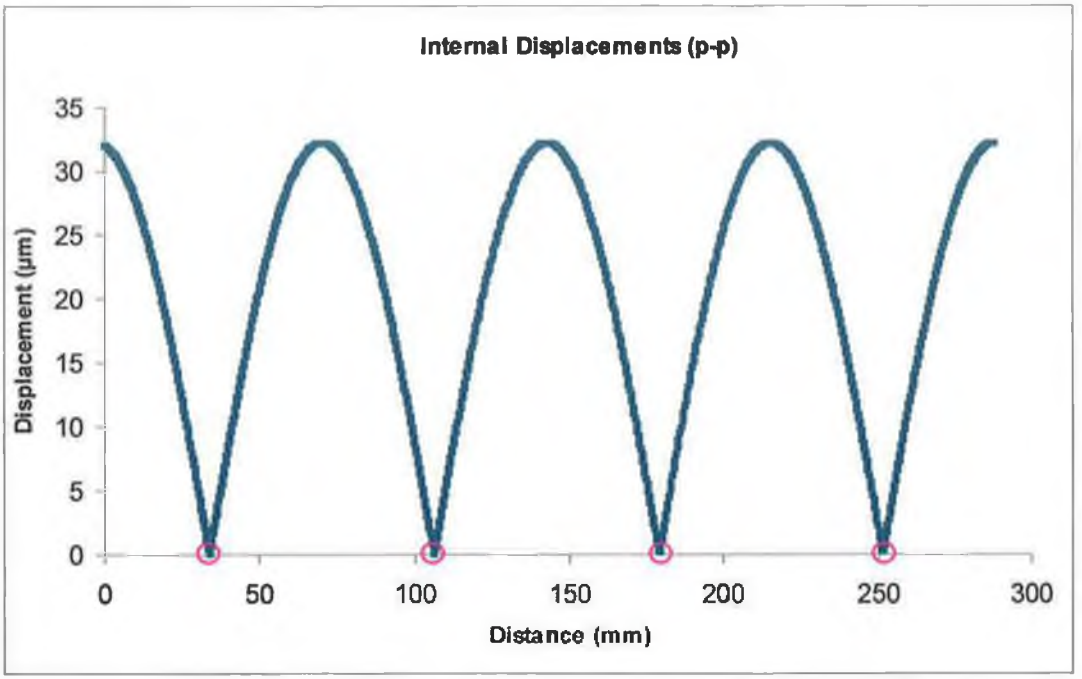

Figure 4.12: Analytical solution of internal displacements in an undamped thin rod of length 288mm subjected to an input displacement of 32µm at 23.5 kHz. Nodal displacement locations highlighted by circles (pink).

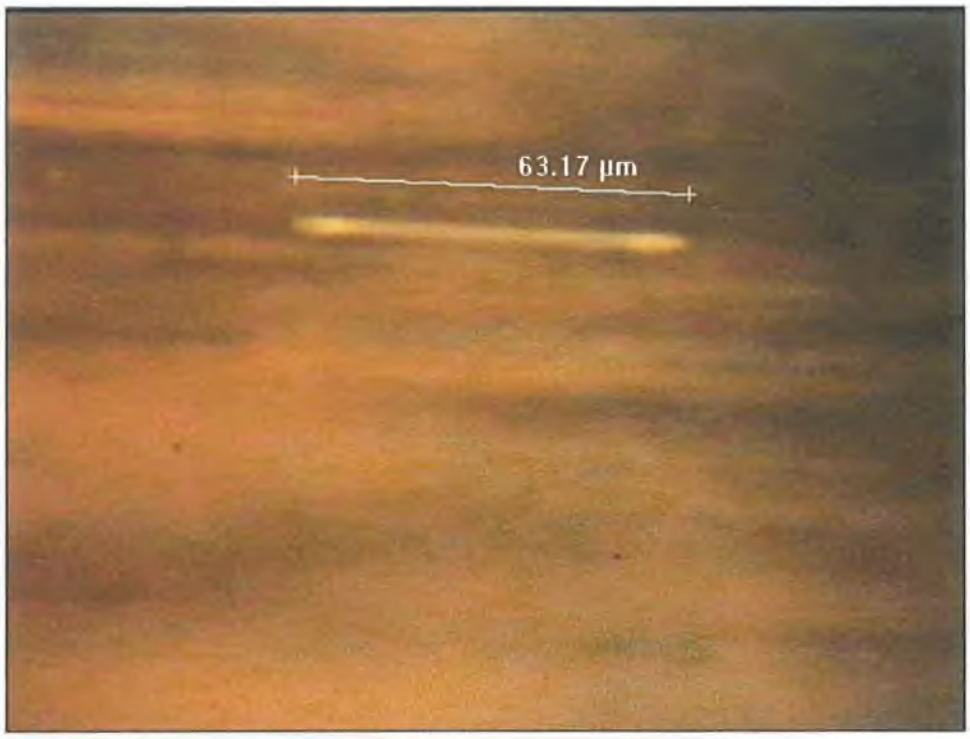

Figure 4.13: Image of internal wire waveguide displacement obtained by the optical microscope and image analysis software. Initial length of mark was 9.2µm and the image streak length of 63.17µm giving a displacement of approximately 54µm

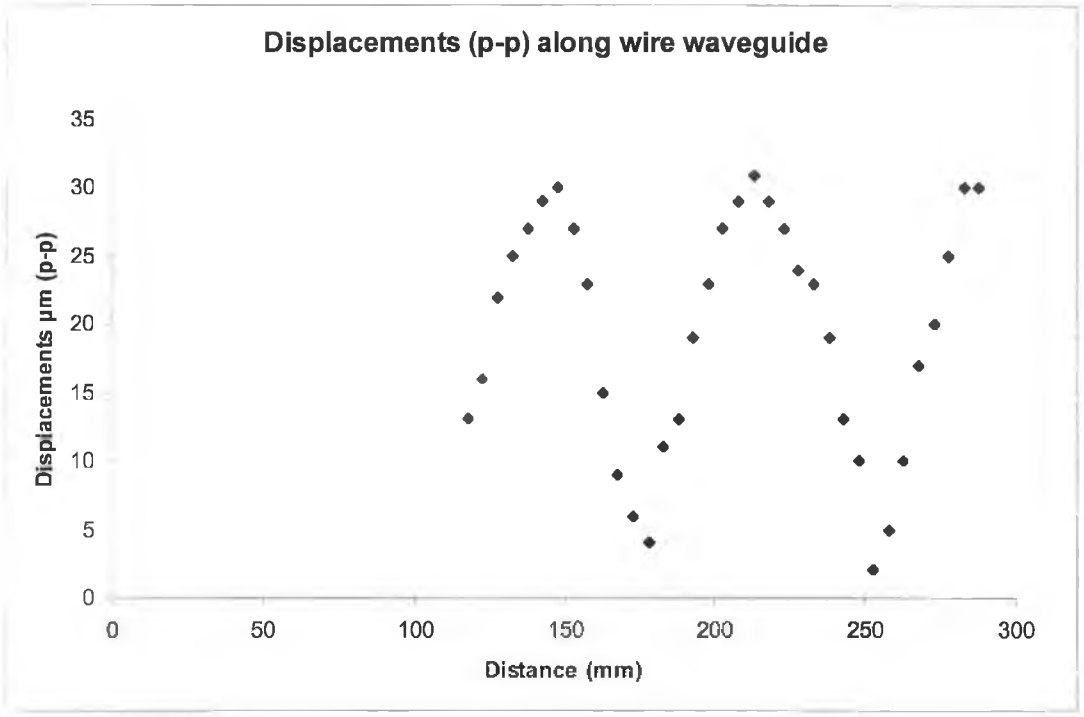

Figure 4.14: Experimental results of wire waveguide displacement along a wire waveguide of non-resonant length 288mm and an input power setting of 1.5 (input displacement = 32µm)

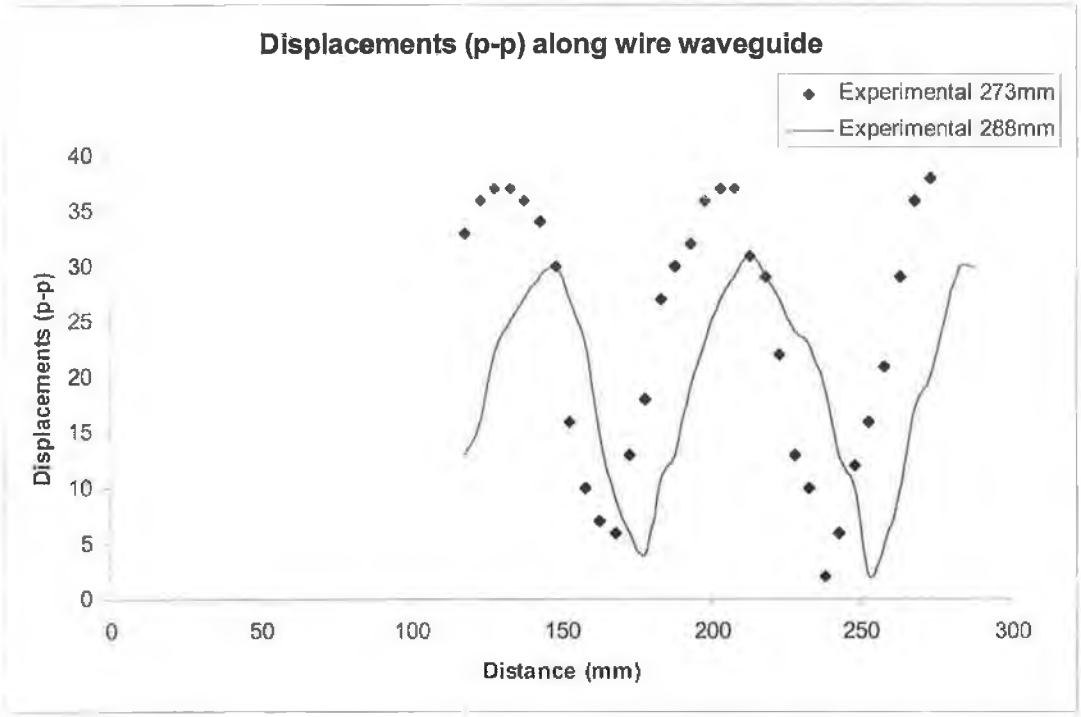

Figure 4.15a: Experimental results of wire waveguide displacement along a wire waveguides of length 273 mm and an input power setting of 1.5 (input displacement = 32μm)

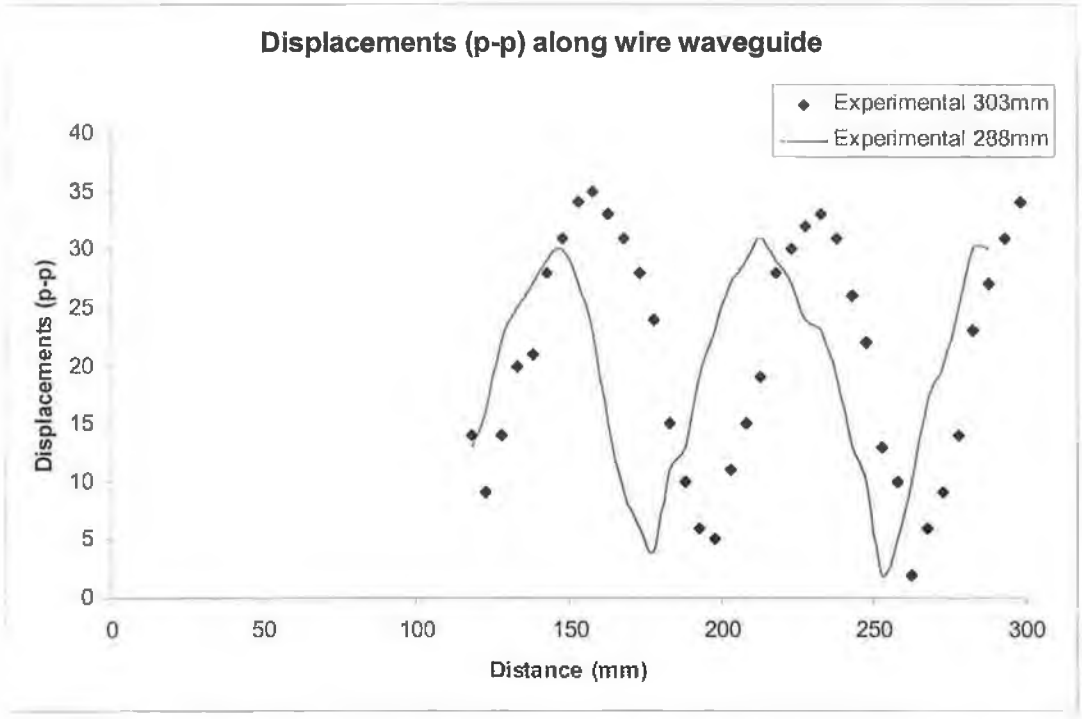

Figure 4.15b: Experimental results of wire waveguide displacement along a wire waveguides of length 303 mm and an input power setting of 1.5 (input displacement = 32μm)

4.5. Summary

Wire waveguide distal-tip displacements were experimentally determined by direct optical measurement and this showed the effects of resonant lengths and input power dial-setting on the measured displacements.

Wire lengths close to resonant lengths showed increased wire waveguide distal-tip displacement, but the overall performance of the wire waveguide apparatus very close to these resonant lengths was difficult to measure based on the unsteady displacement readings observed and the inability of the generator to drive the wire at resonance. However, near or at non-resonant lengths the ultrasonic wire waveguide apparatus delivered steady distal-tip displacements that could be measured.

Peak-to-peak displacement measurements along the length of the waveguide showed a standing wave structure similar to that predicted by the analytical solution presented with a series of displacement minima and maxima along the length of the waveguide and some losses due to damping were observed.

The frequency of operation of the ultrasonic wire waveguide apparatus was estimated to be 23.5 kHz by comparing the experimentally observed non-resonant lengths with the analytically determined non-resonant lengths. For the range of input power settings tested the input peak-to-peak displacements applied by the distal-tip of the acoustic horn to the proximal end of the wire waveguide have been determined. Both of these results will be further examined in the development of a numerical model to predict wire waveguide behaviour.

Chapter 5

Numerical Model of Wire Waveguide and Fluid Interaction

5.1 Introduction

The experimental behaviour of the wire waveguide observed in Chapter 4 highlights the complexity of the behaviour of the ultrasound wire waveguide. In the ultrasound angioplasty application, it is vital that the conditions at the distal-tip are well understood and that a product can be designed to behave predictably *in vivo*.

The inputted ultrasonic displacements to the proximal end of the wire waveguide have been experimentally shown to cause a standing wave structure in small diameter wire waveguides and a peak-to-peak displacement at the distal-tip. Other authors have shown that the distal-tip vibration at ultrasonic frequencies results in a pressure field being developed in the fluid around the distal-tip and that at sufficiently high amplitudes of vibration cavitation can occur.

While an analytical solution of the steady-state wire waveguide behaviour exists, as shown in Chapter 2, this only applies to an undamped uniform rod with no interaction with fluid at the distal-tip. In reality, the wire waveguides reported in clinical trials are non-uniform having an enlarged distal-tip geometry that increases the contact area with the atherosclerotic plaque and also increases the pressures in the surrounding fluid field; therefore, enhancing the important disruptive cavitation mechanism. The NiTi wire waveguide material also dampens these vibrations.

A finite element model of the wire waveguide and fluid surrounding the distal-tip is described here as part of this work. This fluid structure finite element model is used to predict the behaviour of the wire waveguide under realistic loading conditions with the inclusion of damping, distal-tip geometries and fluid.

Further, the model will predict the pressures in the surrounding fluid due the vibrating wire waveguide distal-tip and predict the conditions necessary to cause cavitation. This model will predict pressures developed for various non-uniform distal-tip geometries in addition to the simplified spherical geometry for which analytical solutions appear in the literature, as shown in Chapter 2.

In order to achieve these goals and validate the models against both the experimental work and analytical solutions available, the modelling was broken down into two distinct sections.

Firstly, a harmonic structural finite element model to simulate the behaviour of the wire waveguide is developed. The input conditions to this model are the input peak-to-peak displacements and the frequency of operation determined from the experimental testing in Chapter 4. The model predicts the lengths of wire waveguide where resonance occurs and also the distal-tip displacement characteristics. These are compared with both the analytical steady-state solution and the experimentally determined response of the wire to changes in length.

In addition, this model will determine the internal standing wave structure, including displacements and stresses, in the waveguide and will predict the locations of displacement, and stress, minima and maxima over a range of conditions. Once validated the model has the potential to be extended to more complex wire designs and distal-tip shapes.

Secondly, a fluid structure interaction finite element model is developed. This model is used to predict the effects of the presence of the fluid at the distal-tip on the wire waveguide and the pressures in the fluid field surrounding the distal-tip. These results are compared with experimental results of the pressures in the field around an experimental apparatus published by Makin and Everbach [62].

Initially, a modal analysis is performed to address the issues raised in the literature survey in the modelling of structures at ultrasonic frequencies. Some of these effects will be analysed further in the harmonic analysis section.

5.2 Modal Analysis of Wire Waveguide

A modal analysis of the waveguide is an good starting point in the simulation and prediction of wire waveguide behaviour as it is less computationally expensive than a full harmonic analysis and can be used to investigate the effects of mesh density and also to perform sensitivity studies.

5.2.1 Modal Analysis Method

The problem sketch for the modal analysis of the waveguide is shown in Figure 5.1. The wire waveguide was modelled using ANSYS© Multi-physics (v8.1) as a uniform rod subjected to a fixed-free boundary condition and solved using the Block Lanczos eigenvalue solver [76]. The basic equation solved in an undamped modal analysis is:

$$[K]\{\phi_i\} = \omega_i^2[M]\{\phi_i\} \tag{5.1}$$

where $[K]$ = stiffness matrix

$\{\phi_i\}$ = mode shape vector (eigenvector) of mode i

ω_i = natural frequency of mode i (ω_i^2 is the eigenvalue)

$[M]$ = mass matrix

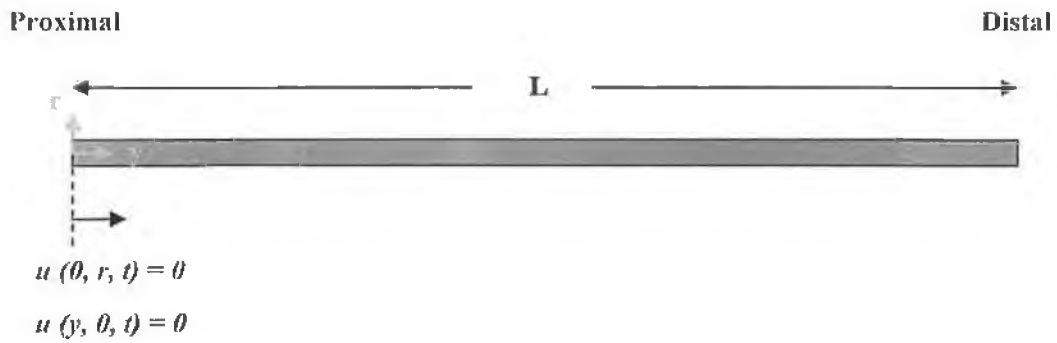

Figure 5.1: Problem sketch of wire waveguide with fixed-free boundary conditions

5.2.2 Effects of Mesh Density on Modal Analysis of Wire Waveguide

The numerical model of the wire waveguide with boundary conditions is shown in Figure 5.2 and was used to determine the effect mesh density has on the predicted resonant frequencies compared with those from the analytical solution of a fixed free uniform rod. This is an axisymmetric model using 2D axisymmetric 4 node quadrilateral structural elements (Plane42) [77]. The model was constrained to allow zero displacement in the radial direction along the axial centreline and is also constrained with a zero displacement in the axial direction at the proximal end nodes.

Mesh density (pattern) is defined as the number of elements in the radial direction (r) multiplied by the number of elements in the axial direction (y) and is presented as (r × y) [66]. Insufficient element numbers in the axial direction will result in the internal mode shape being poorly resolved while the number of elements used in radial direction is to ensure good element aspect ratios.

Mesh density analysis was performed on modelled wire waveguides of length equal to 303 mm and for three waveguide diameters of 1.0 mm, 0.6 mm and 0.35 mm, chosen as this is similar to the experimentally tested waveguides. The material properties, Young's modulus and density, used for the models of the NiTi wire waveguides are those given in Chapter 4.

5.2.3 Sensitivity Analysis of Material Properties

Following the mesh density analysis, and the establishment of sufficient meshing pattern criteria, further models were developed with this element structure and pattern to determine the effects of minor changes in material properties of the wire waveguide. This allowed for greater understanding of model sensitivity to changes in properties such as Young's modulus and density.

Values for both the Young's modulus and density were varied by ± 5% of the values given in Chapter 4. This was considered sufficient as similar variation in material property values was evident based on material testing results shown in Chapter 4.

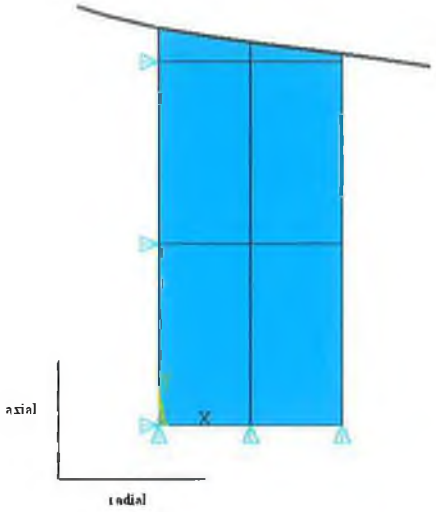

Figure 5.2a: Proximal end of finite element model of 1.0mm diameter wire waveguide with a mesh density of 2 × 606 with aspect ratio of 2

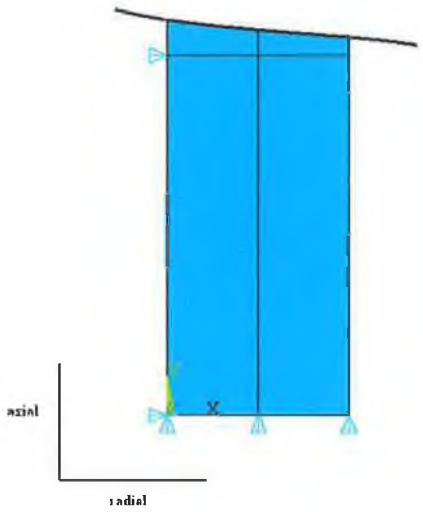

Figure 5.2b: Proximal end of finite element model of 1.0mm diameter wire waveguide with a mesh density of 2 × 303 with the poorer aspect ratio of 4

5.2.4 Results of Modal Analysis

The analytical solution for the resonant frequencies of a 303 mm wire waveguide with the material properties given is shown is shown in Table 5.1 for a frequency range of 0-30 kHz. These results show that over this frequency range there are five resonant frequencies for the waveguide.

Figure 5.3 shows the results of resonant frequencies from the numerical modal analysis models for different mesh density. From these results we see that insufficient mesh density (1×10) can over predict the higher resonant frequencies compared to the analytical solution and can also result in the failure to determine the higher resonant frequencies altogether as seen in the 1× 5 solution.

From the results of the 1.0mm diameter wire waveguide, shown in Figure 5.3a, at mesh densities lower than 1 × 10 the higher resonant frequencies fail to be resolved and no value is returned. Where insufficient mesh density is used the calculated resonant frequencies are higher than the analytical solution but eventually at a mesh density of 1 × 200 all five resonant frequencies are calculated to a high degree of accuracy.

The final value of 2 × 606 was chosen so that there would be multiple elements in the radial direction and with an appropriate aspect ratio. Figure 5.2a shows this element structure which breaks down to 2 elements per a millimetre in the axial direction and 4 elements per a millimetre in the radial direction. This is the mesh density and geometry for the 1.0 mm wire waveguide and will be used in the further harmonic analysis study, in section 5.3.

In a similar manner, Figure 5.3b and Figure 5.3c show the mesh density analysis results for both the 0.6 mm diameter and the 0.35 mm diameter waveguides, respectively.

Table 5.1: Comparison of Analytical and Numerical Resonant Frequencies for waveguides of length 303mm.

Resonant Frequency	**Analytical Resonant Frequency Solution (Hz)**	**Numerical Resonant Frequency Predictions (Hz)** (% Error)		
		1.0mm	**0.6mm**	**0.35mm**
1	2812.7	2813.5 (0.03%)	2813.5 (0.03%)	2813.5 (0.03%)
2	8438.11	8440.53 (0.03%)	8440.53 (0.03%)	8440.52 (0.03%)
3	14063.53	14067.6 (0.03%)	14067.57 (0.03%)	14067.56 (0.03%)
4	19688.94	19694.74 (0.03%)	19694.65 (0.03%)	19694.62 (0.03%)
5	25314.35	25321.96 (0.03%)	25321.77 (0.03%)	25321.71 (0.03%)

Following this analysis, and maintaining good element aspect ratio, a mesh density value of 2 × 909 was chosen for the 0.6 mm waveguide. This corresponds to 3 elements per a millimetre in the axial direction and 4 elements per a millimetre in the radial direction. Similarly for the 0.35 mm diameter wire waveguide model a mesh density value of 2 × 1212 was chosen, corresponding to 4 elements per a millimetre in the axial direction and 4 elements per a millimetre in the radial direction.

5.2.5 Summary of Modal Analysis

Table 5.1 shows a comparison of the results for the resonant frequencies of the wire waveguides, for all three diameters, and their respective final chosen mesh density against the steady-state analytical solution for a fixed-free uniform rod. The resonant frequencies calculated from the numerical model are independent of diameter, as expected from the analytical solution, and compare favourably with the analytical results with a percentage error of 0.03%.

The mesh densities established for the various diameter waveguides give confidence that the higher resonant frequencies will be captured prior to moving on to the more computationally expensive harmonic and fluid-structure analysis. These mesh densities were also used in the parametric study.

Figure 5.4 shows the effects of changes in Young's modulus and material density by ± 5% on the first and fifth resonant frequencies. These results in conjunction with the mesh density analysis suggest that with confidence in material properties and suitable mesh density accurate results of the frequency response of the wire waveguide can be obtained by the numerical method. These results form the basis of the harmonic response analysis of the wire waveguide.

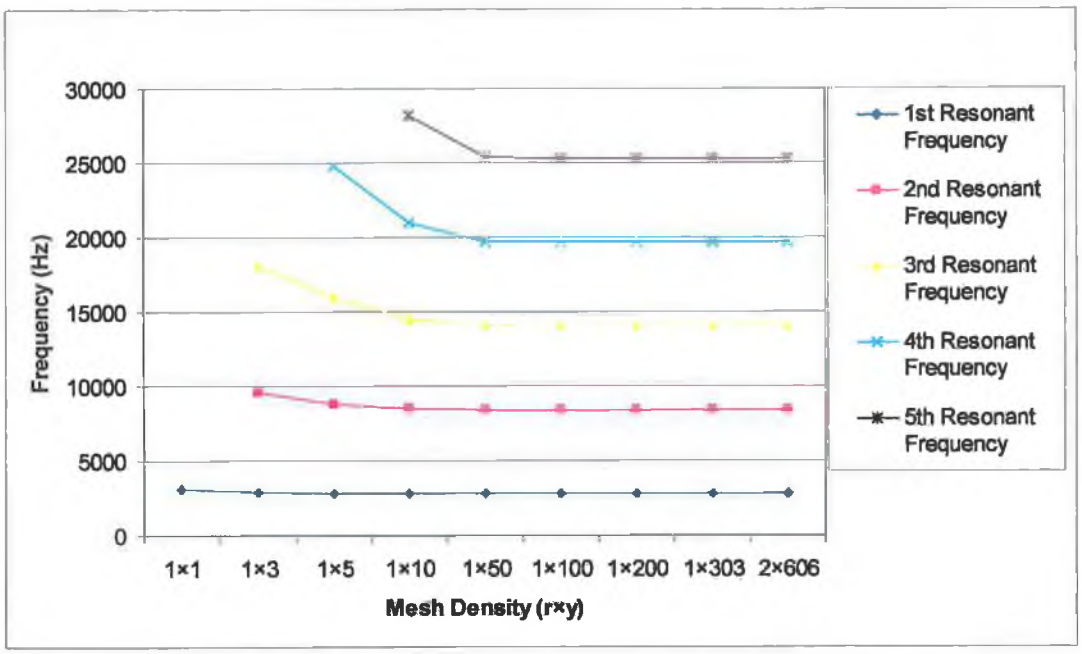

Figure 5.3a: Mesh density results from modal analysis of 1.0 mm diameter wire waveguide model of length 303mm

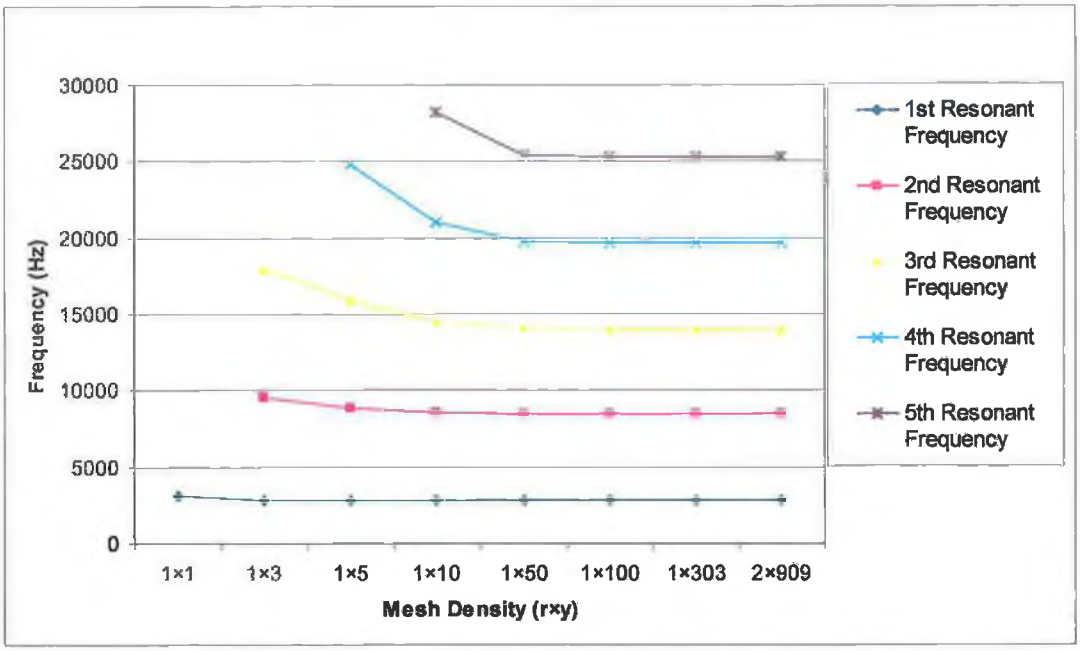

Figure 5.3b: Mesh density results from modal analysis of 0.6 mm diameter wire waveguide model of length 303mm

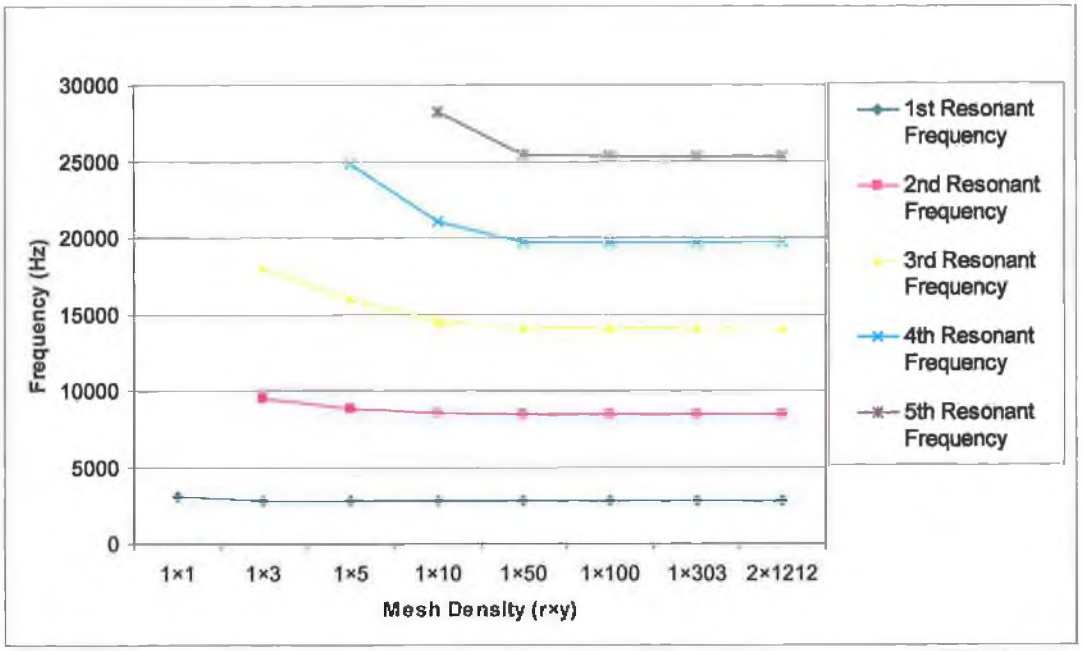

Figure 5.3c: Mesh density results from modal analysis of 0.35 mm diameter wire waveguide model of length 303mm

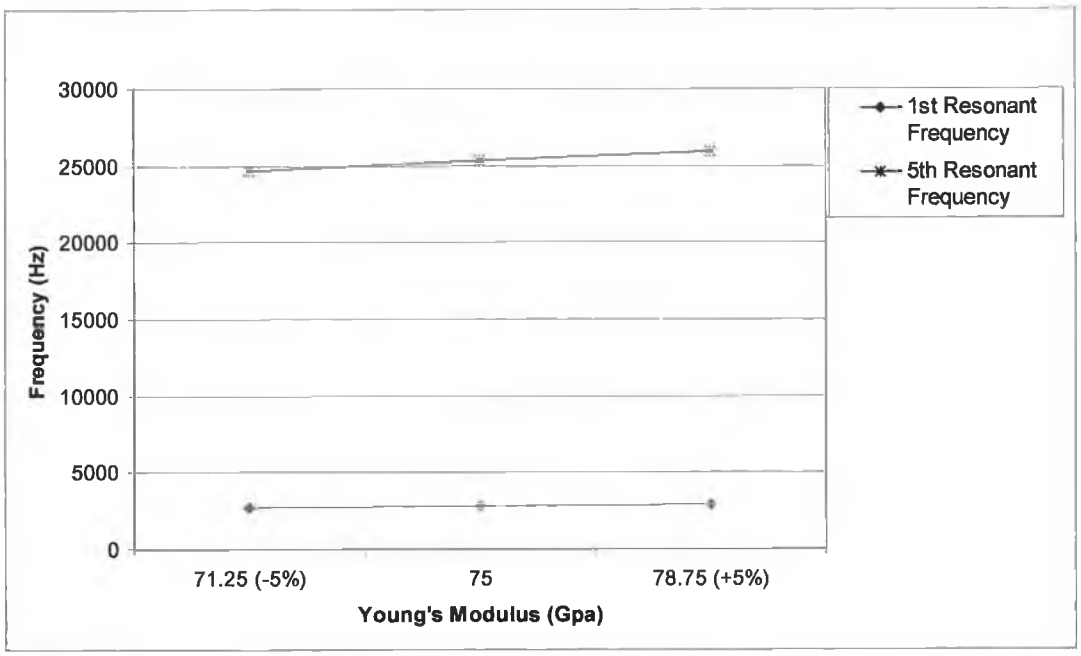

Figure 5.4a: Effect on the first and fifth resonant frequencies due to variations (± 5%) in Young's modulus, length = 303mm.

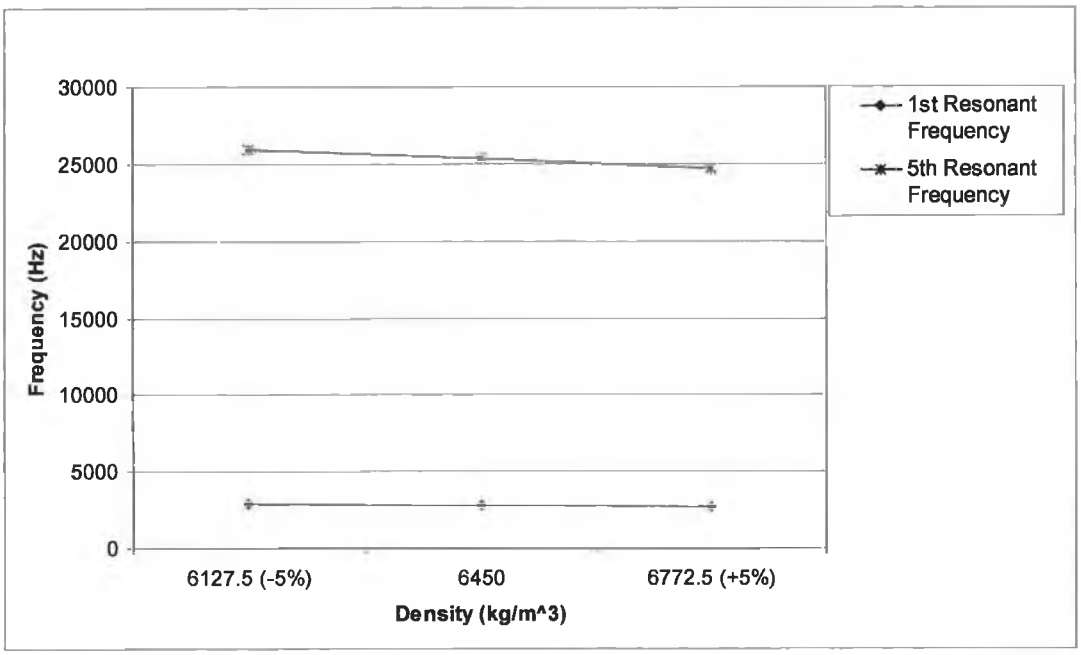

Figure 5.4b: Effect on the first and fifth resonant frequencies due to variations (± 5%) in density, length = 303mm.

5.3 Harmonic Response Analysis of Wire Waveguide

A harmonic response analysis is used to determine the response of a structure under a sustained cyclic load. This analysis is generally performed to gain an understanding of how a structure will respond over a wide range of frequencies due to inputted forces or displacements and allows damping in the system to be modelled. It is a steady-state analysis as initial transient effects are ignored and only the steady state response determined [67].

This technique is used to model the behaviour of the wire waveguide as it undergoes a sustained sinusoidal displacement imposed by the radiating face of the acoustic horn. This analysis can be performed for a fixed length of wire waveguide over a range of frequencies or multiple models can be developed to simulate the effects of wire waveguide length on distal-tip peak-to-peak displacement for a prescribed input frequency and displacement. These simulations will yield results comparable to the experimental analysis performed on various wire lengths in Chapter 4 and the model will be validated against these results.

The harmonic response analysis can also be used to determine the steady-state wave structure and displacements along the length of the waveguide at a particular frequency and can also be compared with the displacements and standing wave determined in the experimental analysis.

5.3.1 Harmonic response method

A harmonic response analysis solves the general equation of motion for a structural system [67] given by:

$$[M](\ddot{\vec{u}}) + [C](\dot{\vec{u}}) + [K](\vec{u}) = (\vec{F}^{a}) \qquad (5.2)$$

where $[M]$ = mass matrix

$[K]$ = stiffness matrix

$(\vec{F}^a)$ = applied load vector

$[C]$ = damping matrix

$(\ddot{\vec{u}})$, $(\dot{\vec{u}})$ and $(\vec{u})$ = the nodal acceleration vector, nodal velocity vector and nodal displacement vector, respectively.

The presence of the damping matrix is necessary to represent material damping and losses in a harmonic response analysis. It can be used to control the response at and near resonant locations and can be used to account for damping due to many phenomena. It is planned to use a constant damping value in this analysis to account for all damping. The damping matrix is determined from:

$$[C] = (\beta)[K] \tag{5.3}$$

where (β) is the variable matrix multiplier determined from the inputted damping value (ζ) over the harmonic frequency range (f):

$$(\beta) = \frac{\zeta}{\pi f} \tag{5.4}$$

The problem sketch for the harmonic response analysis model is shown in Figure 5.5. Axisymmetric solid Plane42 elements, as described, were used and constrained along the central axial line to have zero displacement in the radial direction. The proximal end of the modelled wire waveguide is subjected to an applied harmonic displacement, $u = bsin(\omega(t))$ to simulate the applied displacement

from the acoustic horn. The analysis is performed over a prescribed frequency range.

5.3.2 Distal-tip response of wire waveguides over a range of frequencies

The harmonic response analysis method is initially used to simulate the response of wire waveguides over a set frequency range similar to the modal analysis. This is to ensure that the mesh densities used are suitable to predict the response of the wire waveguide over the 0-30 kHz frequency range of interest. Multiple models are developed for the wire waveguide diameters of 1.0 mm, 0.6 mm and 0.35 mm, with the appropriate mesh densities, established in the modal analysis study, used.

These models are then used to predict the wire waveguide distal-tip displacement frequency response for a wide a range of input conditions, including variable wire length, input displacement and damping values.

5.3.3 Distal-tip response of wire waveguides over a range lengths

To simulate the behaviour of the wire waveguide under realistic operating conditions, models were developed to determine the distal-tip response of the waveguide to a prescribed input signal over a wide range of lengths. This study is directly comparable with the experimental tests of distal-tip displacements for various lengths conducted in Chapter 4.

Multiple models were developed for a range of wire waveguide lengths between 118 mm and 303 mm in intervals of 5mm for waveguide diameters of 1.0, 0.6 and 0.35 mm. Input displacements applied to the proximal end of the model are based on those determined experimentally. Distal-tip displacement results at a frequency of 23.5 kHz, the operational frequency of the experimental apparatus, were predicted for each of the models.

5.3.4 Displacement response along length of wire waveguides

Using the models developed in the previous section, the steady-state wave structure (standing wave) was determined for wire waveguides of various lengths at the prescribed frequency of 23.5 kHz. This was achieved by plotting the predicted displacements along the entire length of the waveguide.

These results were compared to the experimentally observed internal displacements and wave structure discussed in Chapter 4. The locations of displacement maxima and minima along the waveguide were also compared. In addition, the numerical harmonic model is used to predict the internal stresses at various locations along the length of the waveguide.

5.3.5 Wire Waveguides with Spherical Distal-tip Geometry

Having modelled the small diameter wire waveguide response, spherical distal-tip geometries are included and modelled to establish the effect these have on the overall response of the waveguide.

These models with distal-tip geometries are more representative of wire waveguides previously used in clinical investigations with potential use in cardiovascular and peripheral surgery [25, 25]. Wire waveguides with spherical ball-tips of varying diameter are modelled and form the structural basis for the fluid-structure interaction modelling of the waveguides in fluid, which is described later in this Chapter.

5.3.6 Results from harmonic response analysis

Figure 5.6 shows the predicted distal-tip peak-to-peak displacement harmonic response for all three wire waveguide diameters for a frequency range of 0 – 30 kHz and an input axial peak-to-peak displacement of 30 μm. These models are for wire lengths of 303 mm and an arbitrary damping value of 1%.

The resonant frequency results predicted in the harmonic response models confirm the modal analysis results that there is sufficient mesh density to correctly capture and predict all the resonant frequencies in the range of interest with the

overall response being independent of waveguide diameter as dictated by the analytical theory [65].

The effect of changing input displacement on the predicted wire waveguide distal-tip displacements is shown in Figure 5.7 for a model of a 1.0 mm diameter waveguide. Three input peak-to-peak displacements of 30 μm, 60 μm and 90 μm are shown. Once again an arbitrarily chosen damping value of 1% was used.

These results show that the predicted wire waveguide distal-tip displacement output at any frequency increased with increasing input displacements. In the case of the apparatus described in Chapters 3 the operational frequency is constant at 23.5 kHz as determined experimentally in Chapter 4.

Predicted wire waveguide distal-tip displacements for various damping values are shown in Figure 5.8 and these results show the importance of determining an appropriate damping value for the system. While the effects are minimal in the non-resonant frequencies, near resonance the predicted distal-tip displacement values differ considerably.

Figure 5.9 shows how changes in wire waveguide length can result in large differences in the predicted wire waveguide distal-tip displacements as the wire length is adjusted through resonant and non-resonant lengths. This relationship between length of waveguide and distal-tip displacement appears to be crucial in understanding the behaviour of the waveguide at prescribed ultrasonic frequency. It is this condition that relates closely to our waveguide design and also to the experimental tests of wire waveguide distal–tip displacement versus length conducted in Chapter 4.

From these results it is evident that in order to develop a model that can predict wire waveguide behaviour, the prescribed proximal peak-to-peak displacements, frequency of operation, waveguide length and material properties, including damping, must closely match with those of the actual ultrasonic wire waveguide apparatus.

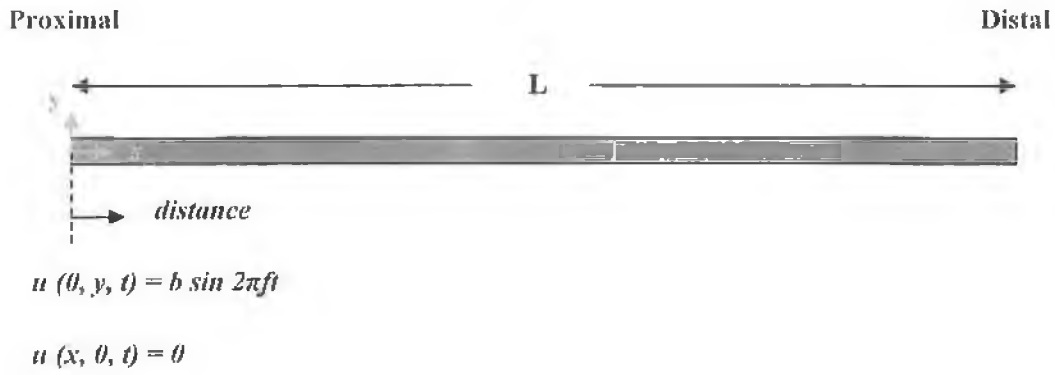

Figure 5.5: Problem sketch for harmonic response analysis of wire waveguide

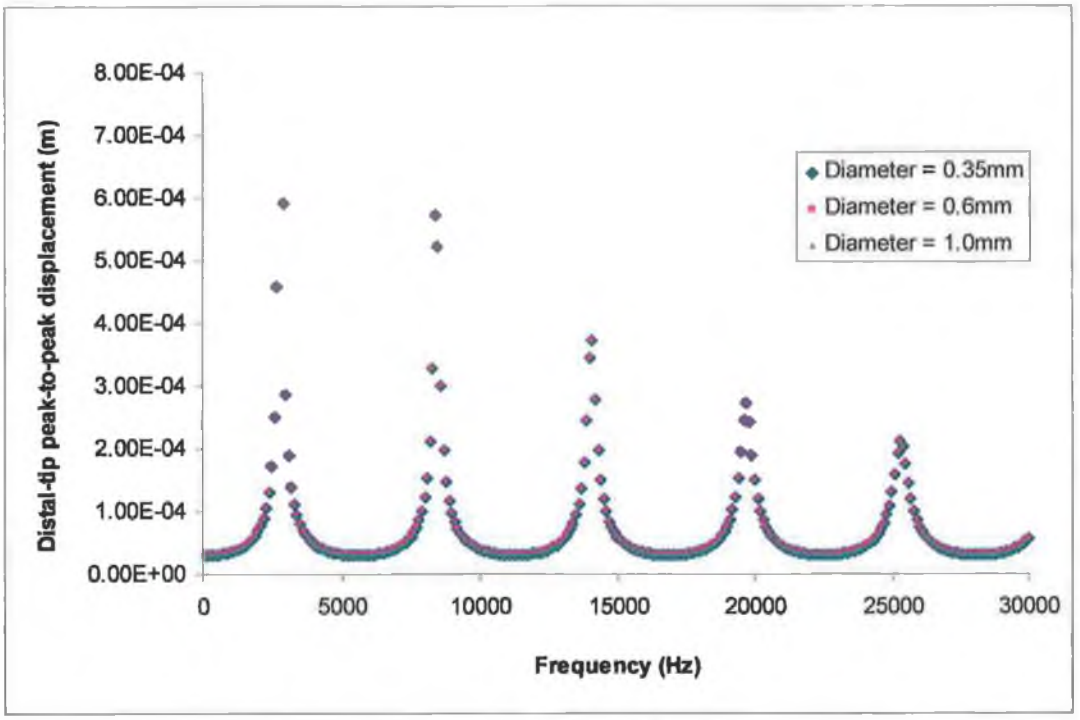

Figure 5.6: Predicted harmonic response of wire waveguide distal-tip peak-to-peak displacements over a frequency range of 0 – 30 kHz, an input displacement of 30 μm, of length 303 mm and an arbitrary damping value of 1%, showing correctly that resonant response is independent of waveguide diameter.

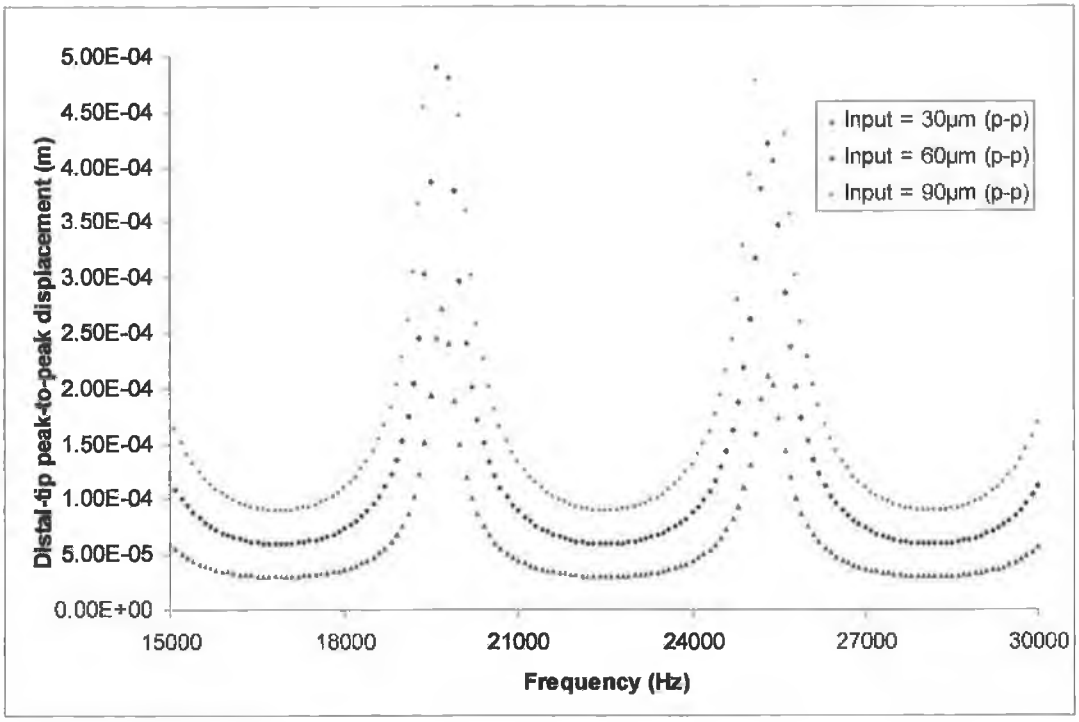

Figure 5.7: Predicted harmonic response of 1.0mm diameter wire waveguide distal-tip peak-to-peak displacements over a frequency range of 15 – 30 kHz for input displacement of 30 µm, 60 µm and 90 µm, of length 303 mm and an arbitrary damping value of 1%

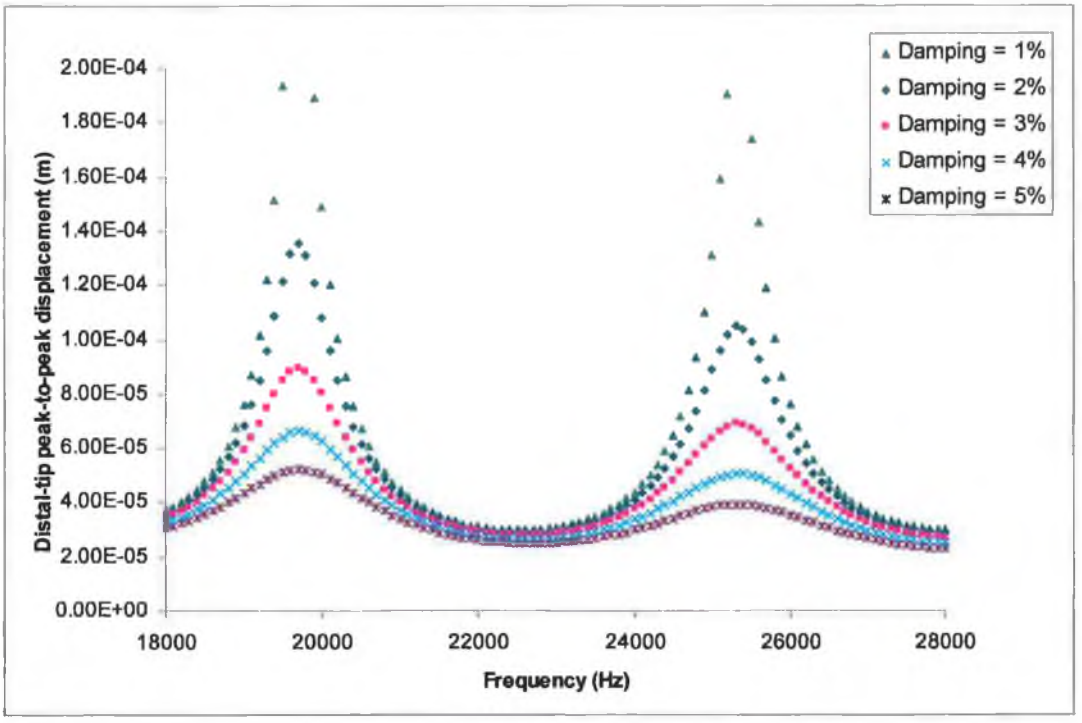

Figure 5.8: Predicted harmonic response of a 1.0mm diameter wire waveguide distal-tip peak-to-peak displacements over a frequency range of 18 – 28 kHz for an input displacement of 30 μm, of length 303 mm and a range of damping values between 1% and 5%

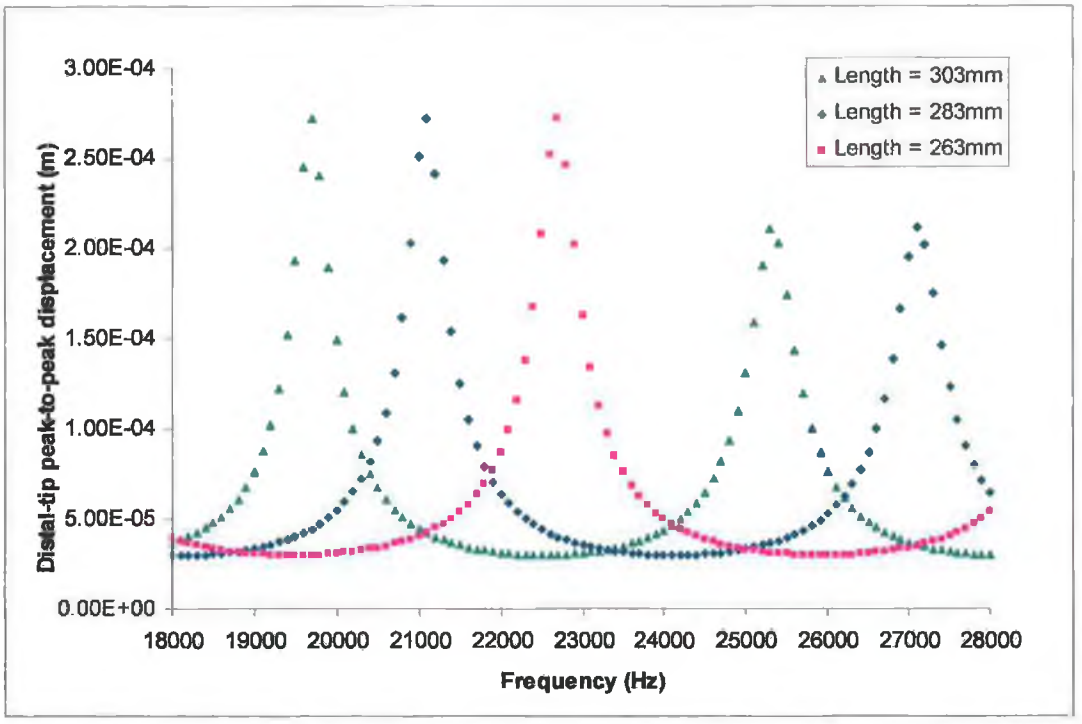

Figure 5.9: Predicted harmonic response of a 1.0mm diameter wire waveguide distal-tip peak-to-peak displacements over a frequency range of 18 – 28 kHz for an inputted displacement of 30 μm, over a range of lengths of 263 mm, 283 mm and 303 mm and an arbitrary damping value of 1%

Figure 5.10 shows the results of predicted wire waveguide distal-tip displacements at a frequency of 23.5 kHz for multiple wire waveguide lengths of 1.0 mm diameter. The lengths of waveguide modelled were in the range of 118 – 303 mm in 5 mm intervals. The prescribed proximal displacement value used was 32 μm and these conditions are comparable with the wire waveguide distal-tip experiments conducted on a 1.0mm diameter waveguide for an input power dial setting of 1.5. The models have been simulated for multiple damping values (4%, 4.5% and 5% shown) in an effort to determine an appropriate damping value for the system.

The results of the models show good comparison when compared with those obtained experimentally when a damping value of 4.5% is used as shown in Figure 5.11. This damping value is similar to values reported in the literature [73]. The numerical models of the wire waveguide not only predict the wire waveguide lengths where resonance and non-resonance occur but also the distal-tip displacements achieved over the range of lengths simulated.

This model has been shown to simulate wire waveguide behaviour and in order to truly validate it against the experimental results and determine its versatility it must be able to model waveguide behaviour for different input displacements (input power dial-settings).

Figure 5.12 compares the results of the waveguide model against the experimental results for an input power dial setting of 2.5. This corresponds to an input displacement of 46 μm as determined for the experimental studies. The model appears versatile as the results determined predict the waveguide distal-tip displacements for this higher input power.

These models of wire waveguide characteristics are post processed further to obtain displacement results, both amplitude and phase along the entire length of the waveguide; the internal steady-state wave structure. These results are converted to peak-to-peak displacements and compared against the experimentally determined displacements measured along the length of waveguide. In addition stresses along the length of waveguide are determined numerically.

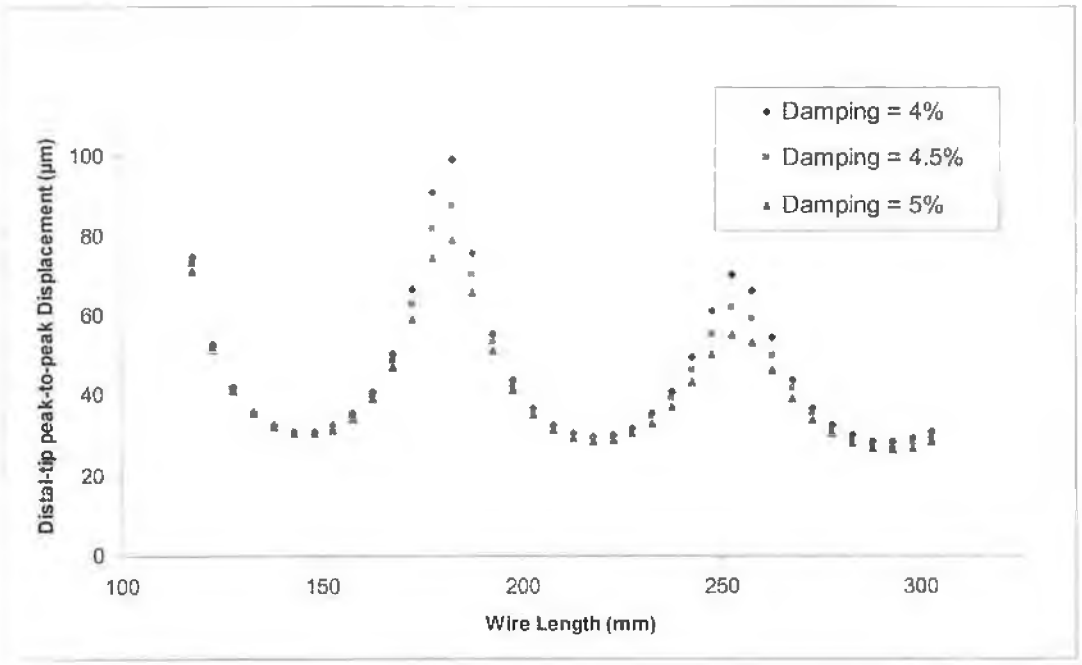

Figure 5.10: Predicted response of a 1.0mm diameter wire waveguide distal-tip peak-to-peak displacements at 23.5 kHz, over a range of lengths from 118 mm – 303 mm, for an inputted displacement of 32 µm and a range of damping values of 4%, 4.5% and 5%.

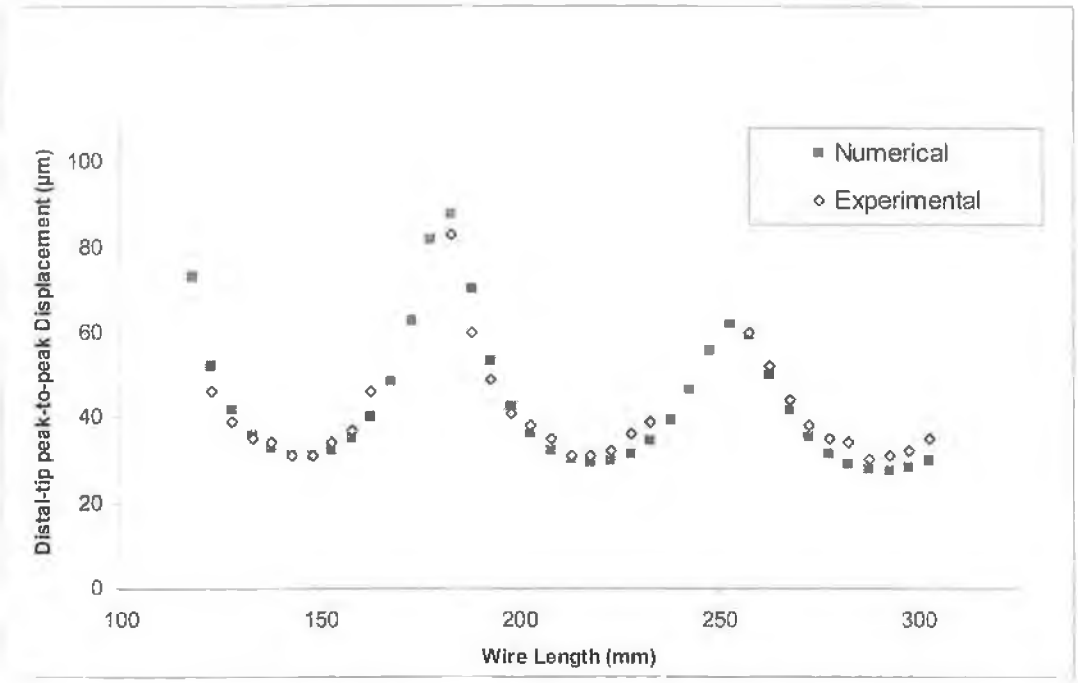

Figure 5.11: Comparison of a 1.0mm diameter wire waveguide distal-tip peak-to-peak displacements, over a range of lengths from 118 mm – 303 mm, for an inputted displacement of 32 µm (power setting = 1.5) and a damping value of 4.5%

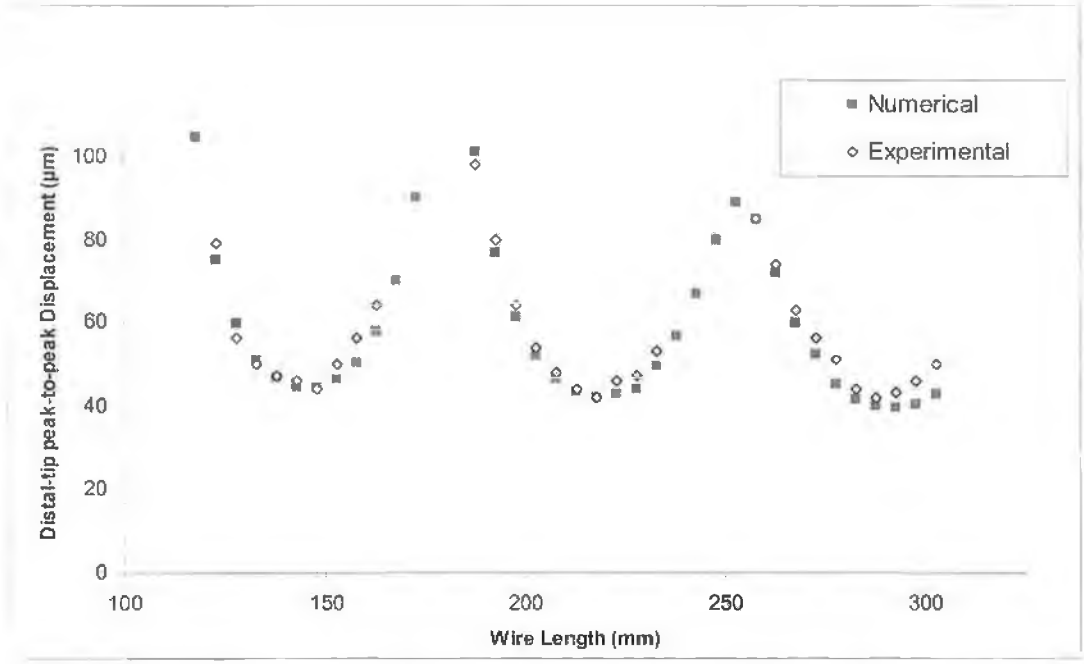

Figure 5.12: Comparison of a 1.0mm diameter wire waveguide distal-tip peak-to-peak displacements, over a range of lengths from 118 mm – 303 mm, for an inputted displacement of 46 µm (power setting = 2.25) and a damping value of 4.5%

Figure 5.13 shows the predicted internal displacements for an undamped 1.0 mm diameter wire waveguide model of 288 mm length with an input displacement of 32 μm at 23.5 kHz and compare it to the analytical solution given in Equation 2.1. An excellent comparison is achieved and the results show a standing wave structure with a series of displacement nodes and antinodes along the length of the waveguide. In addition, the numerical model can predict the internal stresses in the wire waveguide as shown. This is a simplified undamped model, however, but with the inclusion of the damping value of 4.5% the internal displacements can be compared with the experimentally determined results.

Figure 5.14 shows the predicted internal displacements (p-p), displacement phase and stresses for a 288 mm wire waveguide, with an input displacement of 32 μm at 23.5 kHz and the determined damping value of 4.5% and compares it to the experimental results of internal peak-to-peak displacements.

A few notable differences in the internal wave structure appear with the inclusion of the damping value. The undamped solution of the near non-resonant wire waveguide length of 288 mm, as shown in Figure 5.13 predicts a series of displacement nodes and antinodes along the waveguide length. Displacement antinodes occur at both the proximal and distal ends (32 μm (p-p)) and as a result the corresponding internal stress at these locations for this length is near a stress node with a near zero value. At displacement nodes stress is at a maximum and a maximum stress value of 51.8 MPa is predicted.

With the inclusion of the damping value, Figure 5.14, a series of displacement maxima and minima are now predicted and show good comparison in terms of the displacement values predicted and the location of maxima and minima with the experimentally determined internal displacements. The losses due to damping have reduced the predicted distal-tip displacements to 28 μm (p-p). Also, while the proximal end of the wire waveguide is still on a displacement maximum the stress at this location is no longer nearly zero and stress is now predicted to have a maximum value of 28 MPa.

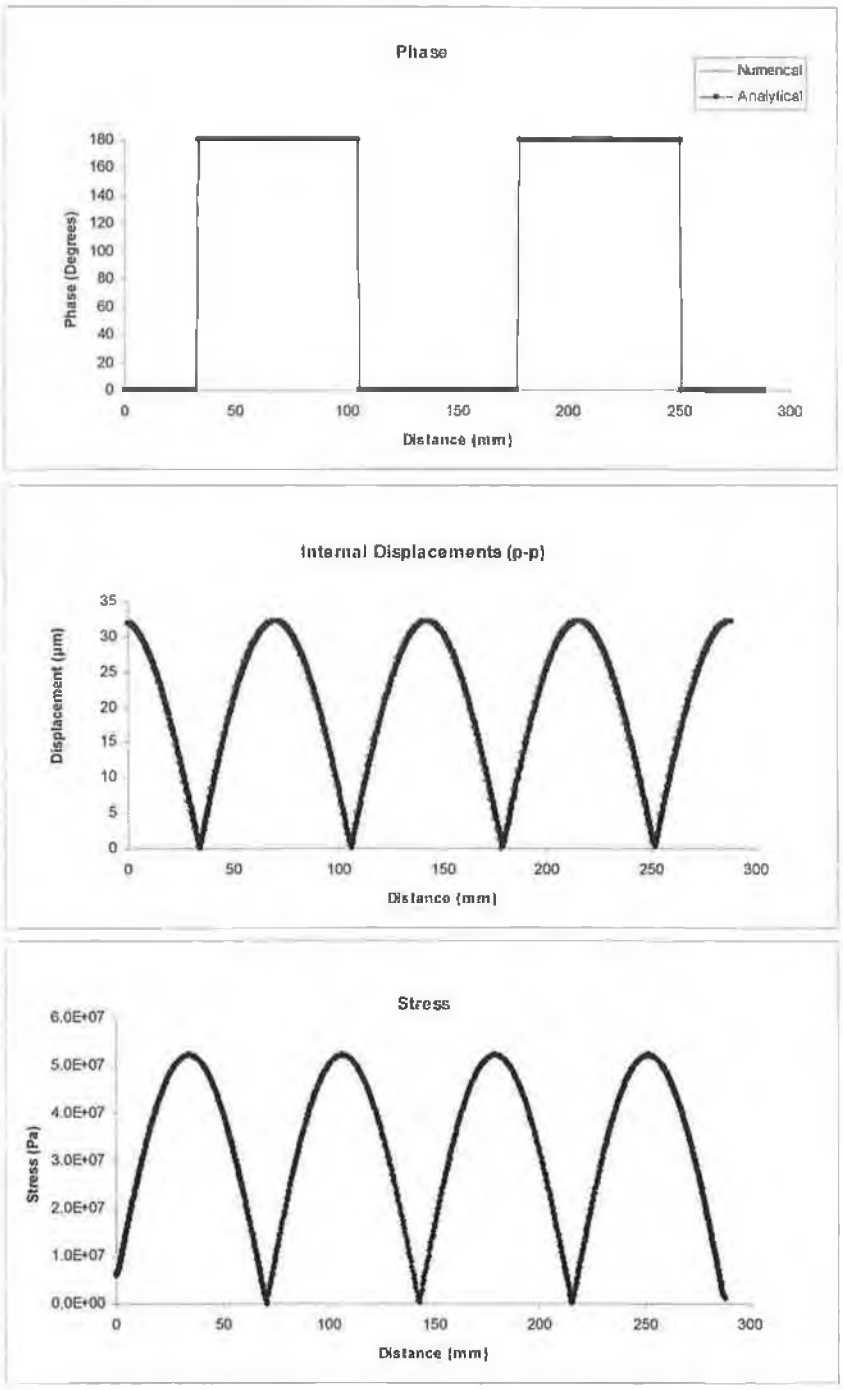

Figure 5.13: Comparison of numerical (no damping) and analytical 1.0mm diameter wire waveguide (l=288 mm) internal displacements and numerically determined internal stress

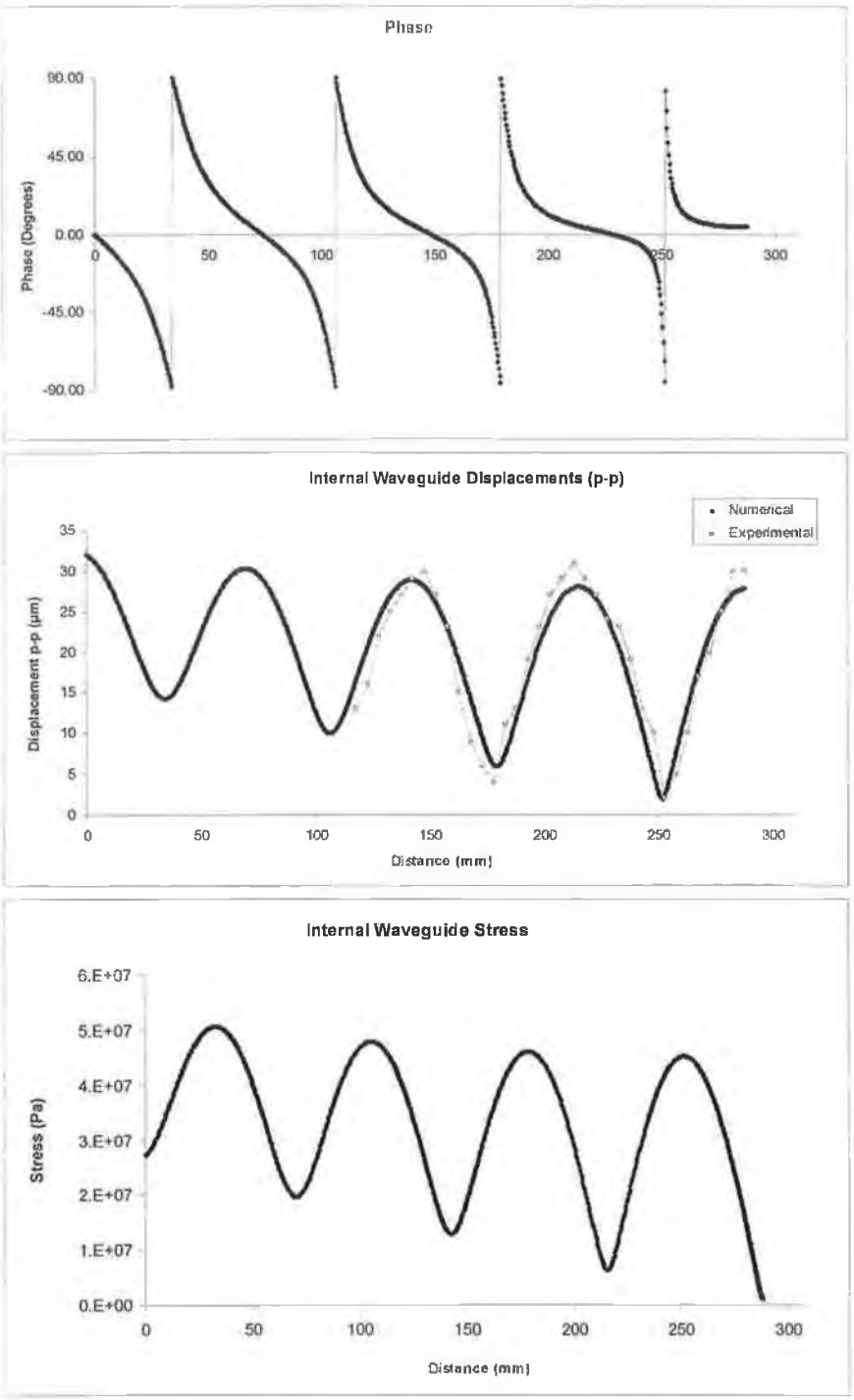

Figure 5.14: Comparison of numerical (damping = 4.5%) and experimental 1.0mm diameter wire waveguide (l=288 mm) internal displacements and numerically determined internal stress

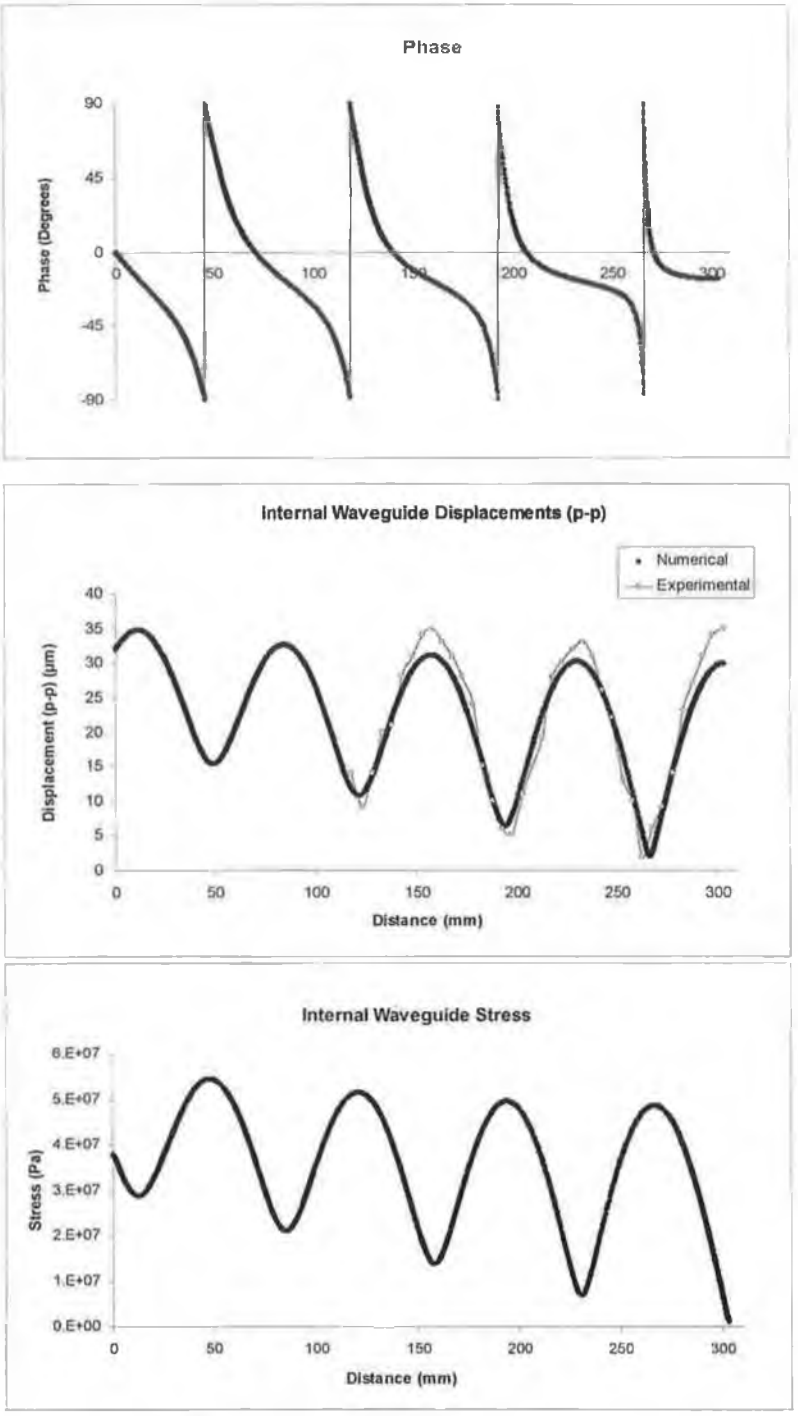

Figure 5.15: Comparison of numerical (damping = 4.5%) and experimental 1.0mm diameter wire waveguide (l=303 mm) internal displacements and numerically determined internal stress

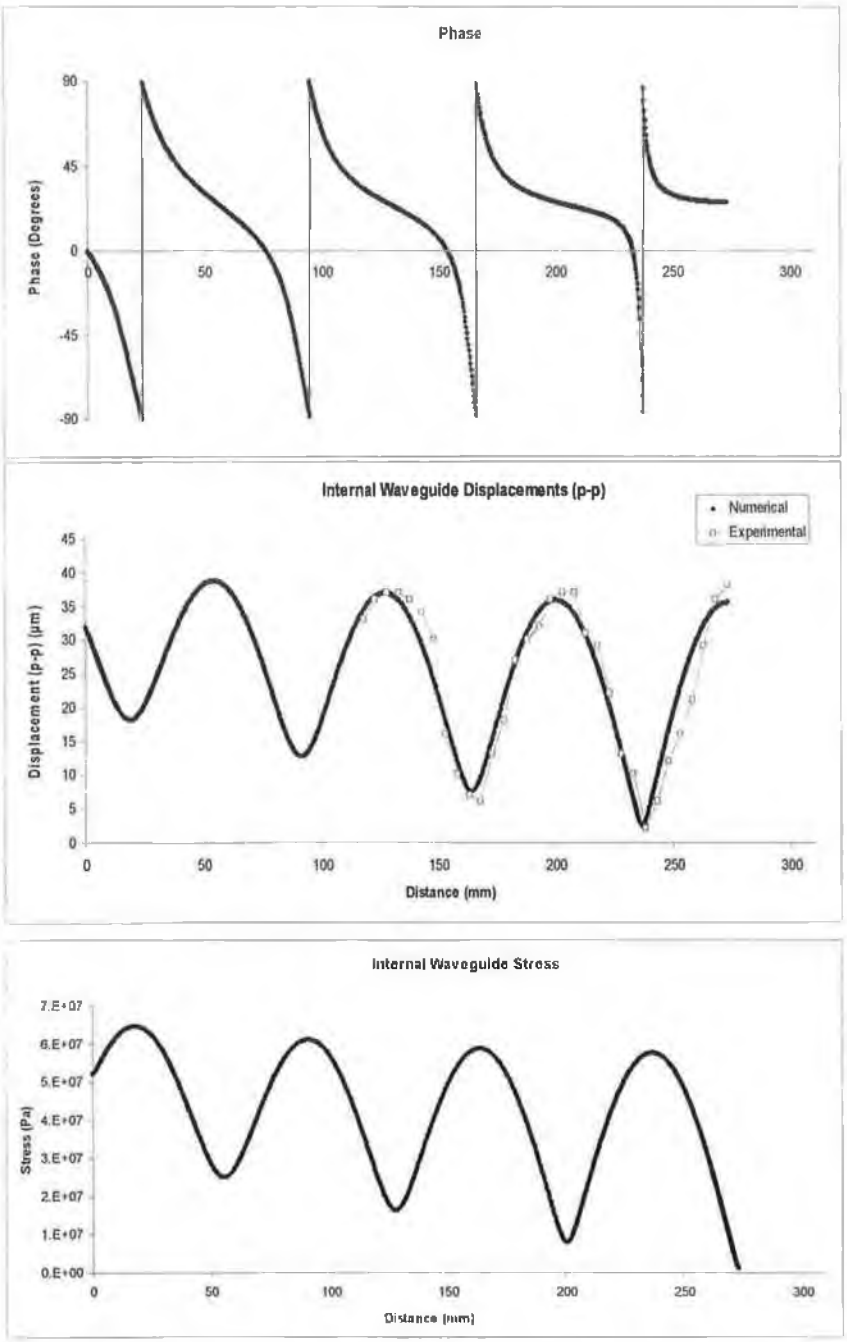

Figure 5.16: Comparison of numerical (damping = 4.5%) and experimental 1.0mm diameter wire waveguide (l=273 mm) internal displacements and numerically determined internal stress

This stress at the proximal end is due to losses in the waveguide and a further inputted stress is required to sustain the input displacement (p-p). This is the cyclic stress on the radiating face of the acoustic horn as it sustains the applied cyclic displacement. For the 1.0 mm wire waveguide modelled the cyclic force on the radiating face of the acoustic horn can be calculated as having a maximum value of 22 N. The maximum stress predicted in the wire waveguide for this configuration is 50.5 MPa and is well within the austenitic elastic range for the NiTi wire waveguide reported in Chapter 3.

Figure 5.15 shows the predicted internal displacement results for a 303 mm wire waveguide and compare them to the equivalent experimentally determined displacements (p-p). This length is closer to a resonant length and as a result experimental displacement results showed an increase in internal peak-to-peak displacements and the numerical model predicts this behaviour.

These greater internal displacements, however, result in larger internal stresses. Stress at the proximal end of the waveguide is predicted to have a maximum value of 36.8 MPa while the maximum internal stress is 54.3 MPa. Similar results are shown in Figure 5.16 for a wire waveguide of length 273 mm, closer again to a resonant length. Increased internal displacements result in a further increase in the predicted internal stresses with the maximum stress at the connection point equal to 52.2 MPa and a maximum stress in the waveguide of 64.6 MPa.

The force at the proximal end of the 1.0mm wire waveguide of 273 mm length is calculated to be a value of 41 N. This increase in force acting on the radiating face of the acoustic horn is the reason why the ultrasonic apparatus fails to operate at resonant lengths of wire waveguide. As mentioned earlier, Perkins [54] has suggested for acoustic horns that excessive amplification at resonance can cause the system (converter and horn) to stall. This is consistent with what was observed in the experimental tests at near resonant lengths in Chapters 3 and 4.

Figure 5.17 shows the predicted distal-tip frequency response results for a 0.35 mm diameter wire waveguide of length 500 mm with no distal tip, a spherical 1.0mm diameter ball-tip and a spherical 1.5 mm diameter ball-tip. These

dimensions are similar to those reported in the literature and will be used in the fluid interaction model.

The results of the model show that the frequency response is moderately affected by the presence of the spherical ball-tips and that with increasing ball-tip diameter the response is further effected. This is similar to a rod with a concentrated mass at the distal end which loads the distal-end of the waveguide and shifts the resonant frequencies as described by Steidel [65]

The peak-to-peak displacements predicted at the distal-end of the waveguide appear to be affected to a greater degree with a loss in amplitude for increasing ball-tip diameter.

The inclusion of a fluid surrounding the distal-tip of the wire waveguide will further affect this resonant response and this is investigated in the Section 5.4.

5.3.7 Summary of Harmonic Analysis of Wire Waveguide

A model that can predict the behaviour of a wire waveguide with no distal load subjected to an applied ultrasonic input displacement has been developed and validated against the experimental displacement measurements made on the ultrasonic wire waveguide apparatus.

The results show the critical relationship between distal-tip displacement and wire waveguide length as the length of the waveguide is varied between resonant and non-resonant lengths. The inclusion of the damping value has allowed for the accurate prediction of distal-tip displacements for a range of NiTi wire waveguide lengths.

The model predicts the internal standing wave structure and is validated further against the experimental measurements of internal displacement made on the ultrasonic wire waveguide apparatus.

This model can also predict the internal stresses in the wire waveguide and in particular at the connection point to the acoustic horn and shows that an increase in waveguide damping or internal displacements due to operating near resonant

lengths all result in greater force acting on the radiating face of the horn and possibly explains why the system cannot operate near resonant waveguide lengths.

The inclusion of distal-tip geometries has shown that for the range of values modelled, representing those reported in the literature, the resonant response of the waveguide is only moderately affected. The inclusion of a fluid-structure interaction model at the distal tip of the wire waveguide will enhance the model further.

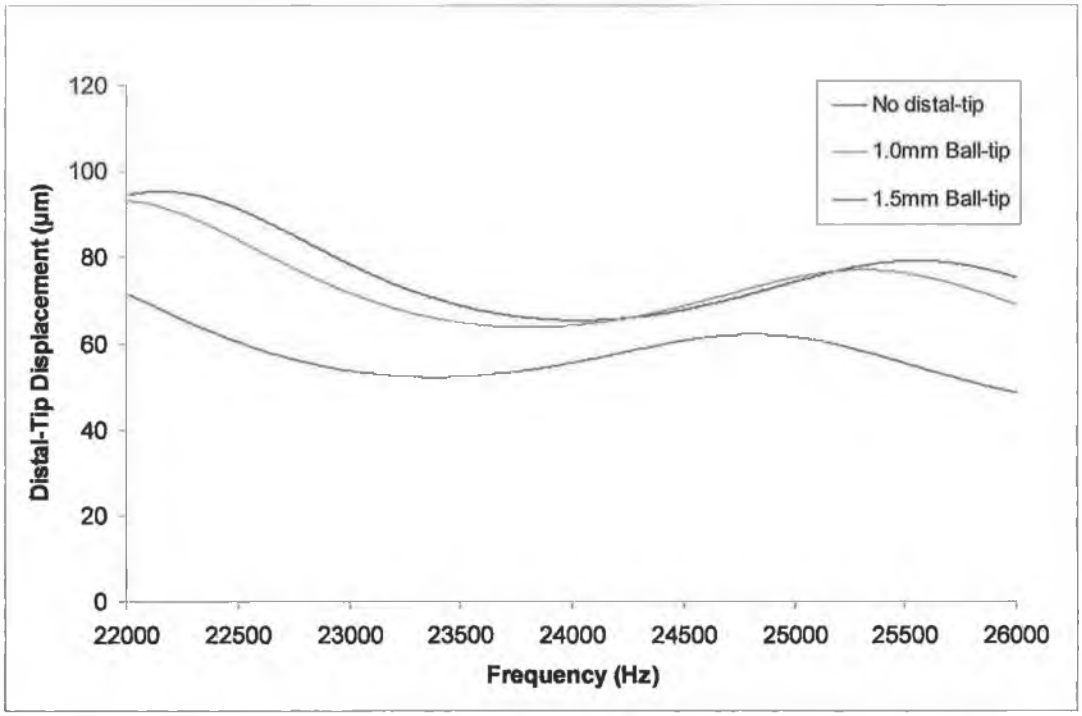

Figure 5.17: Comparison of predicted frequency response of wire waveguide distal-tip peak-to-peak displacements for a 0.35 mm wire waveguide (l= 500mm) with and without spherical distal ball-tips. Input displacement is 100 µm and damping is 4.5%

5.4 Coupled Fluid-Structure Model of Wire Waveguide

The harmonic structural model developed in the previous section predicts the harmonic response of the wire waveguide and has been validated against experimental distal-tip and displacement response along the length of the waveguide. It has also been shown numerically that the inclusion of various distal-tip geometries has only a negligible effect on the waveguide resonant response.

These models, however, assume that the distal-tip of the wire waveguide has no force acting on it. In the normal operation condition in the treatment of atherosclerotic lesions and thrombus this in not the case as there is a fluid, blood, surrounding the distal-tip. Since this form of energy causes pressure waves in surrounding fluid as reported by Makin and Everbach [62] the fluid must also be applying a load back on the distal-tip of the waveguide.

This acoustic fluid-structure model of the wire waveguide, distal-tip geometry and surrounding fluid will address this issue and predict the effect of the fluid on the resonant frequencies and the standing wave structure in the wire waveguide. The fluid part of this model will predict the acoustic pressure field developed around the distal-tip of the wire waveguide and will allow for the prediction of the conditions leading to the highly disruptive cavitation and its location.

5.4.1 Acoustic Fluid-Structure Method

The interaction of the fluid nodes and structural nodes at the fluid-structure interface is such that the pressure in the acoustic field exerts an applied force on the structural elements that produce an effective fluid load [68]. The governing equations for both the fluid nodes and structural nodes (similar to equation 5.2) are:

$$\text{Structural:} \quad [M_S](\ddot{\vec{u}}) + [K_S](\vec{u}) = (\vec{F}_S) + [R](\vec{P}) \tag{5.5}$$

$$\text{Fluid:} \quad [M_F](\ddot{\vec{P}}) + [K_F](\vec{P}) = (\vec{F}_F) - \rho_0 [R]^T (\ddot{\vec{u}})$$

where $(\ddot{\vec{P}})$ and $(\vec{P})$ = the 2nd derivative of nodal pressure and nodal pressure respectively.

$[R]$ = a coupling matrix that represents effective area associated with each node

The equations given in Equation 5.5 can be combined into a single equation that describes load quantities at all locations in fluid and structure as shown in Equation 5.6.

Combined:
$$\begin{bmatrix} M_S & 0 \\ \rho_0 R^T & M_F \end{bmatrix} \begin{pmatrix} \ddot{\vec{u}} \\ \ddot{\vec{P}} \end{pmatrix} + \begin{bmatrix} K_S & -R \\ 0 & K_F \end{bmatrix} \begin{pmatrix} \vec{u} \\ \vec{P} \end{pmatrix} = \begin{pmatrix} \vec{F}_S \\ \vec{F}_F \end{pmatrix} \qquad (5.6)$$

In terms of modelling, an axisymmetric model of the wire waveguide and distal-tip acoustic fluid was used. Fluid elements Acoustic29 (2D axisymmetric 4-node fluid element) were used and the fluid structure interface (FSI) was identified and must lie on coincident nodes of both structural and fluid element types. An infinite acoustic circular boundary layer, Acoustic129 (2D axisymmetric 4-node fluid element), is placed at the extremities of the model and prevents reflection of pressure components back into the model as shown in Figure 5.18.

The predicted pressure results from the model are returned in real, P_R, and imaginary, P_I, component form. With the actual pressure amplitude above mean pressure given by:

$$P_{\max} = \sqrt{P_R^2 + P_I^2} \qquad (5.7)$$

Initially a fluid-structure model for a wire waveguide with spherical distal-tip and surrounding fluid is developed as the acoustic fluid results of this model can be compared with the analytical solution for an oscillating sphere presented in the literature survey.

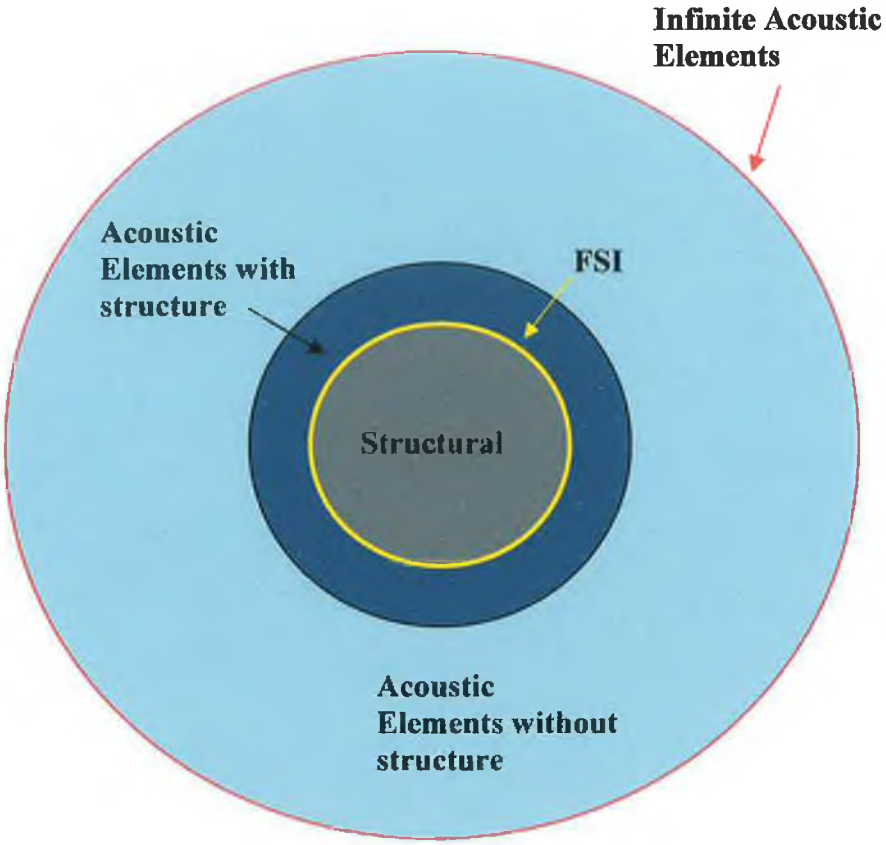

Figure 5.18: Schematic of Numerical Fluid-Structure Modelling

5.4.2 Fluid-structure model of spherical distal-tip

Acoustic fluid-structure models of a 0.35 mm diameter wire waveguide of 500 mm length with spherical distal ball-tips of 1.0 mm and 1.5 mm diameter were developed. The physical properties used for the fluid were those of blood including the speed of sound in the material ($\approx$1580 ms^{-1}) and fluid density ($\approx$1050 kgm^{-3}) [78].

The model of the 0.35 mm diameter waveguide with a 1.0 mm distal-tip is shown in Figure 5.19. The structural results of these models predicts the effect the presence of the fluid load will have on the harmonic response of the wire waveguide while the fluid results predict the acoustic pressure field developed surrounding the distal-tip.

The acoustic pressure field results of a spherical tip can be compared with the analytical results of an oscillating sphere [60] and the cavitation threshold intensities can allow for the prediction of where in the field cavitation will occur and for what tip displacements and geometry.

Figure 5.20 shows a contour plot of the predicted acoustic pressure (real) field around the 1.0 mm diameter spherical distal-tip. Also shown are the axial line '0X' and the radial line '0R' which relate to pressure plots discussed later.

The harmonic response of the distal-tip displacements results of the wire waveguide with both a 1.0 mm and 1.5 mm diameter ball-tip, shown in Figure 5.21 and Figure 5.22, predict that the presence of the fluid and the subsequent force it exerts on the wire waveguide has a negligible affect on the resonant response. The minor effect is, however, more pronounced in the waveguide with the larger distal-tip ball-tip of 1.5 mm diameter. These results suggest that the overall standing wave structure and lengths where resonance and non-resonance occurs are not significantly affected due to the presence of the ball-tip and fluid for ball-tip sizes modelled.

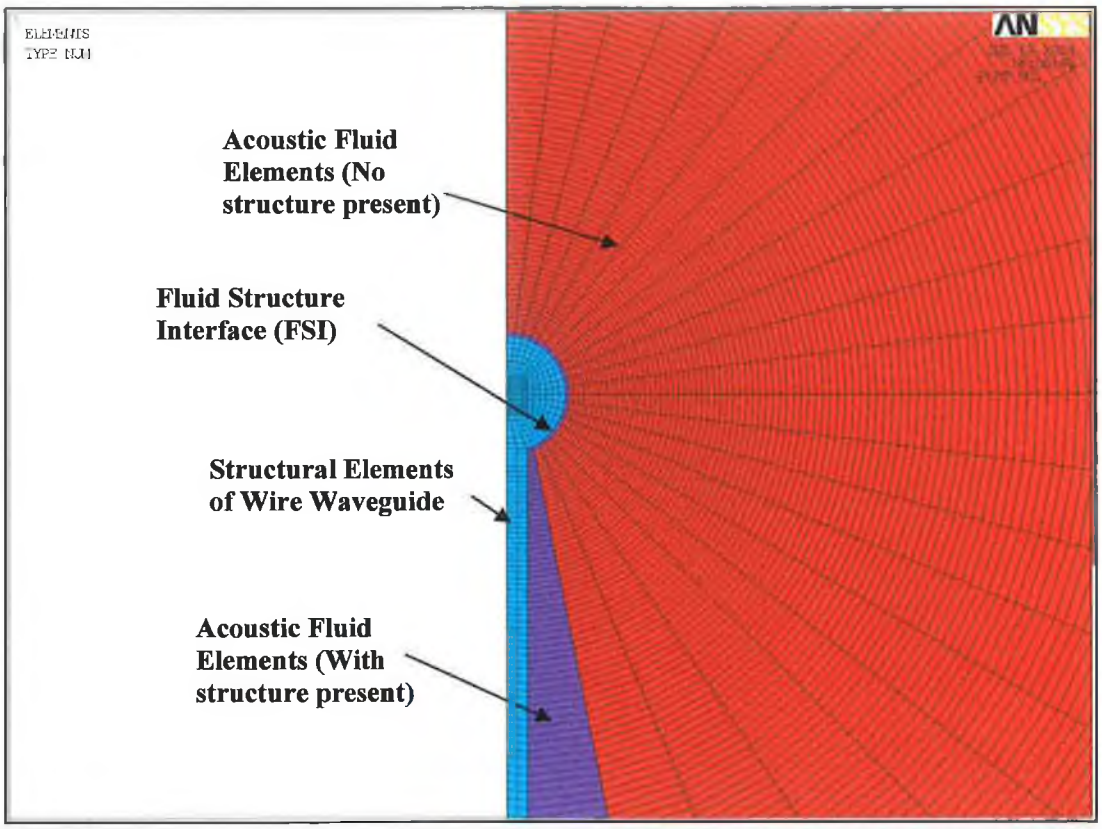

Figure 5.19: Distal Section of Acoustic Fluid Structure Model of Wire Waveguide with 1.0 mm spherical ball-tip

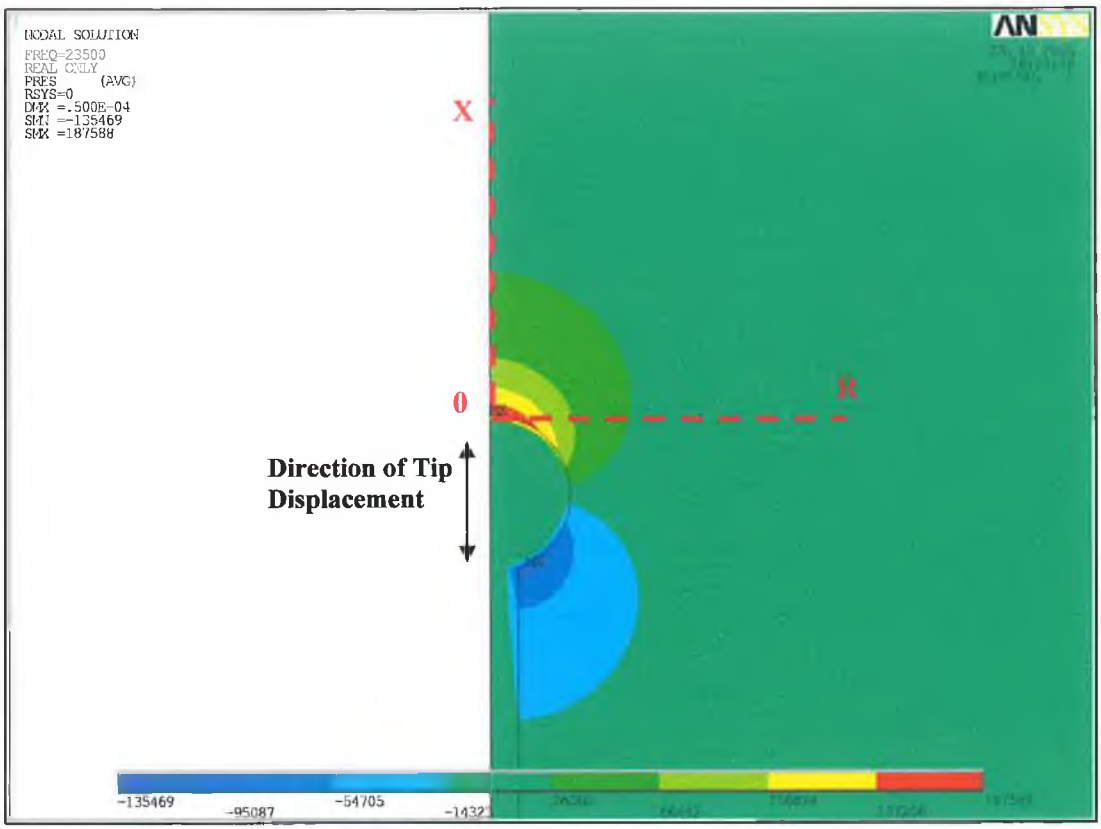

Figure 5.20: Predicted pressure field (real) around distal section of acoustic fluid structure model of wire waveguide with 1.0mm spherical ball-tip. Distal -tip displacement is 64.5μm at 23.5 kHz.

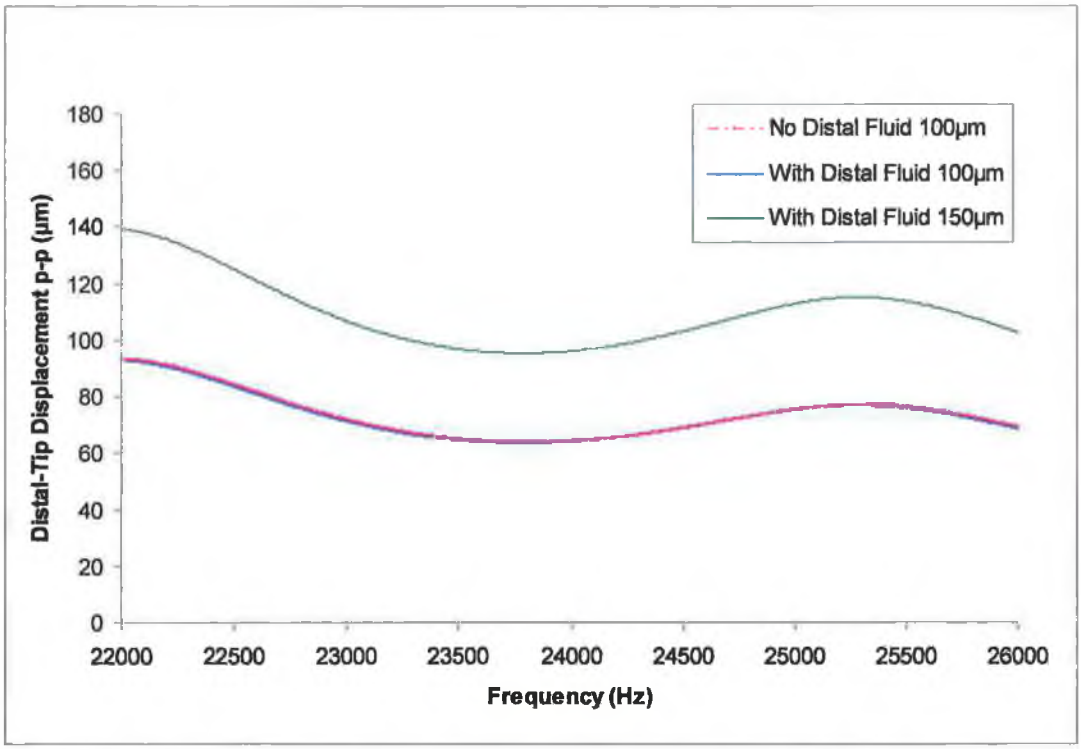

Figure 5.21: Comparison of predicted frequency response of wire waveguide distal-tip peak-to-peak displacements for a 0.35 mm wire waveguide (l = 500mm) with a 1.0 mm diameter spherical distal ball-tip and with a surrounding fluid. Input displacement is 100 µm and 150 µm (p-p).

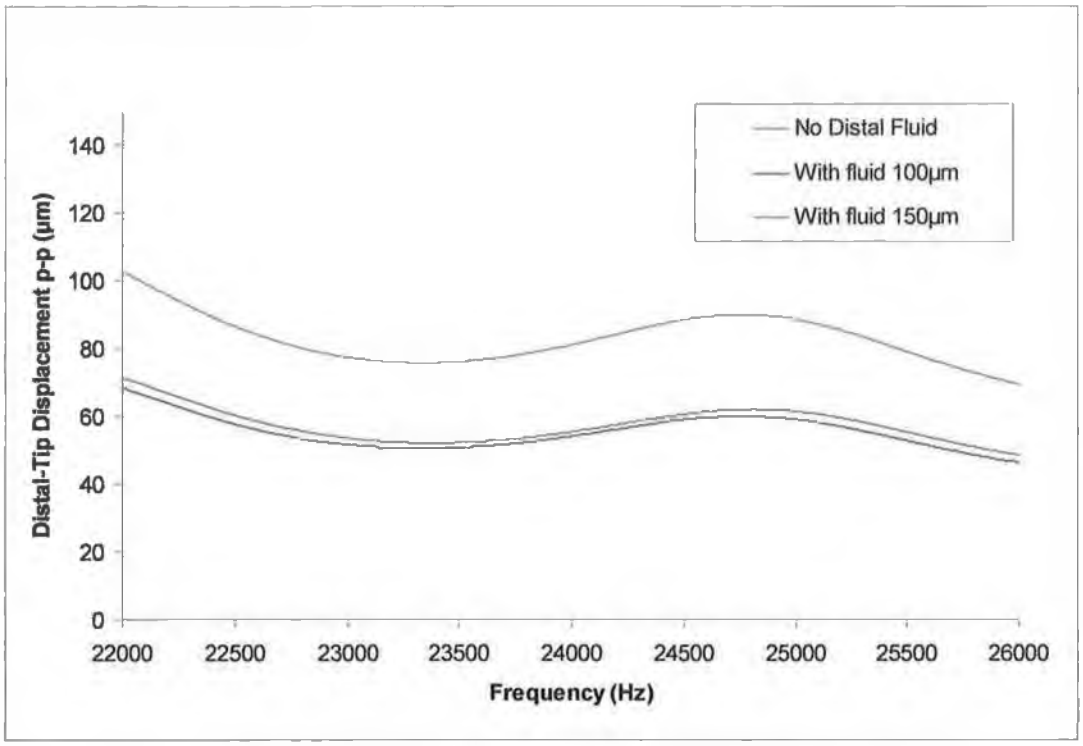

Figure 5.22: Comparison of predicted frequency response of wire waveguide distal-tip peak-to-peak displacements for a 0.35 mm wire waveguide (l= 500mm) with a 1.5 mm diameter spherical distal ball-tip and with a surrounding fluid. Input displacement is 100 µm and 150 µm (p-p).

The predicted axial (line '0X') acoustic pressure (amplitude) results from the fluid part of the model of the 0.35 mm diameter waveguide with a 1.0 mm diameter spherical ball-tip are shown in Figure 5.23 and compared with the analytical solution, shown in Equation 5.8 [60], of a 1.0 mm diameter oscillating sphere with same peak-to-peak displacement (64.5μm) and frequency (23.5 kHz).

$$P_{\max} = 2\pi^2 \rho R f^2 d_0 \times \frac{R^2 |\cos\theta|}{r^2} \tag{5.8}$$

The results show a good comparison for this simple spherical distal-tip shape and both predict pressure amplitudes of approximately 185,000 Pa near the tip of the waveguide. With a cavitation threshold intensity, for degassed water at room temperature, in the region of 2.5 W/cm^2 as given in Figure 2.12 the pressure amplitude for which cavitation will take place, as shown in Equation 5.9 [57], can be calculated as approximately 288 kPa. However, this is an upper end value and the presence of additional nuclei in the blood and around the tip may considerably reduce this pressure required to cause cavitation to between 100 kPa and 200 kPa [54, 58].

$$T = \frac{P_m^2}{2\rho c} \tag{5.9}$$

Figures 5.24 shows the predicted pressure amplitudes along the axial line '0X' and Figure 5.25 shows the predicted pressure amplitudes along radial line '0R' for distal tip ball-tips of 1.0 mm and 1.5 mm diameter for a range of tip displacements (p-p). The results show that an increase in ball-tip diameter of displacement results in an increase in the pressures predicted in the region close to the tip and the overall region where cavitation can take place increased.

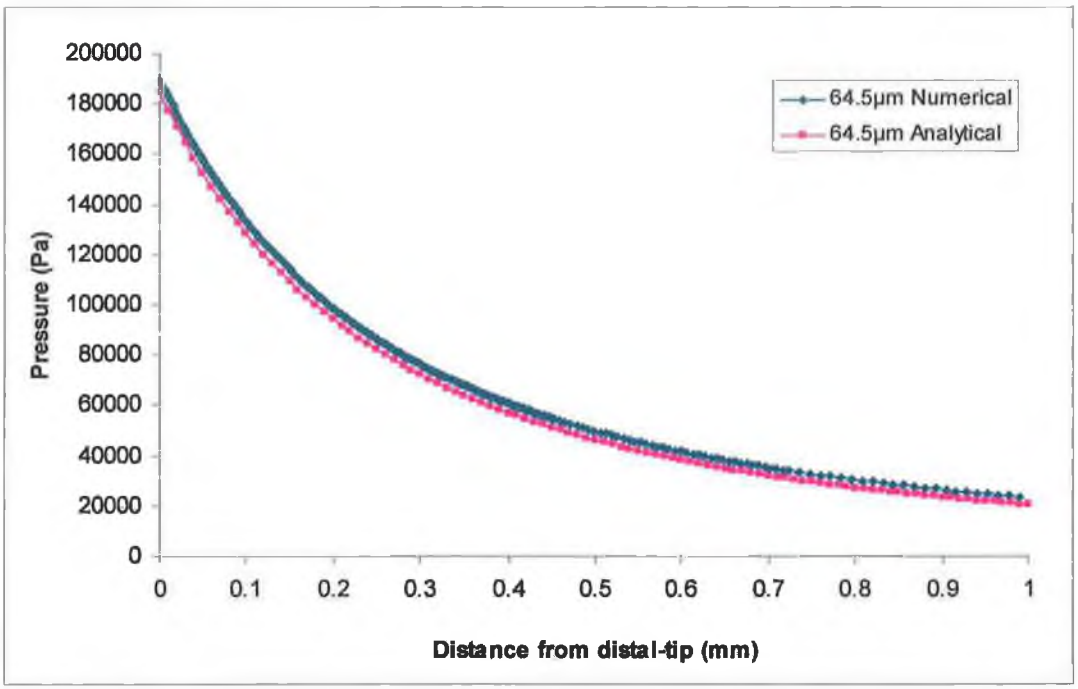

Figure 5.23: Comparison of predicted pressures and analytically determined pressures along axial line '0X' for a wire waveguide with a 1.0 mm spherical ball-tip. Distal -tip displacement is 64.5 µm at 23.5 kHz.

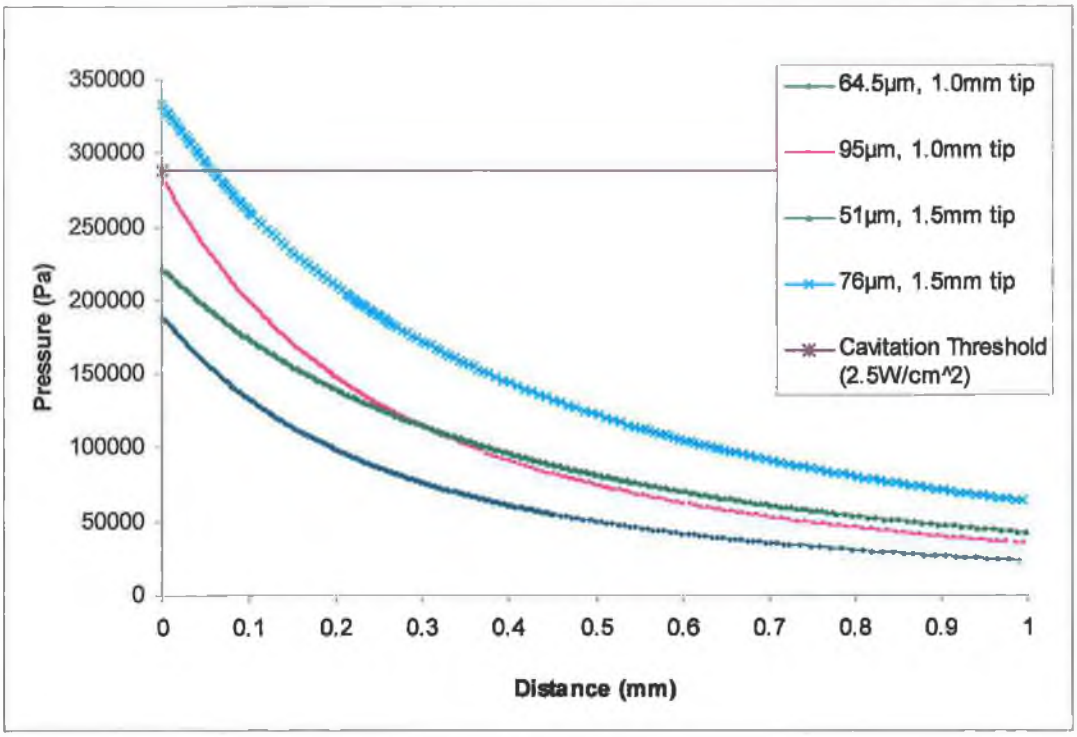

Figure 5.24: Comparison of predicted pressures along axial line '0X' for a wire waveguide with a 1.0 mm and 1.5 mm diameter spherical ball-tip for various distal-tip displacements at 23.5 kHz. Cavitation threshold (2.5 W/cm^2) line also shown.

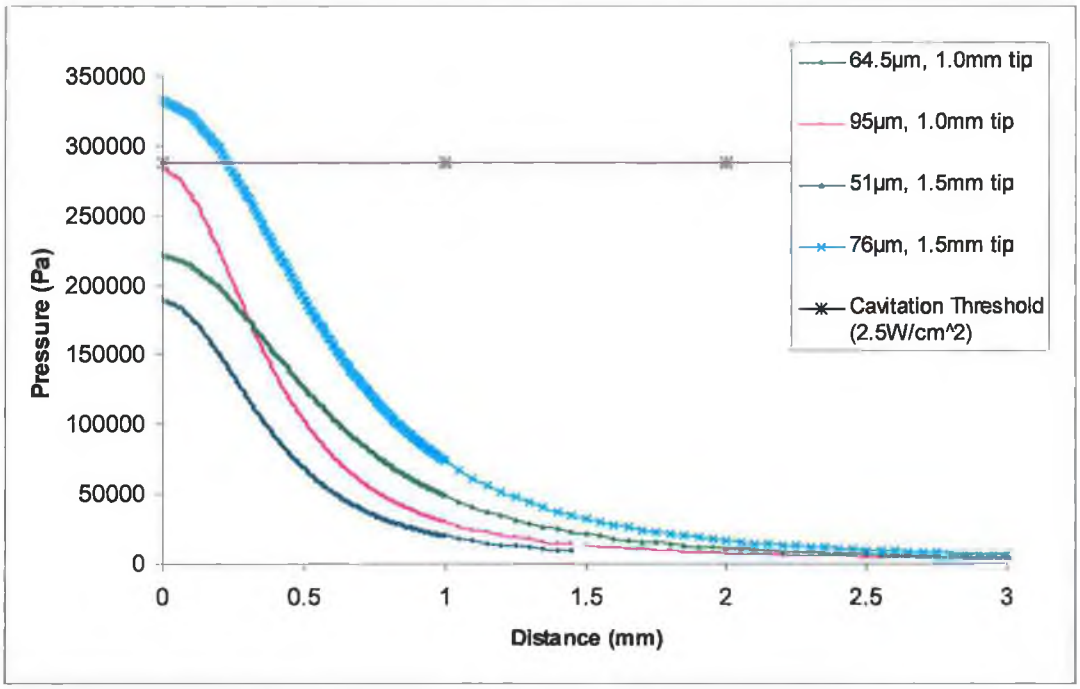

Figure 5.25: Comparison of predicted pressures along radial line '0R' for a wire waveguide with a 1.0 mm and 1.5 mm diameter spherical ball-tip for various distal-tip displacements at 23.5 kHz. Cavitation threshold (2.5 W/cm^2) line also shown.

Figure 5.26 shows the predicted pressures in the form of a 3-dimensional pressure field map for a 0.35 mm diameter wire waveguide with a 1.5 mm diameter tip with a peak-to-peak displacement of 51 μm.

Some experimental measurements of the pressure amplitudes in the field surrounding a vibrating wire waveguide with ball-tips have been performed by other authors [62] as discussed in the literature survey. Based on the information about the device provided, an acoustic fluid -structure model was developed as shown in Figure 5.27. The predicted acoustic pressure field results from the model were compared with the experimental results reported.

Figure 5.27 shows a contour plot of the predicted pressures around the model of the distal-tip of the device described by Makin and Everbach [62]. Figure 5.28 show the good comparison of the numerically determined pressures and the experimentally reported pressures along the axial line ahead of the distal-tip. These results start at a distance of 12 mm from the distal-tip as experimental measurements were not reported in the region closer to the tip although the authors concluded that based on the trend of these results pressures sufficient to cause the observed cavitation were generated in the region close to the tip. The numerical model developed as part of this thesis predicted these pressures as high as 1 MPa in this region.

Makin and Everbach [62] also presented some of their experimental measurements in the form of 3-D acoustic pressure field maps. No exact details of distal-tip displacements for these pressure measurements are documented although the authors state the input power level is very low. A fluid-structure model has been developed based on the available description and with a distal-tip displacement of 6.5 μm and a pressure field map was created based on the numerical results. Figure 5.29 shows the pressure field maps for both the reported experimental measurements and pressures predicted by the numerical model developed in this project. Both set of results show that the pressures radiated from a source increase considerably in the region close to the tip.

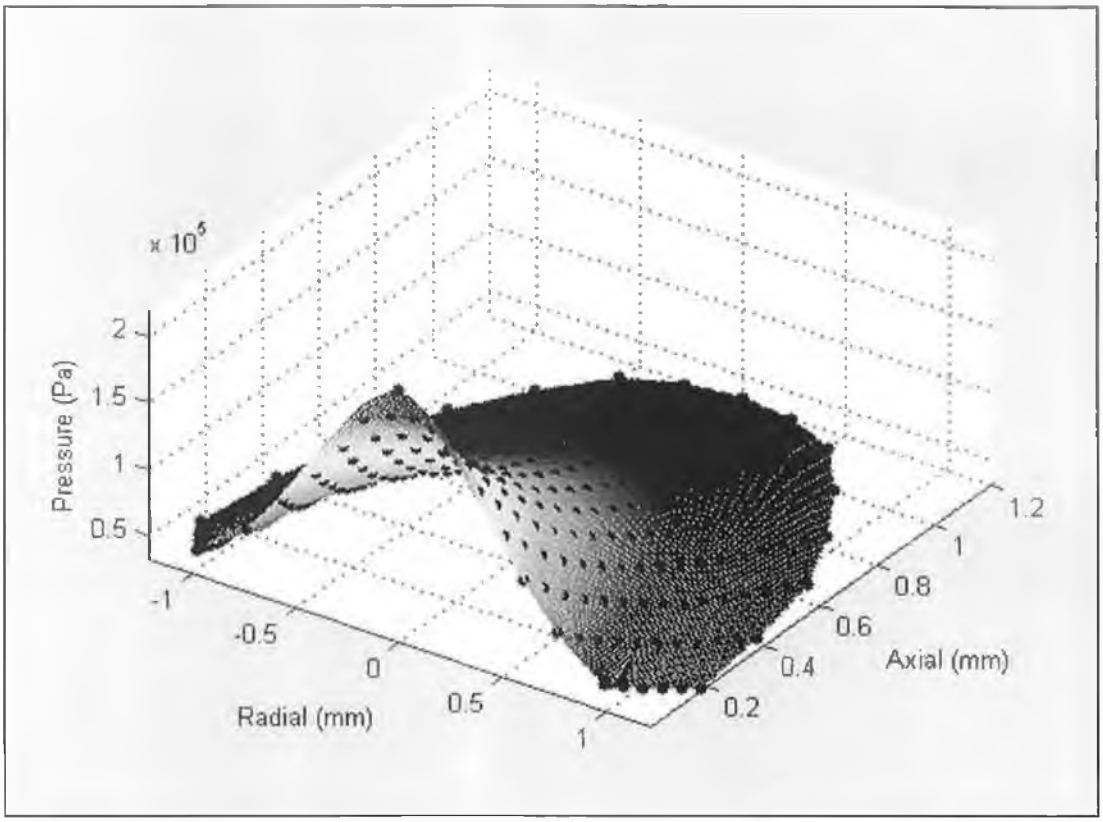

Figure 5.26: Predicted surface pressure field (nodal results) for a wire waveguide with a 1.5 mm spherical ball-tip. Distal -tip displacement is 51 μm at 23.5 kHz.

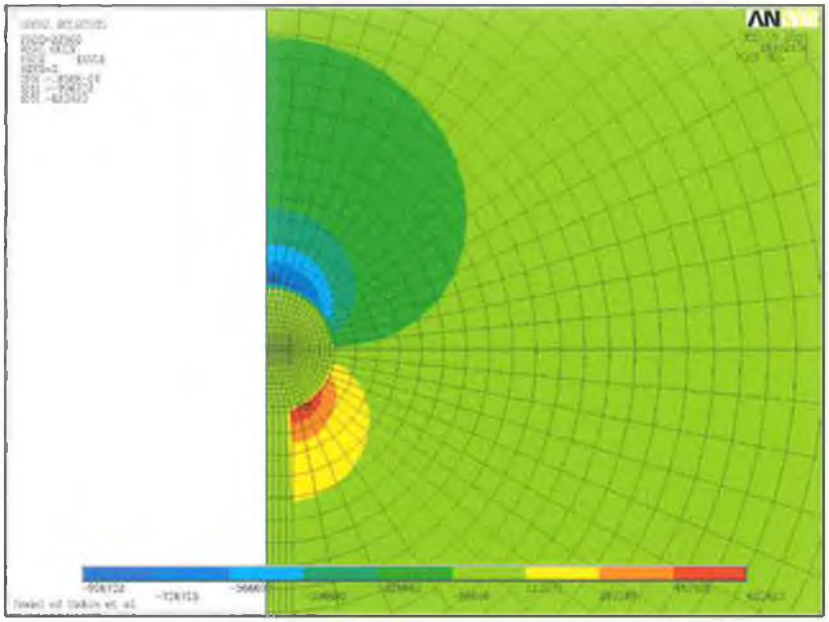

Figure 5.27: Predicted pressure (real, Pa) field around distal section of acoustic fluid structure model of wire waveguide with 2.46 mm spherical ball-tip and distal - tip displacement of 130 μm at 22.5 kHz as described by Makin et al [62]

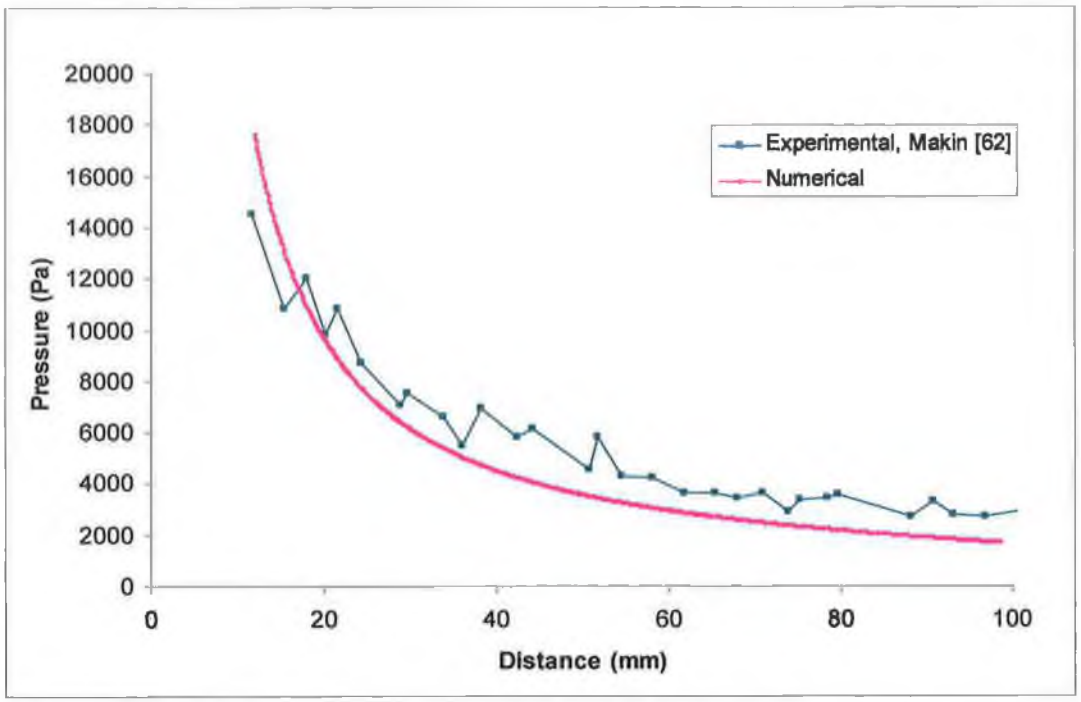

Figure 5.28: Comparison of predicted pressures and experimental results along axial line ahead of distal-tip for a model based on device described by Makin et al [62]

a)

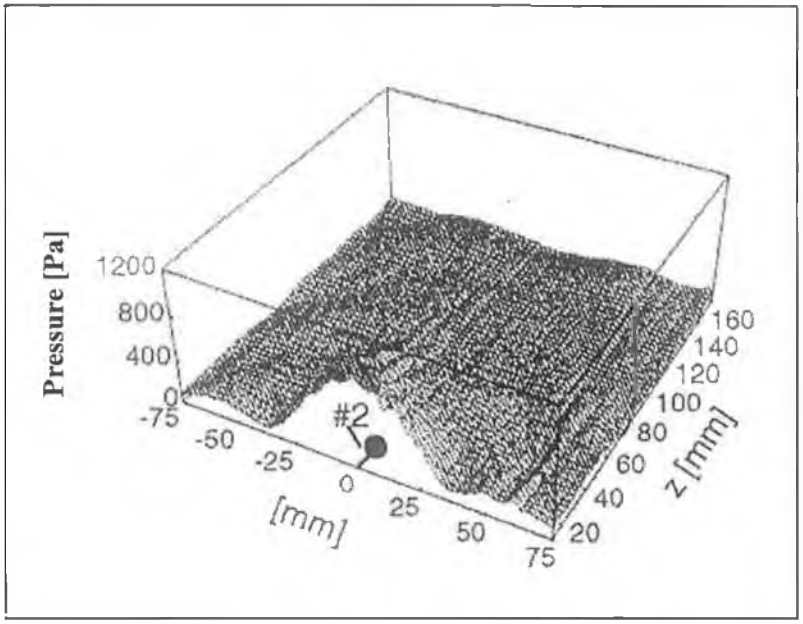

b)

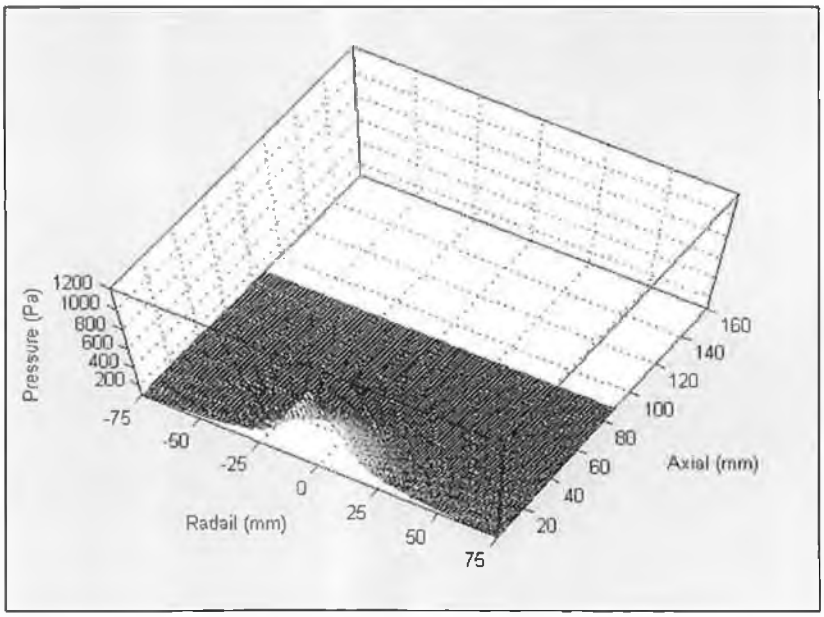

Figure 5.29: Comparison of a) the experimental distribution, as described by Makin et al [62] and b) the predicted pressure field distribution (tip displacement = 6.5μm (p-p)), in the region surrounding (>12mm) from the distal tip.

Based on the comparisons with both analytical and experimental results, the numerical acoustic fluid-structure model has shown the capability to accurately predict the pressure field around a spherical-tip. Expanding on this model, other distal shapes can be modelled, as well as the effect of using the wire waveguide in a fluid without a distal tip.

5.4.3 Fluid-structure model of wire waveguide with no distal-tip

A fluid-structure model of a 0.35 mm diameter wire waveguide with no additional distal-tip geometry was developed as shown in Figure 5.30 and Figure 5.31. The waveguide was modelled for distal-tip displacements of 11, 26, 55 and 80 μm and results for the acoustic pressures axially ahead of the tip are shown in Figure 5.32.

The predicted acoustic pressure results show that the absence of large distal-tip geometry, and therefore area of contact, results in lower pressure amplitudes in the region close to the distal-tip.

The flat distal-tip of the wire waveguide results in a more uniform pressure field in the region close to the tip and can be seen in the surface plot of the predicted acoustic pressure field in Figure 5.33.

A fluid-structure model of the 1.0 mm diameter wire waveguide without a distal-tip was also developed and the predicted pressures ahead of the distal-tip for various distal-tip displacements are shown in Figure 5.34. The results show that with a 1.0 mm diameter waveguide a distal-tip displacement of approximately 60 μm is required to generate cavitation with the cavitation threshold set at the typical value of 2.5 Watts/cm^2 [54].

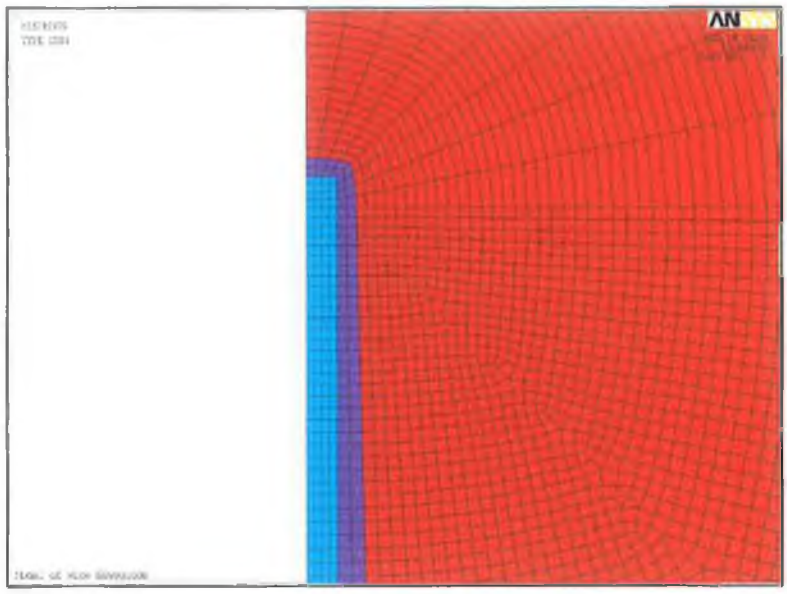

Figure 5.30: Distal section of acoustic fluid structure model of wire waveguide with flat distal-tip geometry.

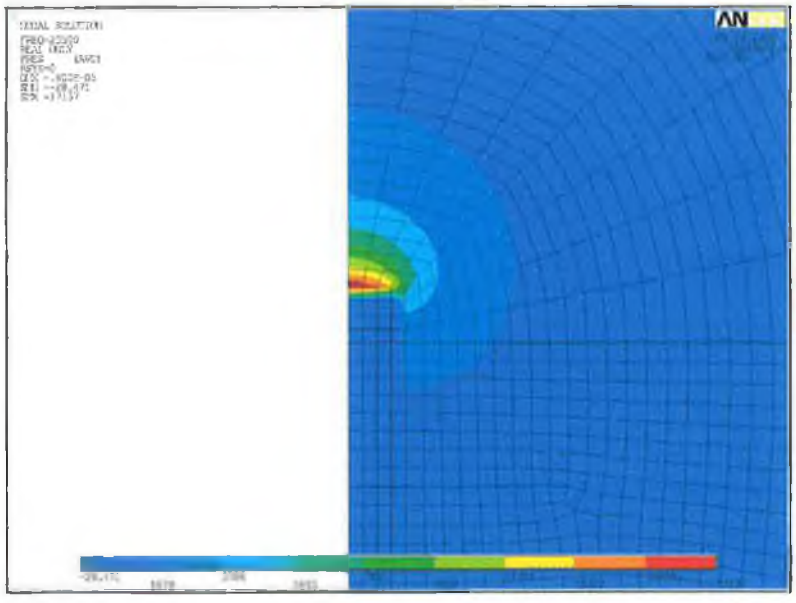

Figure 5.31: Predicted pressures (real, Pa) in region surrounding 0.35 mm diameter wire waveguide with flat distal-tip geometry (freq. = 23.5 kHz, distal-tip displacement = 11 μm).

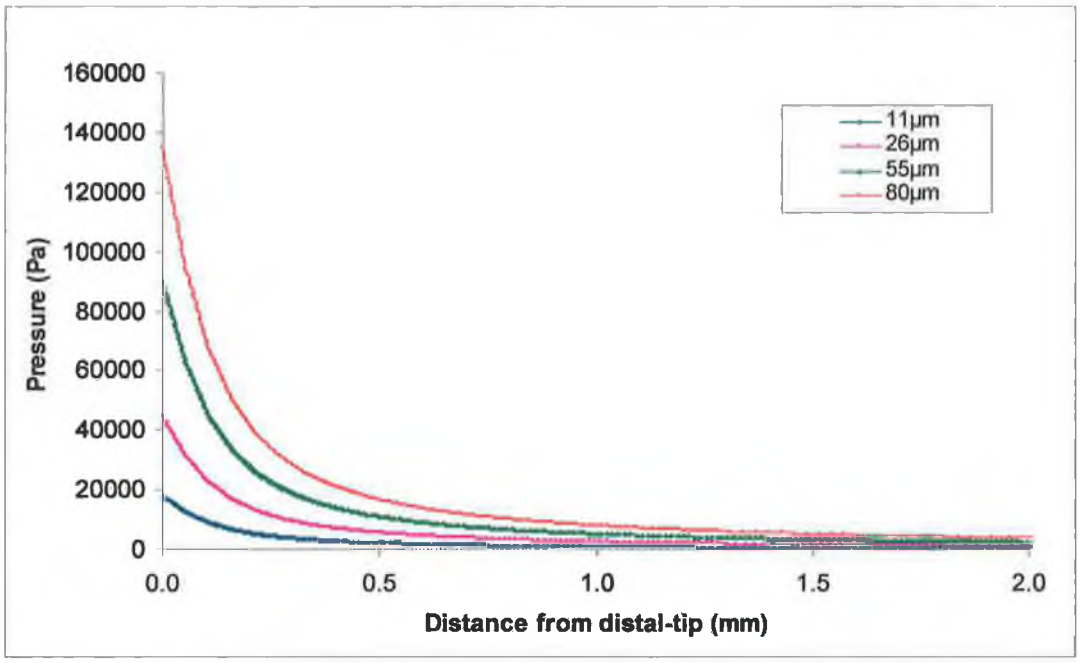

Figure 5.32: Comparison of predicted pressures along axial line for a wire waveguide (0.35 mm diameter) with flat distal-tip geometry for various distal-tip displacements at 23.5 kHz.

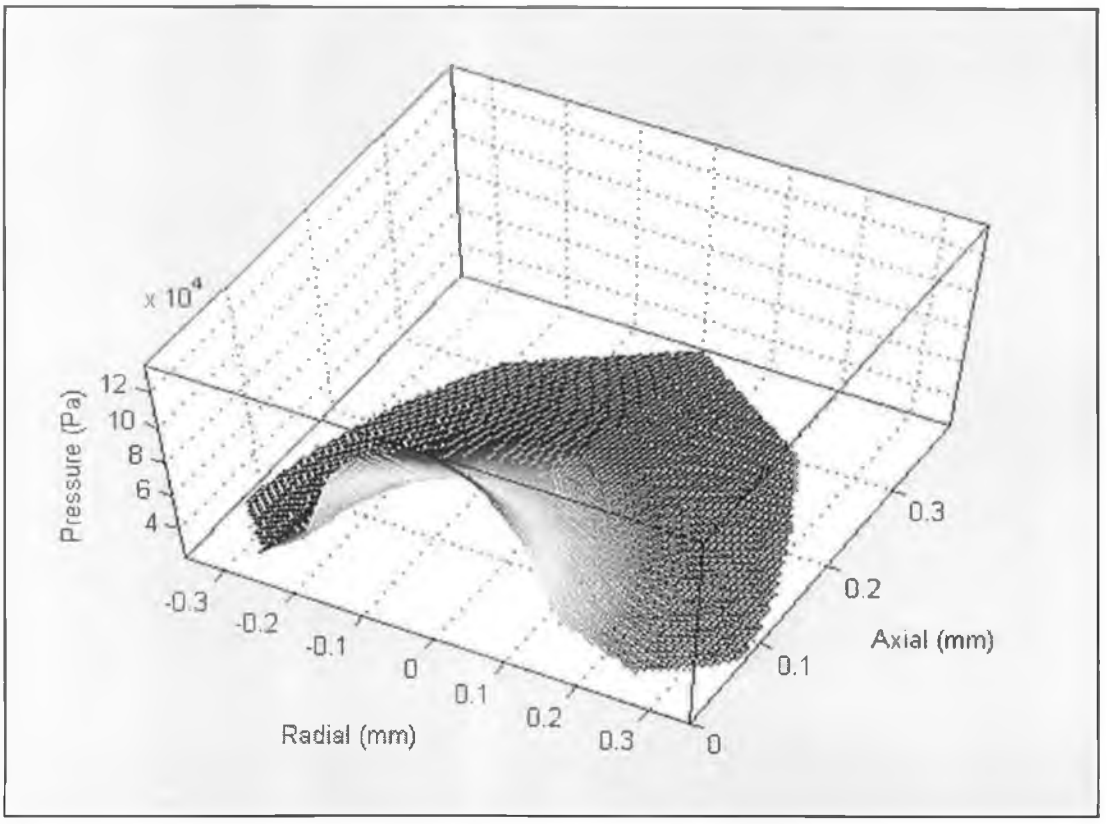

Figure 5.33: Predicted pressure field distribution (tip displacement = 80 μm (p-p)) in the region surrounding a 0.35 mm wire waveguide with no distal tip.

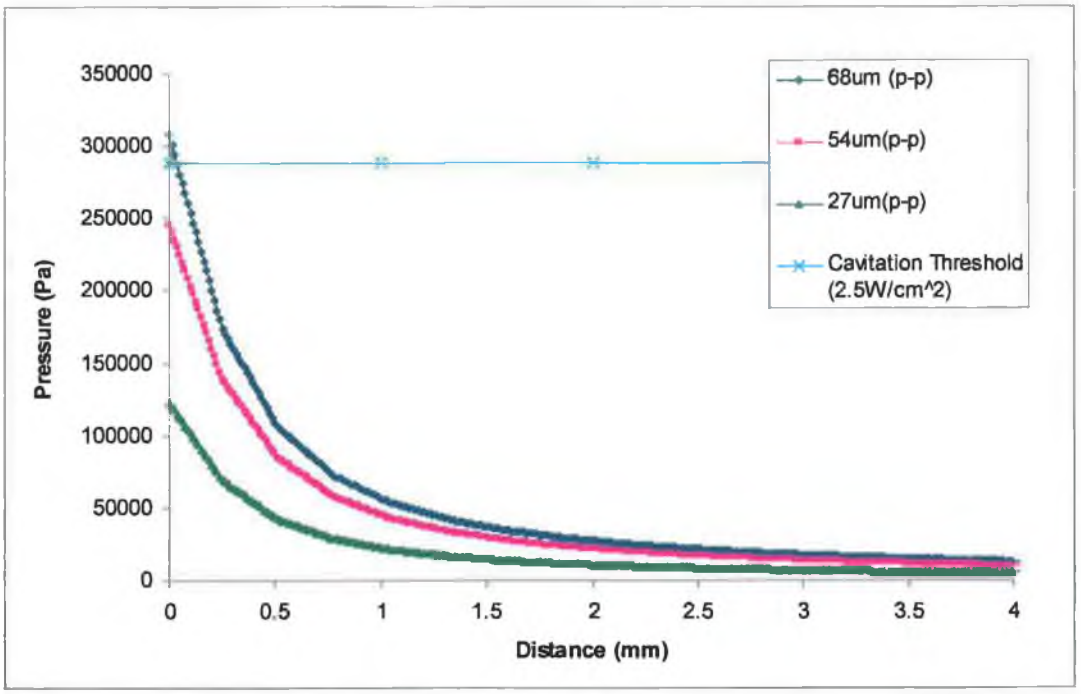

Figure 5.34: Comparison of predicted pressures along axial line for a wire waveguide (1.0 mm diameter) with flat distal-tip geometry for various distal-tip displacements at 23.5 kHz. Cavitation threshold (2.5 W/cm^2) line also shown

5.5 Summary

A numerical model of the ultrasonic wire waveguide is described that also includes distal-tip geometries and an acoustic fluid surrounding the distal-tip. This model predicts the harmonic response and the location of resonant and non-resonant lengths and, further, shows that the presence of distal-tip geometries and surrounding fluid has a negligible effect on this response.

The model has been validated against analytical results and with the inclusion of a constant damping value of 4.5% for the waveguide the model has been validated against the experimental measurements of distal-tip displacements over the range of lengths tested. The model also predicts the standing wave structure, measured experimentally, with a series of displacement minima and maxima along the length of the waveguide. This model further validates the input displacements and frequencies that were estimated based on experimental measurements.

The model can also determine stresses at any location along the length of the wire waveguide and predicts that near resonant length the stress at the proximal end is higher, consistent with operating conditions which cause the apparatus (converter and horn) to stall.

This acoustic model has been validated against analytical solutions for an oscillating sphere and experimental measurements of the acoustic pressures in the field surrounding a spherical-tip described by Makin and Everbach [62]. The acoustic fluid results of the model predict pressures sufficient to cause cavitation, for the distal-tip displacements and frequency modelled.

The validated acoustic fluid structure model of the wire waveguide can be used in the further modelling of various distal-tip geometries, wire lengths and surrounding fluids in the prediction of pressures amplitudes in the acoustic pressure field and operating parameters to cause cavitation.

Chapter 6

Experimental Testing of the Ultrasonic Wire Waveguide Apparatus

6.1 Introduction

Bench testing of the ultrasonic wire waveguide apparatus on model materials chosen for their properties which are similar or stiffer to rigid calcified biological material is described in this chapter.

Two wire waveguides will be used in the testing. The first will be a standard 1.0 mm diameter wire waveguide as described in Chapter 3. The second, however, is a tapered NiTi wire waveguide designed as part of this work that allows ultrasonic displacements to be delivered to a 0.35 mm wire waveguide with improved reliability.

In addition, both these waveguides are to be tested in water at ambient temperature in order to identify distal-tip displacements that cause cavitation and will be compared with the numerically predicted displacements in Chapter 5.

The presence of acoustic streaming will also be identified for various distal-tip peak-to-peak displacements for both wire waveguides.

6.2 Tapered Wire Waveguide

A NiTi wire waveguide with a 1.0 mm diameter proximal section and tapering to a 0.35 mm diameter distal section was designed as shown in Figure 6.1. The wire was manufactured by Precision Wire Components (10230 SW Spokane Ct., Tualatin, Oregon, USA) from the same grade of NiTi wire as discussed in Chapter 3.

This tapered wire waveguide was designed to have the bending stiffness and increased diameter to allow for connection to the radiating face of the acoustic horn, via the axial set screw connection method, yet have sufficient flexibility and dimensions in the distal section, similar to standard guidewires. The length of the tapered wire was 310 mm.

Both wire waveguides, the 1.0 mm diameter and 0.35 mm diameter tapered, were tested under the optical microscope to determine distal-tip displacements over a range of input power dial-settings.

The distal-tip displacements for the 1.0mm diameter wire waveguide of 288mm length for multiple input power dial settings is shown in Figure 6.2. This is similar to data reported in Chapter 4, but higher input power dial-settings are included here.

No measurements of the distal-tip displacements for the 0.35 mm tapered wire waveguide could be obtained. This was due to transverse vibrations (whipping) that resulted in blurred images being obtained. An image of the 0.35 mm diameter tapered wire waveguide, both, in its stationary position and energised, is shown in Figure 6.3. This motion is similar to that described by Makin and Everbach [62] and a point cannot be focused upon during operation even when contained in a 0.4 mm inner diameter catheter.

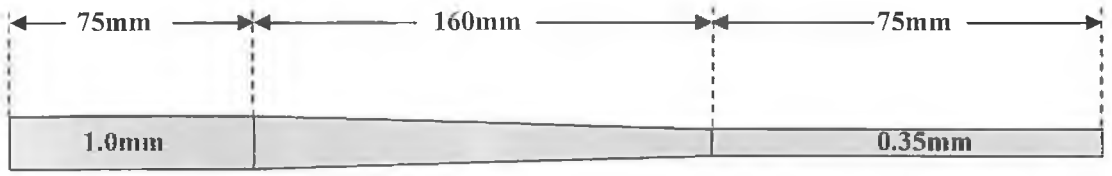

Figure 6.1: Diagram of 0.35 mm tapered wire waveguide

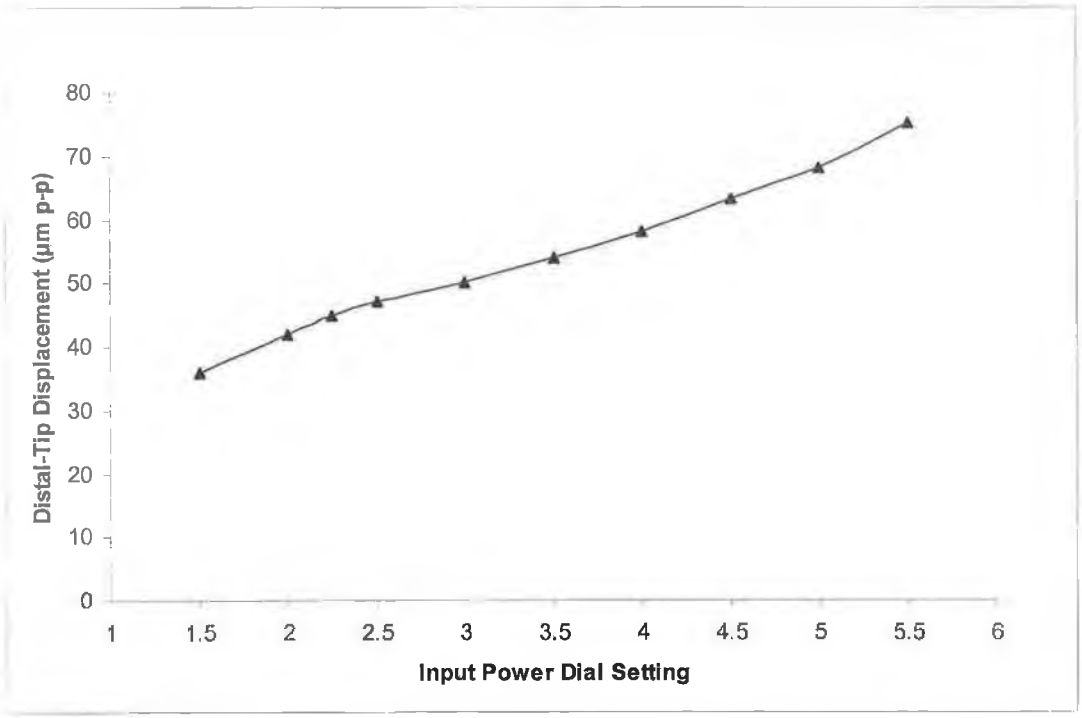

Figure 6.2: Distal-tip displacements for a 1.0 mm diameter wire waveguide of length 288 mm for multiple input power dial-settings

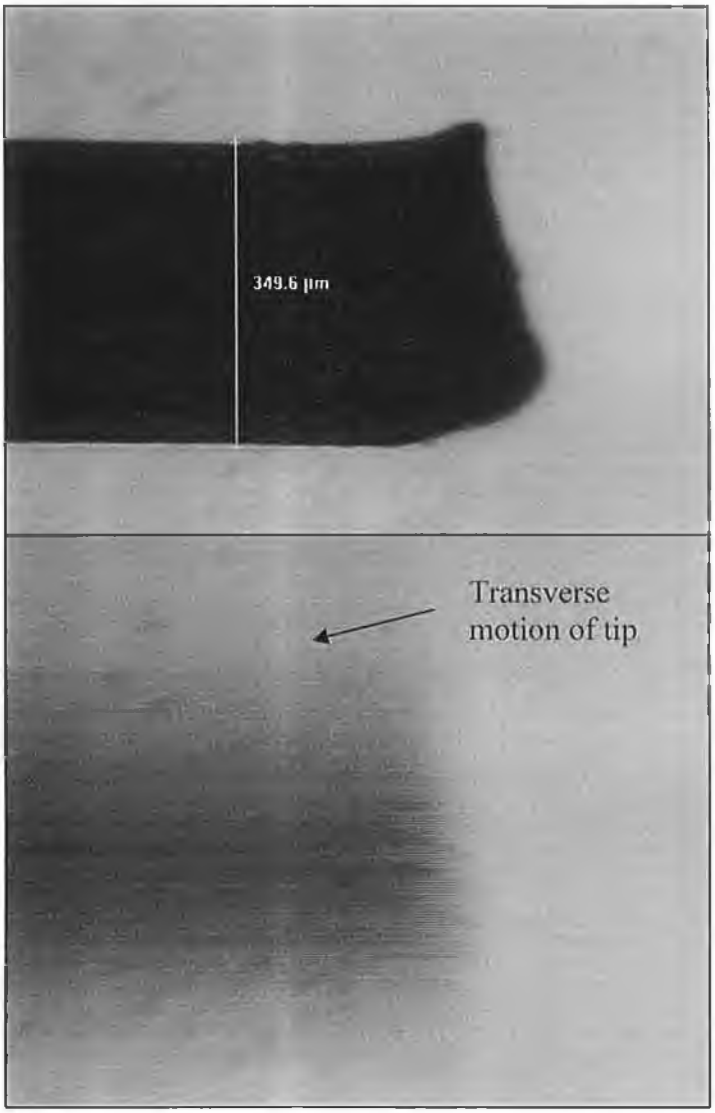

Figure 6.3: Image of stationary and vibrating 0.35 mm tapered wire waveguide distal tip with a calibrated objective lens magnification factor of 8

6.3 Model Materials

Calcium based materials such as calcium carbonate (blackboard chalk), calcium sulphate and calcium hydroxyapatite have been suggested as potential model materials to represent calcified biological material such as renal calculi and other biological calcifications [78]. Silicone rubbers, agar and gelatin and polyvinyl alcohol (PVA) hydrogels can be used as model materials for the healthy arterial wall [78, 79 (cited in [6])].

In this work calcium carbonate and calcium hydroxide will be used as model material for the calcified plaque. The calcified model materials were tested to establish important mechanical properties prior to bench testing.

Billets of calcium hydroxide were manufactured by researchers at the Ceramics Research Group in Dublin City University by compressing $Ca(OH)_2$ powder in a billet die under loads of 20, 40 and 50 kN [80] . Calcium carbonate (extruded chalk) billets were obtained and samples of the material types are shown Figure 6.4. These billets were subjected to compression tests to failure, similar to tests conducted by Topoleski and Salunke [6, 20]. Both Rockwell B and Rockwell C hardness testing failed as samples shattered under the applied loads.

Compression tests to failure were performed using the Hounsfield H20K-W testing machine with a crosshead speed of 2 mm/min. The results of the compression tests are shown in Figure 6.5. The calcium hydroxide specimens showed considerably stiffer behaviour when compared with the calcium carbonate specimens with the 50 kN sample showing the stiffest overall response.

Figure 6.6 shows the response of the calcium carbonate specimens which show an approximate linear response to failure. Included are linear best-fit trendlines which give an approximate Young's modulus value for the two samples of 60 MPa and 70 MPa.

These calcified based model materials have a stiffer response when compared with compression tests conducted on actual calcified plaque by Topoleski and Salunke [6, 20], see Figure 2.3 (page 14), and higher ultimate failure strengths of between approximately 4 and 16 MPa.

The estimated Young's modulus values for the calcium carbonate samples are within the wide range of reported values used in the modelling of calcified materials from 1 to 1000 MPa [81, 82 (cited in 6), 49, 83].

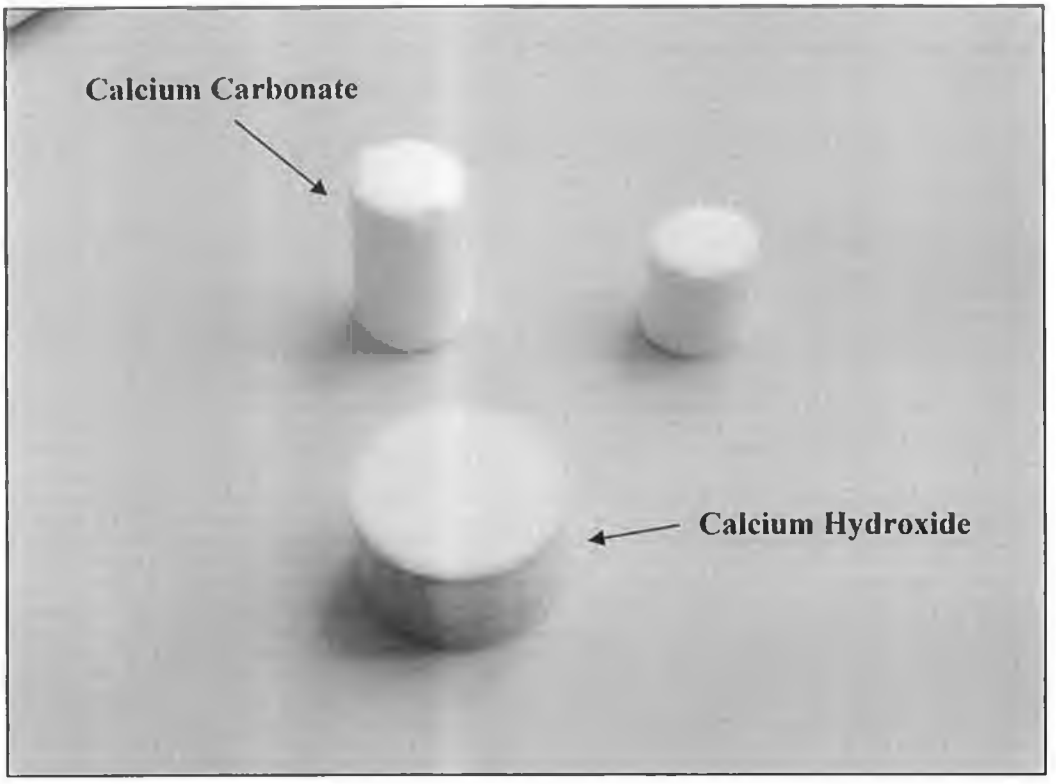

Figure 6.4: Billets of calcium carbonate and calcium hydroxide

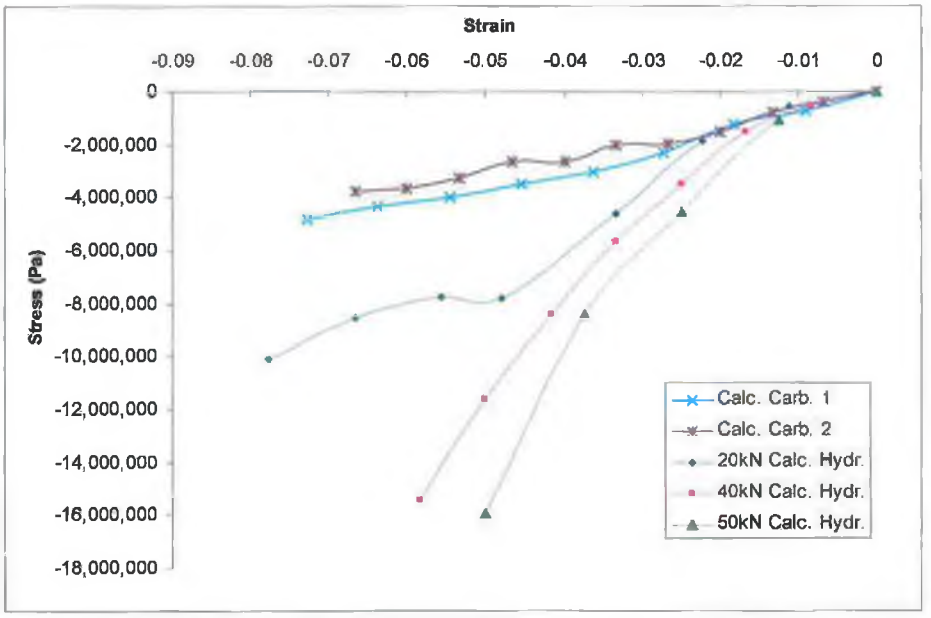

Figure 6.5: Results of compression tests on billets of calcium carbonate (n=2) and compressed calcium hydroxide (20, 40 and 50kN)

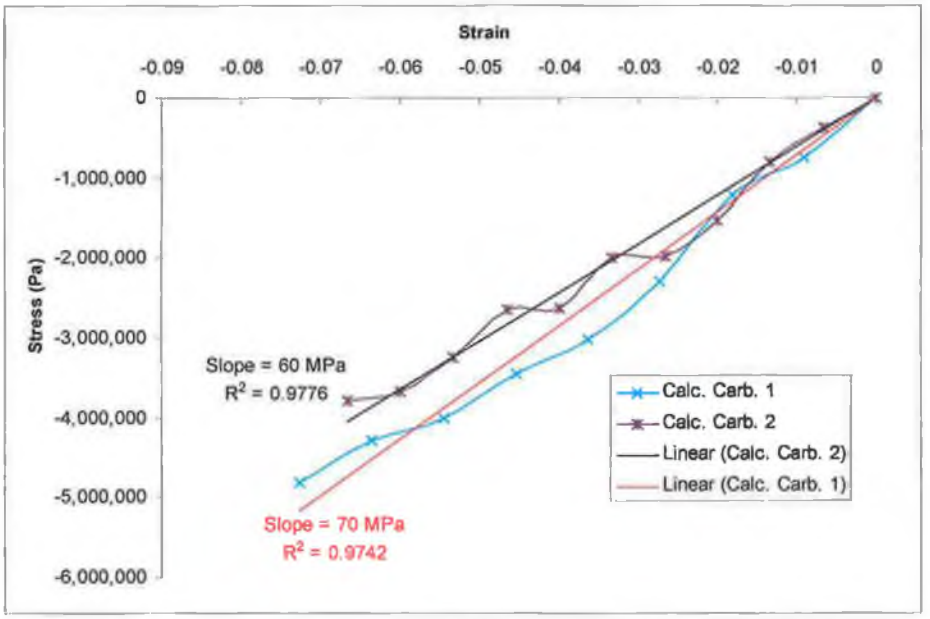

Figure 6.6: Compression results from calcium carbonate billets with fitted linear trendlines

6.4 Testing Ultrasonic Wire Waveguide Apparatus on Model Materials

The material samples of the calcium carbonate and the various types of compressed calcium hydroxide were ablated with the ultrasonic wire waveguide apparatus, described in Chapter 3, for various input power dial settings.

In order to control the direct ablation conducted on the various samples, a test rig was developed that could apply a constant force the wire waveguide apparatus applied on the sample. This rig, shown in Figure 6.7 and Figure 6.8, consists of a steel table that holds a slider unit adapted from a static friction test-rig. This slider held the specimen and the force the specimen applied on the tip was kept constant by hanging various weights (*Fa)* off the hanger. The applied feed force (*Fc*) the specimen applied on the tip was calculated from:

$$Fc = (Fa + weight\ of\ hanger) - Fr$$

where *Fr* is the static frictional force between the table and slider, calculated prior to testing to be 0.5 N. For each specimen tested, the material ablation feed rate was measured and presented in mm/min. Tests were conducted for multiple input power dial settings and applied forces.

Figure 6.9 and Figure 6.10 show the material ablation feed rates for the calcium hydroxide and calcium carbonate specimens, respectively, for an applied feed force (*Fc*) of 1 N. Figure 6.11 and Figure 6.12 show the material ablation feed rates for an applied force of 2 N.

The material ablation feed rate for the calcium carbonate specimen was considerably higher than each of the calcium hydroxide specimens. At an input power dial-setting of 3.5 the material ablation feed rate for the calcium carbonate sample was 282 mm/min versus 5.1 mm/min for the 50 kN compressed calcium hydroxide.

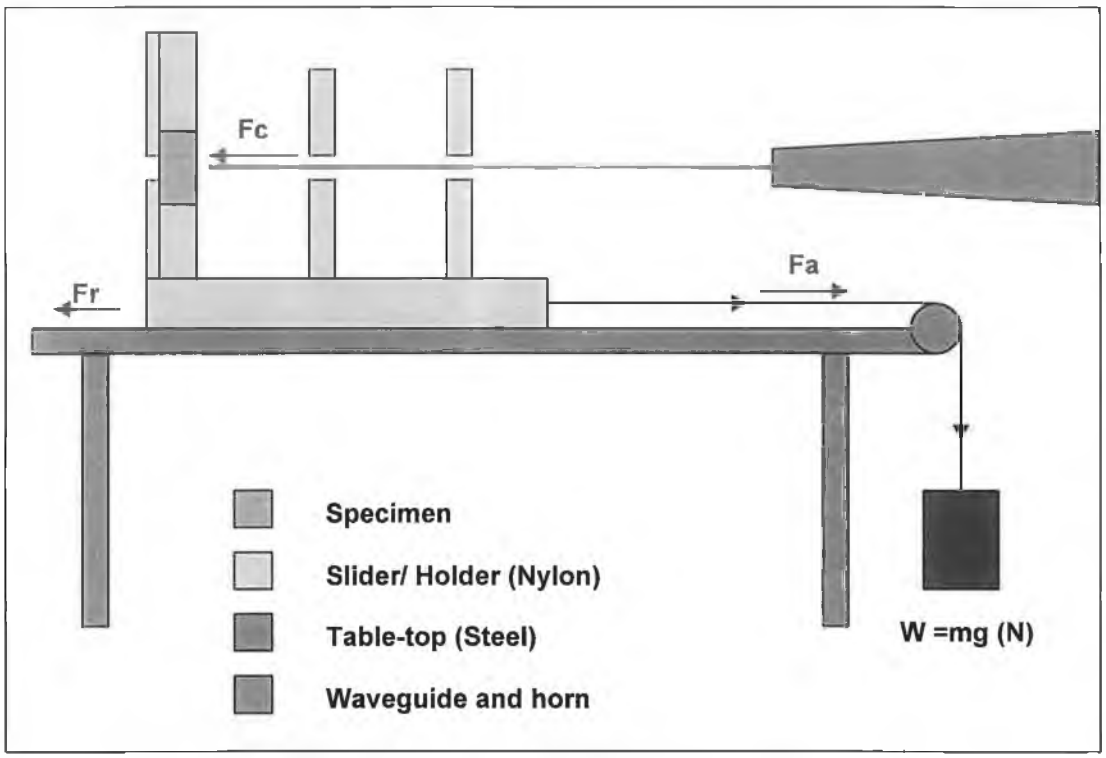

Figure 6.7: Diagram of direct ablation testing rig

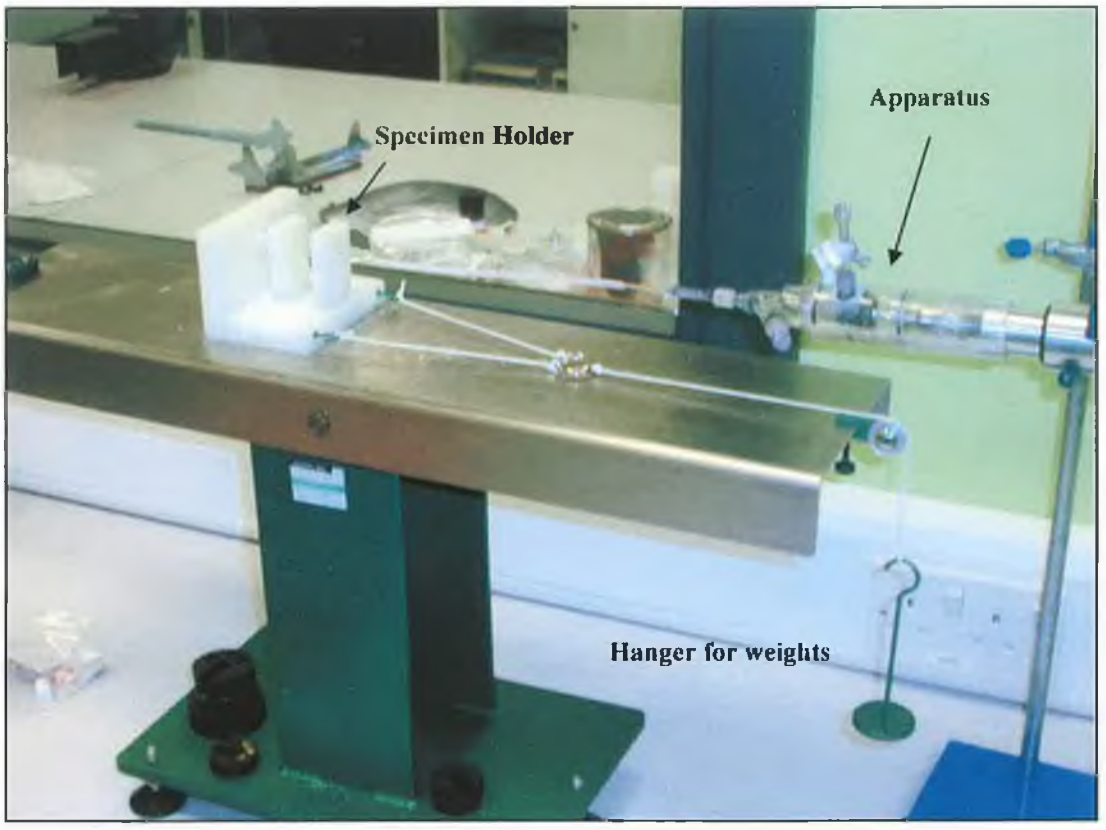

Figure 6.8: Adapted static friction tester used in bench testing of ultrasonic wire waveguide apparatus in determining material removal rates for various specimens

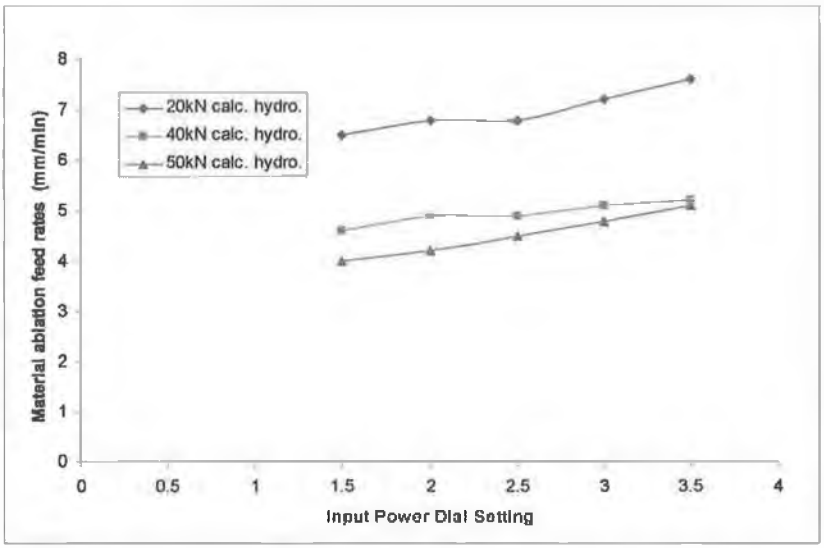

Figure 6.9: Results of direct ablation on the 20, 40 and 50 kN compressed calcium hydroxide samples for a 0.35 mm tapered wire waveguide and an applied feed force of 1 N.

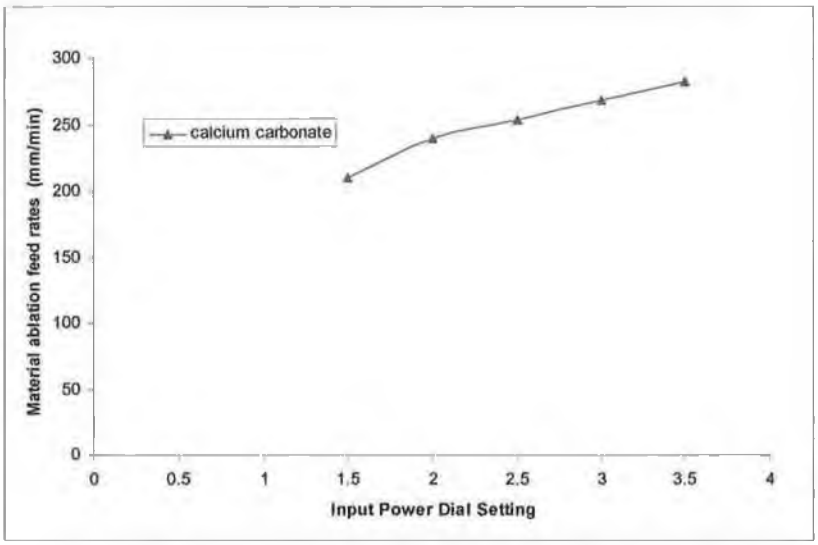

Figure 6.10: Results of direct ablation on the calcium carbonate for a 0.35 mm tapered wire waveguide and an applied feed force of 1 N.

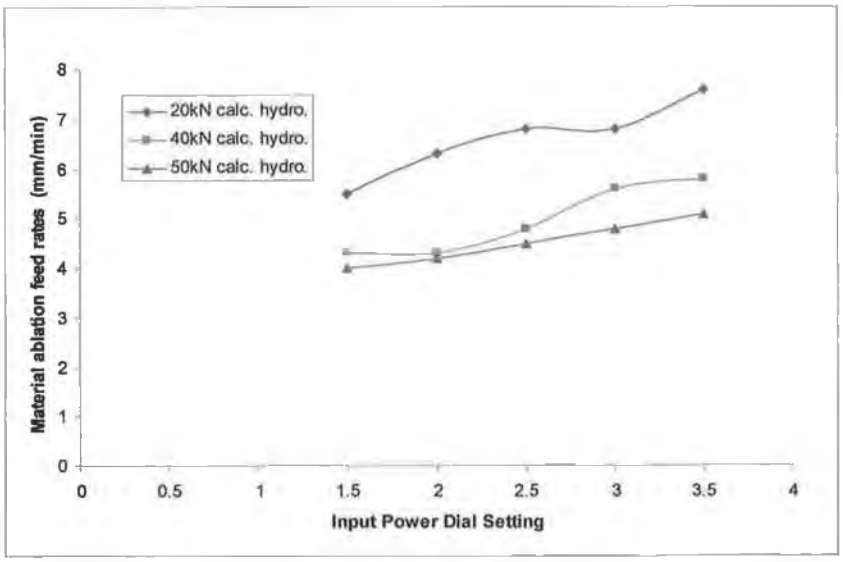

Figure 6.11: Results of direct ablation on the 20, 40 and 50 kN compressed calcium hydroxide samples for a 0.35 mm tapered wire waveguide and an applied feed force of 2 N.

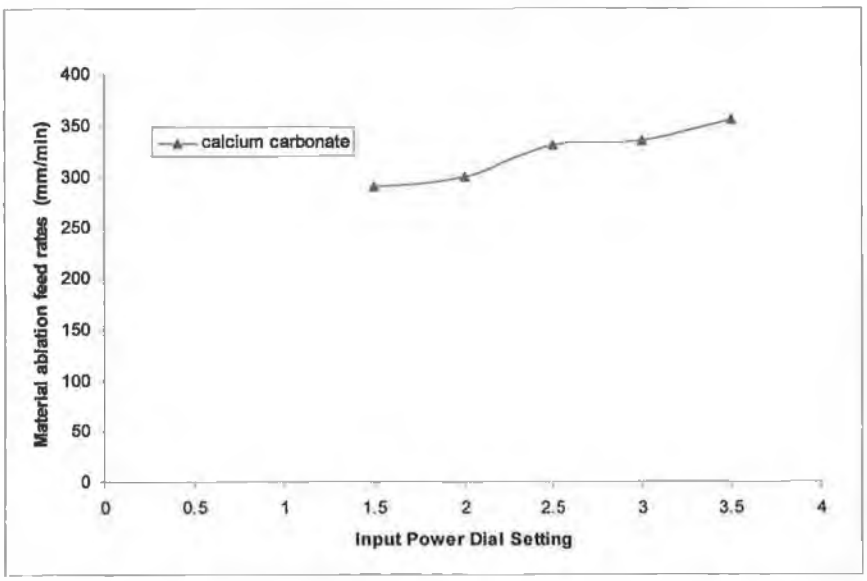

Figure 6.12: Results of direct ablation on the calcium carbonate for a 0.35mm tapered wire waveguide and an applied feed force of 2 N.

Figure 6.13 shows an image of a calcium carbonate specimen after administration of ultrasound. The image shows a hole drilled through the 15mm long specimen with the 0.35mm tapered wire waveguide, also shown.

Figure 6.14 shows an image of a 20 kN compressed calcium hydroxide specimen following drilling using the 0.35mm tapered wire waveguide. In general, direct ablation with the 0.35 mm tapered wire waveguide resulted in a hole drilled through the sample. The sample remained intact, although radial cracks are seen propagating out from the centre as in Figure 6.14.

Direct ablation with the 1.0 mm wire waveguide yielded similar results on the calcium carbonate sample but shattered all the calcium hydroxide specimens as shown in Figure 6.15.

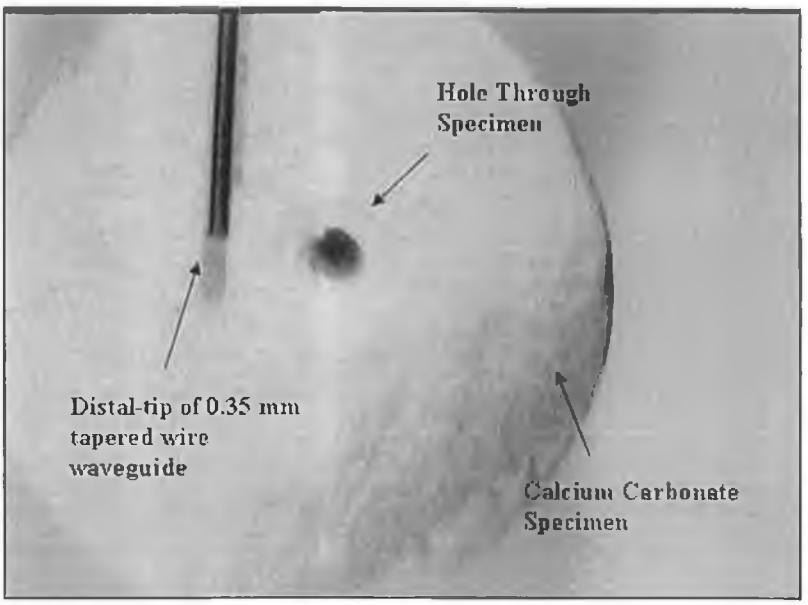

Figure 6.13: Image of calcium carbonate specimen with hole drilled through with 0.35 mm diameter tapered wire waveguide, also shown.

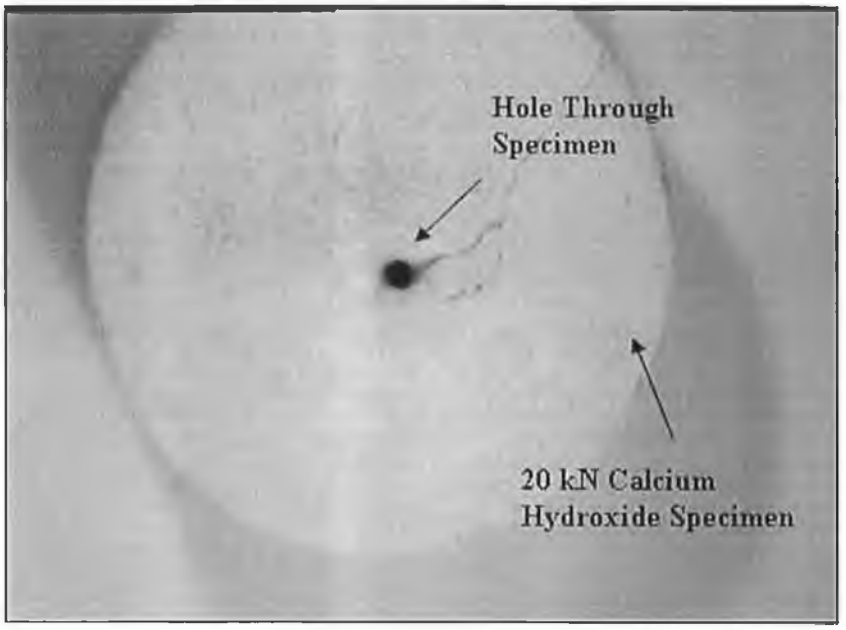

Figure 6.14: Image of 20 kN calcium hydroxide specimen with hole drilled through with 0.35 mm diameter tapered wire waveguide.

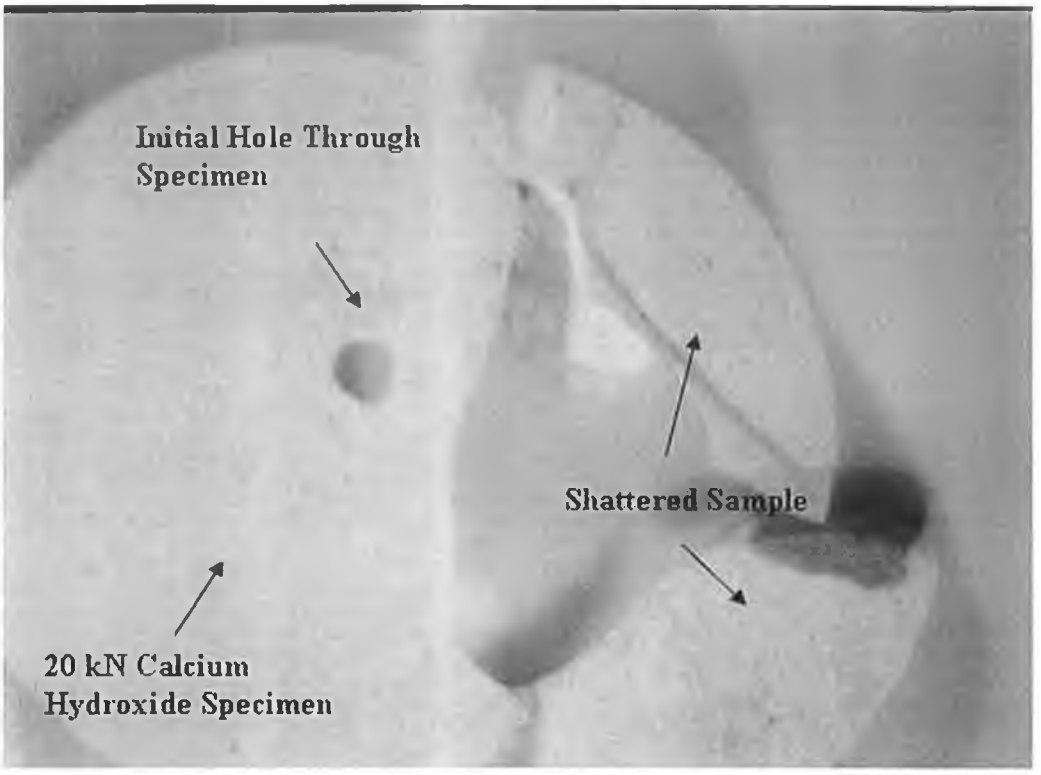

Figure 6.15: Image of 20 kN calcium hydroxide specimen with hole drilled through with 1.0 mm diameter wire waveguide.

6.5 Ultrasonic Wire Waveguide in Fluid

Both the 1.0mm and 0.35mm diameter tapered wire waveguides were tested in water at room temperature to observe fluid disturbance in the region surrounding the distal-tip. These experimental observations were conducted for various input power dial settings.

6.5.1 Cavitation

The distal-tip of both the 1.0 mm diameter and 0.35 mm diameter tapered wire waveguides were placed in a Petri dish filled with water at ambient temperature. For various input power dial-settings between 1.5 and 6.5, images of the fluid surrounding the distal-tip were captured using a microscope (MEIJI™ EMZ-TR) with video capture capability (Videolabs™ Illumabase).

The transverse motion of the 0.35 mm diameter tapered wire waveguide prevented images near to the distal-tip being obtained. With the 1.0 mm wire waveguide, however, images were obtained for the entire input power dial-setting range.

Figure 6.16 shows the images obtained with the 1.0 mm wire waveguide. The images show that at the input power dial-setting of 4.5, a cavitation region, identified by cloudiness in the water close to the tip, a change in noise produced and overall disturbance of the fluid [58], is observed. With a further increase in the input power dial-setting this region increases further and is accompanied by a greater fluid disturbance.

The input power dial-setting of 4.5 required to cause cavitation correlates to a distal-tip displacement of 62 μm, as shown Figure 6.2. This compares favourably with the distal-tip displacement (p-p), of approximately 60 μm, predicted by the fluid-structure numerical model of the 1.0 mm diameter waveguide in Chapter 5, for a commonly used cavitation threshold of 2.5 Watts/cm^2.

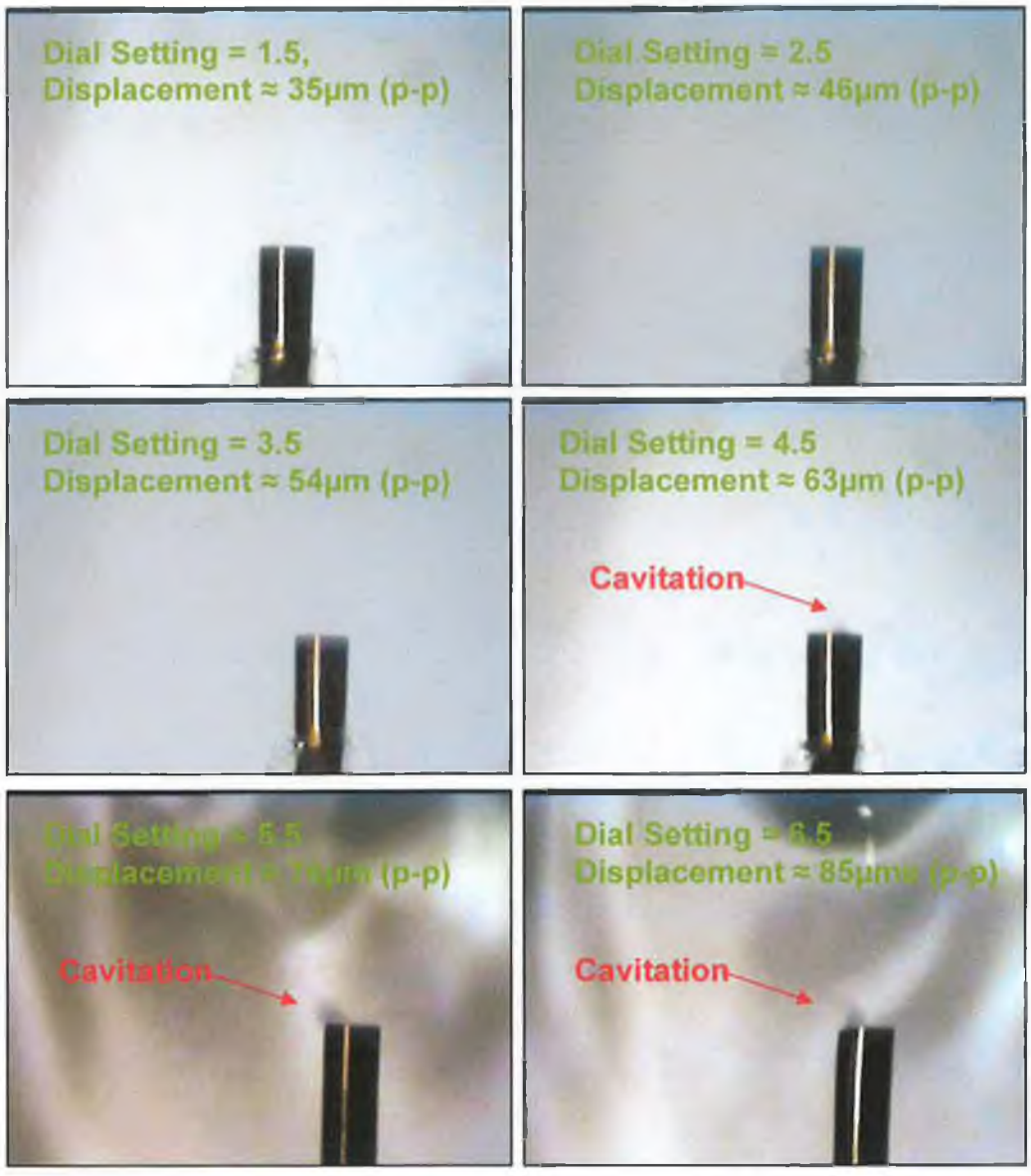

Figure 6.16: Images of the distal-tip of the 1.0 mm diameter wire waveguide in water at ambient temperature for various input power dial-settings between 1.5 and 6.5. The displacement for a dial setting of 6.5 is estimated based on observed trend in Figure 6.2

6.5.2 Acoustic Streaming

In addition to the cavitation caused around the distal-tip, a fluid motion due to acoustic streaming was also identified. In order to observe this acoustic streaming pattern seeding particles (Polyamid Seeding Particles, 50 μm, Dantec Dynamics), normally used in Particle Image Velocimetry (PIV), were placed in the water. These were chosen as they have similar density to water and as a result have a minimal effect on the fluid motion.

Figure 6.17 shows images of the acoustic streaming around the distal-tip of the 1.0 mm diameter wire waveguide for various input power dial-settings. The images show a streaming laminar flow away from the distal-tip and the velocity of this flow was qualitatively observed to increase with increasing input power.

Of particular interest is how this flow changes above the cavitation threshold to a turbulent flow with a noticeable increase in fluid disturbance in an increased region around the vibrating distal-tip. The region of cavitation close to the tip is once again visible.

Figure 6.18 shows an image of enlarged region around the distal-tip of the 0.35 mm diameter wire waveguide and the fluid flow due to acoustic streaming and shows a response similar to the acoustic streaming pattern around a small vibrating sphere, in Figure 2.6.

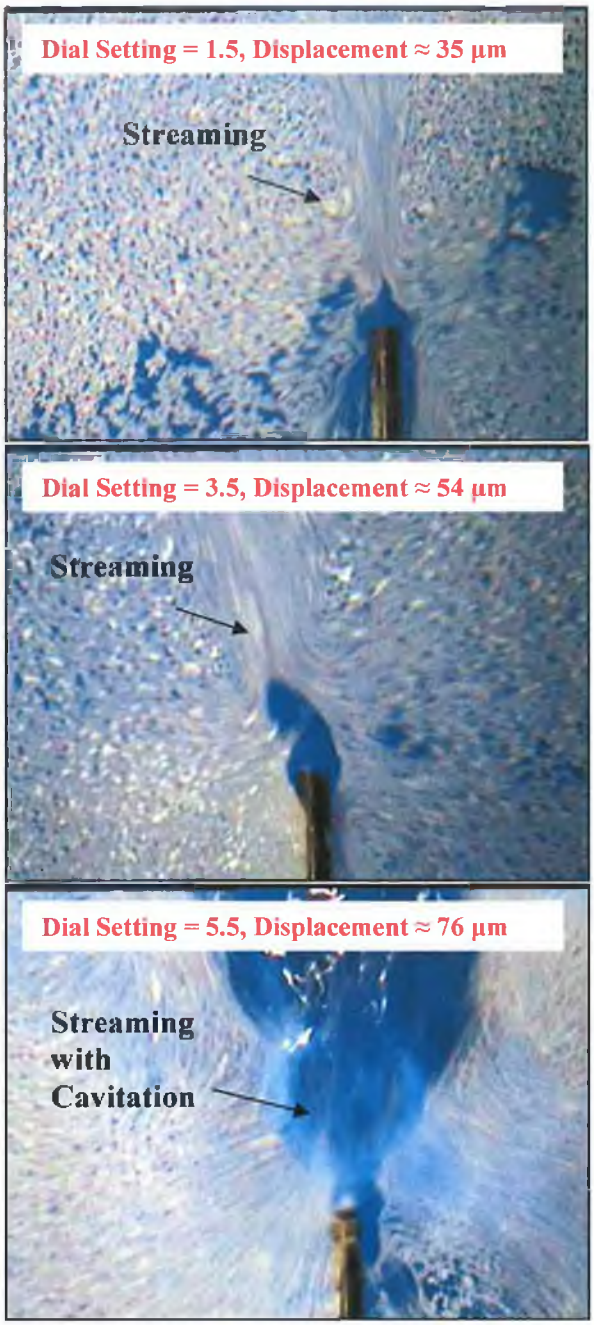

Figure 6.17: Images of acoustic streaming around the distal-tip of the 1.0 mm diameter wire waveguide for various input power dial-settings.

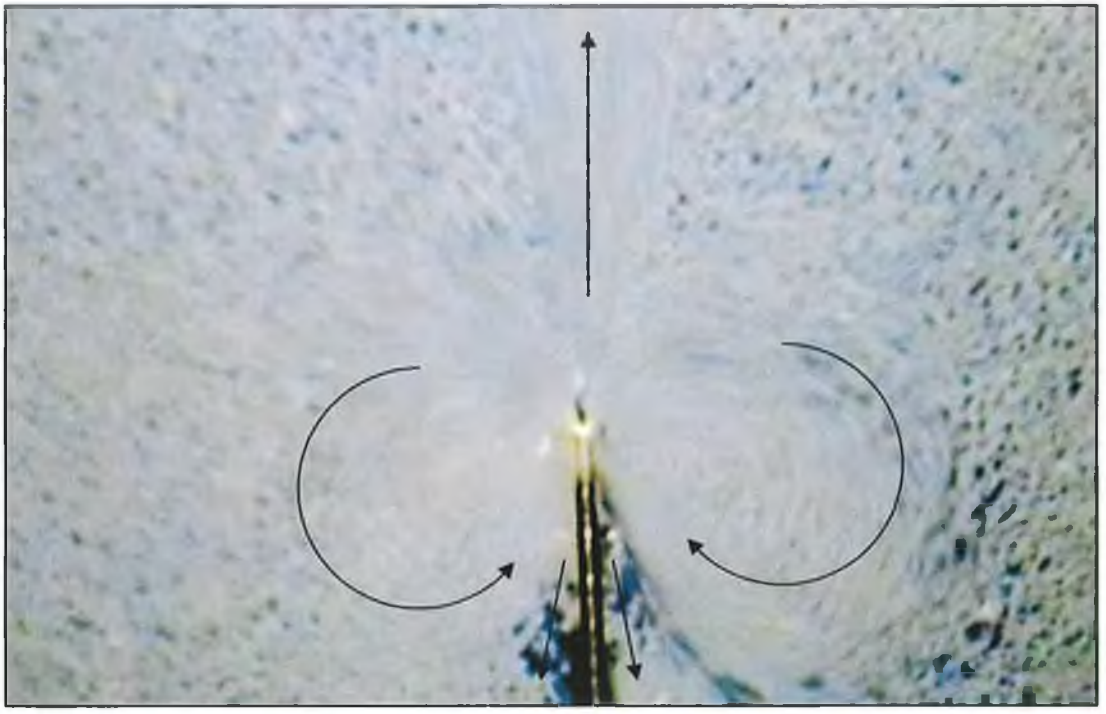

Figure 6.18: Images of acoustic streaming around the distal-tip of the 0.35 mm diameter tapered wire waveguide for an input power dial-setting of 2.5. Arrows indicate general direction of observed fluid motion.

6.6 Summary

The ultrasonic (23.5kHz) displacements a the distal-tip of both the 1.0 mm and 0.35 mm tapered wire waveguide has been shown to ablate calcium carbonate and calcium hydroxide specimens. These specimens have a stiffer response in compression than those reported for calcified plaques in the literature.

The results of ablation on the samples show that with the material ablation feed rate increased with increasing distal-tip displacements and applied force. The removal rates were higher for the 0.35 mm diameter tapered wire waveguide.

Cavitation was observed in the region close to the distal-tip of the 1.0 mm diameter wire waveguide for distal-tip displacements greater than 62 μm and closely matches the predicted displacements and pressures from the numerical model.

Acoustic streaming was observed in the regions around both the 0.35 mm diameter tapered wire waveguide and the 1.0 mm diameter waveguide for all input power dial-settings. This flow was observed to laminar below the displacements required to cause cavitation and the velocity was qualitatively observed to increase with increasing input power.

Above the cavitation threshold this flow was observed to be turbulent and occurred in a large region ahead of the distal-tip of the wire waveguide.

Chapter 7

Conclusions and Future Work

7.1 Conclusions from this Work

With market approvals for the use of therapeutic ultrasound delivered via wire waveguides in the treatment of cardiovascular plaques imminent the evidence in this thesis has shown:

- A validated coupled fluid-structure model of the wire waveguide and the fluid surrounding the distal-tip has been developed. This model predicts wire waveguide behaviour in the ultrasonic frequency range of interest and can be used to model the effects of various frequencies and displacements on the performance of the wire waveguide, including stresses, important in predicting when failure will occur.

- The model predicts the pressures developed in the field surrounding the distal-tip and has been shown to be capable of predicting when cavitation will occur. This is important in cardiovascular surgery as ablation of plaque material is only observed above the cavitation threshold. This model can be used to further improve wire waveguide and distal-tip designs and investigate the effects of various frequencies and displacements.

- A design methodology for the development of Therapeutic Ultrasound Angioplasty devices has been shown. This work describes a reliable axial-screw wire waveguide connection method and the benefits of operating the

waveguide at or near non-resonant lengths, including reduced stress in the wire waveguide and greater control of distal-tip displacements. These are both important considerations during surgical application. In addition, it is recommended that the wire waveguide be operated at a length slightly greater than a non-resonant length. This will allow for increased distal-tip displacement due to the effects of resonance and yet any increased force on the distal-tip would result in the distal displacement response drifting back to the more controllable non-resonant point.

7.2 Summary of Results

- A therapeutic ultrasound wire waveguide apparatus, consisting of a piezoelectric converter, acoustic horn and NiTi wire waveguide, developed as part of this work, delivers ultrasonic displacements down small diameter wire waveguides.

- An axial set-screw connection method, as described in Chapter 3, was found to be the most reliable way to couple the NiTi wire waveguide to the radiating face of the acoustic horn. Using this method 1.0mm diameter wires transmit ultrasonic displacements for at least 300 seconds without failure.

- The 1.0 mm diameter wire waveguide has the greatest time-to -failure when compared with the 0.6 mm and 0.35 mm wire waveguides for the axial set screw connection method. It is hypothesised that the 0.6 mm and 0.35 mm diameter wire waveguides, which are more suited to cardiovascular surgery, suffer more crimp damage as a percentage of cross sectional area and in conjunction with the observed transverse vibration at the connection point fail in a time period of less than 100 seconds.

- The use of a tapered wire waveguide with a 1.0 mm diameter proximal section and tapering to a 0.35 mm diameter distal section was shown to increase reliability relative to a uniform 0.35 mm diameter wire waveguide.

- Peak-to-peak displacements measurements at the distal-tip of the 1.0 mm wire waveguide, by the optical microscope method, show that wire waveguide length is critical, as at lengths close to resonant lengths the distal-tip displacements increase considerably. A maximum distal-tip displacement, with efficient ultrasound delivery, of 85 μm was measured.

- Non-resonant lengths were experimentally determined to occur at lengths of 146, 218 and 288 mm for the range of lengths tested. These lengths were compared with the analytically determined non-resonant lengths for uniform vibrating rod and the frequency of operation of the apparatus is determined to be 23.5 kHz.

- By observing the non-resonant displacements and extrapolating the data back to a zero waveguide length, as discussed in Chapter 4, the input displacements applied to the proximal end of the wire waveguide were estimated. For input power dial-settings of 1.5, 2, 2.25 and 2.5 the applied displacements to the proximal end of the wire waveguide are 32, 41, 44.5 and 46 μm, respectively.

- A standing wave structure along the length of the wire waveguide was experimentally determined. This standing wave consists of a series of displacement maxima and minima along the length of the waveguide and, due to the presence of damping in the waveguide material, differs from the analytically determined standing wave with a series of displacement nodes and anti-nodes.

- The results from the experimental measurements of the wire waveguide apparatus and, in particular, the frequency of operation of the apparatus and the input displacements for various input power dial settings are used in the numerical modelling of the wire waveguide.

- A mesh density of (2 × 606) was shown to capture all the resonant frequencies in the range of interest for the model of the 1.0 mm diameter wire waveguide and yet maintain an aspect ratio of 2. Similarly, mesh densities of (2 × 909) and (2 × 1212) were used for the 0.6 mm and 0.35 mm wire waveguides, respectively.

- The results from the modal analysis of the wire waveguides show that the resonant frequencies in the range of interest are determined for all wire waveguides compared with the analytical solution of resonant frequencies in a uniform rod.

- Using these mesh density values for the wire waveguides the harmonic response analysis of the wire waveguides performed, predicts the peak-to-peak displacements and lengths where resonance occurs, with the inclusion of a constant damping value of 4.5%, and closely matches the experimentally determined results.

- Results from the harmonic response analysis also predict the internal standing wave structure with a series of displacement minima and maxima and compare closely to the measurements of the experimental performance characteristics of the wire waveguide apparatus. In addition, the model predicts stresses at all points along the length of the wire waveguide and shows that near resonant lengths the force the wire waveguide applies to the distal-tip of the acoustic horn increases. This increase in force appears to cause the acoustic horn to stall and is consistent with observations made when operating the apparatus close to wire waveguide resonant lengths.

- Operating the wire waveguide near or at a non-resonant length will reduce stresses at, both, the connection point and along the length of the waveguide.

- The inclusion of a distal ball-tip in the harmonic model of the wire waveguide, similar to experimental devices reported in the literature, was shown to have only a minor effect on the predicted resonant response of the wire waveguide. This model forms the structural basis of the coupled fluid - structure model of the wire waveguide and surrounding fluid.

- The coupled fluid-structure model of the wire waveguide and fluid surrounding the distal-tip shows that the presence of the fluid has only a negligible affect on the resonant response of the wire waveguide for the range of distal-tips modelled, similar to those reported in the literature.

- The fluid-structure model predicts the pressure field developed around the distal-tip of the wire waveguide and shows the increasing ball-tip diameter or distal-tip displacement increases the pressure amplitudes.

- These predicted pressure amplitudes show good comparison with the experimentally determined pressures for a model of an experimental device described by Makin and Everbach [62] and predicts pressures sufficiently high to cause the cavitation observed by the authors.

- The validated fluid structure model was used to predict the distal-tip displacements required to cause cavitation for the ultrasonic wire waveguide apparatus described as part of this work with a 1.0 mm diameter wire waveguide. A distal-tip displacement of 60 μm was predicted with a cavitation threshold intensity of 2.5 Watts/ cm^2 (similar to values reported in the literature).

- The ultrasonic wire waveguide apparatus with, both, the 1.0 mm diameter wire waveguide and 0.35 mm diameter tapered waveguide, was shown to be capable of drilling through calcium carbonate and compressed calcium hydroxide specimens. These model materials were chosen as they had a response similar to or stiffer than calcified plaque material properties reported in the literature. This direct ablation showed that material ablation feed rates for the calcium carbonate specimens were as high as 250 mm/min. Although for the stiffer calcium hydroxide material ablation feed rates up to 7 mm/min were determined.

- The ultrasonic wire waveguide apparatus with the 1.0 mm diameter wire waveguide was shown to generate cavitation in water at ambient temperature above a distal-tip displacement of 62 μm and compares closely with the numerical model that predicted 60 μm with a cavitation threshold intensity of 2.5 Watts/ cm^2, similar to values reported in the literature.

- Acoustic streaming was observed in the region surrounding the distal-tip of, both, the 1.0 mm diameter wire waveguide and 0.35 mm diameter tapered waveguide. The streaming velocity increased with input power but became turbulent above the cavitation threshold.

7.3 Recommended Future Directions

This research has developed an important numerical fluid-structure model of the wire waveguide and fluid surrounding the distal-tip and will form the basis for future more complex modelling. Despite the results reported in this thesis, both experimental and numerical, and the fact that recent market approvals are imminent much work is still required to further understand this form of ultrasound energy delivery and the subsequent affects this has on plaque material and biological response. In particular the following future work must be addressed:

- Experimental investigations into the effects of ultrasound transmission in wire waveguide of lengths up to 1600 mm, as required for minimally invasive cardiovascular surgery, and the effects of bending, as the wire waveguide navigates through the tortuous vascular structure, on ultrasound transmission.

- Experimental investigation of the use of tapered wire waveguides, achievable distal-tip displacements and internal standing wave structure.

- Experimental studies of wire waveguide reliability, wire fatigue and cycles to failure for various input displacements

- Experimental measurements in blood and the threshold intensity required to cause cavitation. Cavitation may be determined through sono-luminescence or hydrophone techniques.

- Experimental measurements of the acoustic streaming produced in the region surrounding the distal-tip through flow analysis methods such as Particle Image Velocimetry (PIV).

- Numerical harmonic modelling of wire waveguides over lengths required in minimally invasive surgery, modelling of tapered wire waveguides and bending in the wire waveguides.

- Numerical fluid modelling of the acoustic streaming identified in the region surrounding the distal-tip.

- Testing of the ultrasonic wire waveguide apparatus on biological plaques and healthy arterial tissue to identify mechanism of ablation and disruption.

- Testing of ultrasonic wire waveguide apparatus on vascular cells including endothelial cells and smooth muscle cells. Smooth muscle cell proliferation is closely associated with restenosis and a study into how cells respond after the administration of therapeutic ultrasound under mechanical and biological conditions similar to those *in vivo*.

References

[1] World Health Organisation. Publications, World Health Report, 2003.

[2] American Heart Association. Publications, International Cardiovascular Disease Statistics, 2004.

[3] American Heart Association. Publications, Heart Disease and Stroke Statistics- Update, 2003.

[4] Irish Heart Foundation, Reports and Position Statements: Mortality from Cardiovascular Disease (CVD), 2005.

[5] O'Rourke M. Mechanical Properties in Arterial Disease. *Hypertension*, 26, pp 2-9, 1995.

[6] Salunke NV and Topoleski LDT. Biomechanics of Atherosclerotic Plaque. *Critical Reviews in Biomedical Engineering*, 25(3), pp 243- 285, 1997.

[7] Ariani M, Fishbein M, Chae JS, Sadeghi H, Don Michael TA. , Dubin SB and Siegel RJ. Dissolution of Peripheral Arterial Thrombi by Ultrasound, *Circulation*, 84, pp 1680- 1688, 1991.

[8] Gruentzig AR. Transluminal dilation of coronary artery stenosis. *Lancet*, 1, pp 263, 1978.

[9] Gruentzig AR, Senning A and Siegenthalaer WE. Non-operative dilation of coronary artery stenosis: percuntaneous transluminal coronary angioplasty. *N Engl. J. Med.*, 301, pp 61-8, 1979.

[10] King S.B. III. Angioplasty from Bench to Bedside. *Circulation*, 93, pp 1621- 1629, 1996.

[11] Folland ED. Chapter 1: Balloon Angioplasty. In: Topol EJ and Serruys PW (Eds.). *Current Review of Interventional Cardiology*, Philadelphia, 1994.

[12] De Jaegere PPT, De Feyter PJ and Serruys PW. Chapter 8: Intracoronary Stenting. In: Topol EJ and Serruys PW (eds.). *Current Review of Interventional Cardiology*, Philadelphia, 1994.

[13] Schwartz SM and Reidy MA. Chapter 39: Restenosis. In: Fuster V, Ross R and Topol EJ (Eds.). *Atherosclerosis and Coronary Artery Disease*, Lippincott- Raven Publishers, Philadelphia, 1996.

[14] C. Bauters and J.M. Isner. The biology of restenosis. In: E.J. Topol, Editor, *Textbook of Cardiovascular Medicine*, Lippincott-Raven, Philadelphia, Pennsylvania, pp. 2465–2490, 1998.

[15] William NG, Wai-Hong Chen, Pui-Yin Lee and Chu-Pak Lau. Initial experience and safety in the treatment of chronic total coronary occlusions with a new optical coherent reflectometry-guided radiofrequency ablation guidewire, *The American Journal of Cardiology*, Volume 92 (6), pp 732-734, 2003.

[16] Harmann A and Kaltenbach M. Chapter 2: Approaches to Total Coronary Occlusions. In: Topol EJ and Serruys PW (eds.). *Current Review of Interventional Cardiology*, Philadelphia, 1994.

[17] Loree HM, Grodzinsky AJ, Park SY, Gibsom LJ and Lee RT. Static Circumferential Tangential Modulus of Human Atherosclerotic Tissue. *J. Biomech.*, 27(2), pp 195-204, 1994.

[18] Topoleski LDT, Salunke NV, Humphrey JD and Mergner WJ. Composition and history-dependent radial compressive behaviour of human atherosclerotic plaque. *J. Biomed. Mater. Res.*, 35, pp 117- 127, 1997.

[19] Moussa I, Di Mario C, Moses J, Reimers B, Di Francesco L, Martini G, Tobis J and Colombo A. Coronary stenting after rotational atherectomy in calcified and complex lesions: angiographic and clinical follow-up results. *Circulation*, 96, pp 128- 136, 1997.

[20] Topoleski LDT and Salunke NV. Mechanical behaviour of calcified plaques: a summary of compression and stress-relaxation experiments. *Z Kardiol 89: Suppl* 2, II/85-II/91, Steinkopff Verlag, 2000.

[21] Rosenschein U, Rozenszajn LA, Kraus L, Marboe CC, Watkins JF, Rose EA, David D, Cannon PJ and Weinstein JS. Ultrasound Angioplasty in Totally Occluded Peripheral Arteries. *Circulation*, 83, pp 1976- 1986, 1991.

[22] Siegel RJ. Chapter 13: Intravascular Ultrasound Angioplasty. In: Topol EJ and Serruys PW (Eds.). *Current Review of Interventional Cardiology*, Philadelphia, 1994.

[23] Yock PG and Fitzgerald PJ. Catheter-based Ultrasound Thrombolysis: Shake, rattle and reperfuse. Circulation, 95: pp 1360- 1362, 1997.

[24] Sobbe A, Stumpff U, Trubenstein G, Figge H and Kozuschek W. Die Ultraschall-Auflosung von Thromben. *Klin Wochenschr*, 52, pp 1117- 1121, 1974.

[25] Siegel RJ, Fishbein MC, Forrester J, Moore K, DeCastro E, Daykhovsky Z and Don Michael TA. Ultrasonic Plaque Ablation: a new method for

recanalisation of partially or totally occluded arteries. *Circulation*, 78, pp 1443- 1448, 1988.

[26] Rosenschien U, Bernstein J, Di Segni E, Kaplinsky E, Bernheim J and Rozenszain LA. Experimental Ultrasonic angioplasty: disruption of atherosclerotic plaques and thrombi *in vitro* and arterial recanalisation *in vivo*. *J Am Coll Cardiol*., 15, pp 711- 717, 1990.

[27] Siegel RJ, Gaines P, Crew JR and Cumberland DC. Clinical Trial of Percuntaneous Peripheral Ultrasound Angioplasty. *JACC.*, 22, (2), pp 480-488, 1993.

[28] Steffen W, Fishbein MC, Luo H, Lee DY, Nita H, Cumberland DC, Tabak SW, Carbonne M, Maurer G and Seigel RJ. High Intensity, Low Frequency catheter-delivered ultrasound dissolution of occlusive coronary artery thrombi: An *in vitro* and *in vivo* study. *J. Am Coll Cardiol*, 24, pp 1571-1579, 1994.

[29] Goodspeed W. Press release for Flowcardia Inc., Sunnyvale, CA, USA. Flowcardia Inc. receives European regulatory approval and successfully U.S. feasibility clinical trial, Flowcardia Inc., January 28th, 2005.

[30] Clinical Trials Office, Columbia University Medical Centre. Principal Investigator: Gregg Stone. FACTOR - *Flowcardia's Approach to Chronic Total Occlusion Recanalisation*, 2005

[31] Hayashi K. 2001. Mechanical Properties of Arterial Wall. In: International Centre for Mechanical Sciences (CISM), September 2001, Italy

[32] McDonald DA. *Blood flow in Arteries*, 2nd Edition, Edward Arnold, 1974.

[33] S.Z. Zhao. The Numerical Analysis of Fluid- Solid Interactions for Blood Flow in Arterial Structures, Part 1: A review of models for arterial wall behaviour. *Proc Instn Mech Engrs.*, 212 (Part H), 1998.

[34] Daria- Haust M. The natural history of Human Atherosclerotic Lesions. In: *Vascular Injury and Atherosclerosis,* Moore S (Ed), New York, Marcel Dekker Inc, pp 1-24, 1981.

[35] Woolf N. *Pathology of Atherosclerosis,* 1st ed., London: Butterworth Scientific. 1982.

[36] Ross R. The pathogenesis of atherosclerosis- an update, N. Engl. J Med., 314, pp 488- 500, 1986.

[37] Bouissou M, Pieraggi T and Julian M. Chapter 16: Progression, Topographical Aspects and Regression of Atherosclerosis. In: Camilleri JP, Berry CL, Fiessinger JN and Bariety (Eds.) *Diseases of the Arterial Wall.* Springer Verlag. 1989.

[38] Stary HC. Chapter 26: The histological classification of atherosclerotic lesions in Human Coronary Arteries. In: Fuster V, Ross R and Topol EJ (eds.). *Atherosclerosis and Coronary Artery Disease*, Lippincott- Raven Publishers, Philadelphia, 1996.

[39] Cotran RS, Kumar V, and Robbins SL. Pathologic Basis of Disease, 4th Ed., W.B. Saunders Co., Philadelphia, 1989, p. 557.

[40] Hayashi K and Imai Y. Tensile properties of atheromatous plaque and an analysis of stress in atherosclerotic wall, *J. Biomechanics*, 30 (6), pp 573-579, 1997.

[41] Mohan D and Melvin JW. Failure properties of passive human aortic tissue. Part 1: Uniaxial tension tests, *J. Biomechanics*, 15 (11), pp 887-902, 1982.

[42] Mohan D and Melvin JW. Failure properties of passive human aortic tissue. Part 2: Biaxial tension tests, *J. Biomechanics*, 16 (1), pp 31-44, 1983.

[43] Kaltenbach M, Beyer J, Walter S, Klepzig and Schmidts L. Prolonged application of pressure in transluminal coronary angioplasty, *Catheterisation and Cardiovascular Diagnosis*, 10, pp 213-219, 1984.

[44] Lendon CL, Davies MJ, Richardson PD and Born GVR. Testing of small connective tissue specimens for the determination of the mechanical behaviour of atherosclerotic plaques. *J. Biomedical Engineering*, 15, pp 27-33, 1993.

[45] Lee RT, Richardson SG, Loree HM, Grodzinskey AJ, Gharib SA, Schoen FJ and Pandian N. Prediction of the mechanical properties of human atherosclerotic tissue by high-frequency intravascular ultrasound imaging. *Arteriosclerosis Thrombosis*, 12, pp 1-5, 1992.

[46] Lee RT, Grodzinskey AJ, Frank EH, Kamm RD and Schoen FJ. Structure-dependent dynamic behaviour of fibrous caps from human atherosclerotic plaques. *Circulation*. 83, pp 1764-1770, 1991.

[47] Siegel R. Use of Therapeutic Ultrasound in Percuntaneous Coronary Angioplasty, experimental *In vitro* studies and Initial Clinical Experience. *Circulation*, 89(4), pp 1587- 1592, 1994.

[48] Oh S, Kleinberger M and McElhaney JH. A finite element analysis of balloon angioplasty, *ASME Adv. Bioeng.*, 22, pp 269- 272, 1992.

[49] Oh S, Kleinberger M and McElhaney JH. Finite element analysis of balloon angioplasty. *Med. Biol. Eng. Comput.*, 32, pp 108- 114, 1994.

[50] Atar S, Luo H, Nagai T and Siegel RJ. Ultrasonic Thrombolysis: catheter-delivered and transcutaneous applications. *European Journal of Ultrasound*, 9, pp 39-54, 1999.

[51] Demer LL, Mehrdad A and Seigel RJ. High Intensity Ultrasound Increases Distensibility of Calcific Atherosclerotic Arteries. *JACC*, 18 (5), pp 1259-1262, 1991.

[52] Siegel RJ, Gaines P, Crew JR and Cumberland DC. Clinical Trial of Percuntaneous Peripheral Ultrasound Angioplasty. *JACC.*, 22, (2), pp 480-488, 1993.

[53] Morgan Electroceramics Ltd. Technical Publications. Piezoelectric Technical Tutorials. 2004.

[54] Perkins JP. Power Ultrasonic Equipment: Practice and Application. (Based on a paper presented at the Sonochemistry Symposium, Annual Chemical Congress, Warwick University, UK, 8-11 April 1986.

[55] Belford J.F. Morgan Electroceramics Ltd. The Stepped Horn. Technical Publication paper TP-214. 2004.

[56] Fischell TA, Abbas MA, Grant GW, Siegel RJ. Ultrasonic Energy: Effects on vascular function and integrity, *Circulation*, 84, pp 1783- 1795, 1991.

[57] Burdic WS. Underwater Acoustic System Analysis. 2nd Edition Prentice Hall. 1991.

[58] Nyborg WL. Chapter 1. Basic Physics of Low Frequency Therapuetic Ultrasound. In: Ultrasound Angioplasty. Developments in Cardiovascular Medicine. (Ed. by Siegel RJ). Kluwer Academic Publishers, 1996.

[59] Lee CP and Wang TG. Outer acoustic streaming. *J Acoust Soc Am.*, 40, pp 1363-1370. 1990.

[60] Morse PM. 1981. Acoustical Society of America, Vibration and Sound, New York, Section 27, 311-326, 1981.

[61] Thoe TB, Aspinwall DK and Wise MLH. Review of ultrasonic machining, *I. J. Mach. Tools Manufact.*, 38 (4), pp 239-255, 1998.

[62] Makin RS and Everbach EC, *J. Acoust. Soc. Am.*, Vol. 100(3), pp 1855-64, 1996.

[63] Stephanis CG, Hatiris JG and Mourmouras DE. The process (mechanism) of erosion of soluble brittle materials caused by cavitation. *Ultrasonics Sonochemistry*, 4, pp 269-271, 1997.

[64] Steffen W, Fishbein MC, Luo H, Lee DY, Nita H, Cumberland DC, Tabak SW, Carbonne M, Maurer G and Seigel RJ. High Intensity, Low Frequency catheter-delivered ultrasound dissolution of occlusive coronary artery thrombi: An *in vitro* and *in vivo* study. *J. Am Coll Cardiol*, 24, pp 1571-1579, 1994.

[65] Seidel RF (Jr.), Chapter 13: Distributed Systems. In: An Introduction to Mechanical Vibrations 3rd Ed, Wiley, 1989.

[66] Cunningham PM. Use of Finite Element Method in Ultrasonic Applications. *Ultrasonic Industry Association Symposium, June 2000.*

[67] ANSYS© Multiphysics 8.1: Structural Guide, *Chapters 4: Harmonic Response Analysis*. 2004.

[68] ANSYS© Multiphysics 8.1: *Structural Guide, Chapters 15: Acoustics*. 2004.

[69] Johnson DH and Pal D. 2003. Technical Publications: *Simulation of an ultrasonic piezoelectric transducer*. FEA Consulting paper. Cybersonics, Inc.

[70] Branson Ultrasonics Corporation©, *Instruction Manual: Sonifier 150: Ultrasonic Cell Disrupter and Homogiser*, Branson Ultrasonics Corporation, 41 Eagle Road, Danbury, CT, USA, 1999.

[71] Branson Ultrasonics Corporation©, *Sonifier Cell Disrupter: Microtips*, Branson Ultrasonics Corporation, 41 Eagle Road, Danbury, CT, USA, 1999.

[72] Mihalcz I. Fundamental characteristics and design method for nickel-titanium shape memory alloy. *Periodica Polytechnica Ser. Mech. Eng.*, 45(1), pp 75-86, 2001.

[73] Dolve M and Cardone D. Mechanical behaviour of shape memory alloys for seismic applications. Part 2: Austenite NiTi wires subjected to tension. *International Journal of Mechanical Sciences*, 43, pp 2657-2677, 2001.

[74] Fort Wayne Metals©, *Certificate of Compliance and Chemical Composition*, 9609 Indianapolis Road, Fort Wayne, IN, USA, 2005.

[75] Fort Wayne Metals©, *Nitinol General Data Specification Sheet*, 9609 Indianapolis Road, Fort Wayne, IN, USA, 2005.

[76] ANSYS© Multiphysics 8.1: *Structural Guide, Chapters 3: Modal Analysis*. 2004.

[77] ANSYS© Multiphysics 8.1:*Element Library, Plane42 Element Description.* 2004.

[78] ICRU Report. *Tissue substitutes, phantoms and computational moddeling in medical ultrasound.* International commission of radiation units and measurements, 7910 Woodmont Avenue, Bethesda, Maryland, 20814, USA, 1998.

[79] Jain A, Demer LL, Raizner AE, Hartley CJ, Lewis JM and Roberts R. *In vivo* assessment of vascular dilation during percuntaneous transluminal coronary angioplasty, *Am. J. Cardiol.*, 60, pp 988-992, 1987.

[80] Akter T, Stokes J, M.S.J. Hashmi and Rafferty A. Manufacturing of Synthetic Shell Media for Industrial Waste Air Treatment Process Using Powder Metallurgical Method. Sir Bernard Crossland Symposium. Materials Processing Research Centre (MPRC), Dublin City University, Dublin 9, Ireland, 2005.

[81] Vito RP, Whang MC, Giddens DP, Zarins CK and Glagov S (Goldstein SA Ed.). Stress analysis of the diseased arterial cross section, *ASME Adv. Bioeng.*, 17, 1990

[82] Lee RT, Loree HM, Cheng GC, Lieberman EH, Jaramillo N and Schoen FJ. Computational structural analysis based on intravascular ultrasound imaging before *in vitro* angioplasty: prediction of plaque fracture location, *J. Am. Coll. Cardiol.*, 21(3), pp 777-782, 1993.

[83] Beatie DK, Vito RP and Glagov SP. Mechanical modelling: assessing atherosclerotic plaque behaviour and stability in humans, *Intl. J. Cardiovasc. Med.*, 2(2), pp 69-81, 1999.